Photonic systems based on carbon nanotubes: photoluminescence enhancement and saturable absorbers by inkjet printing and integration on fibre tapers

Mohammad Mubarak Mohammed Al Araimi

Doctor of Philosophy

Aston University

May 2018

Aston University
Photonic systems based on carbon nanotubes: photoluminescence enhancement and saturable absorbers by inkjet printing and integration on fibre tapers
Mohammed Al Araimi
Doctor of Philosophy
May 2018

The multifunctional properties of single-wall carbon nanotubes (SWNTs) created a robust platform for unprecedented innovations in a variety of applications in photonics, sensors, electronics, smart manufacturing and drug delivery. This thesis presents an experimental study of the author's research using innovative approaches for the development of photonic systems based on SWNTs' dispersions and composites, featuring enhanced and effective optical properties. The first set of experiments demonstrates a novel approach for the enhancement of SWNTs' photoluminescent (PL) properties via complexation with organic dyes. One of the more significant findings to emerge from this investigation is the interaction of the indopentamethinedioxaborine dye (DOB-719) with SWNTs, which resulted in new optical features in the spectral range of the intrinsic excitation of the dye, providing clear evidence of the resonance energy transfer from DOB-719 to the SWNTs. The findings from this study allowed for the proposal of the mechanism of interaction between the SWNT and DOB-719, where the dye is attracted to the SWNT surface via π-π stacking with the hydrophobic part facing the aqueous medium by polar groups.

The second set of experiments examined a limitation imposed by the use of SWNT-polymer composites for saturable absorber (SA) applications. The integration of this device in the fibre cavity resulted in modification of the composite properties under continuous high power laser irradiation, which limits the use of composites to generate ultrashort pulses with stable parameters for a long operation time (>10,000 hours). This stimulated the design of advanced approaches in this work as an alternative to the composite method.

The first approach describes a method for the controllable integration of SWNT directly on the core of a fibre edge, using the inkjet printing technique. It is important to note that a direct correlation between the number of printed layers and properties of SA was determined, showing that a SA with 20,000 layers gives the best parameters. The obtained output power and pulse energy are higher than all earlier reported results on SA for erbium-doped fibre lasers using sandwiched SWNT- composites.

The second approach is to coat the tapered fibre with a low refractive index SWNT-polymer composite. This method depends on lateral interaction with the evanescence field of the propagating pulse in the laser cavity. The study reports SAs devices with controllable saturation intensity, low losses and large saturable to non-saturable loss ratios.

Keywords: single-wall carbon nanotubes; indopentamethinedioxaborine dye, photoluminescence, saturable absorber, ultrafast fibre laser, inkjet printing, tapered fibres.

DEDICATION

3

I wish to dedicate this work firstly to my parents who brought me up in the best possible manner. Then to my family, especially my beloved wife, and to my lovely kids who always stand proud for their father's achievements.

Acknowledgements

Table of Contents

Abbreviations

AC	Autocorrelation trace.
AD	Arc discharge.
BWF	Breit-Wigner-Fano line shape of the Graphite mode.
CCD	Charge Coupled Device.
CMC	Carboxymetylcellulose.
CNTs	Carbon nanotubes.
CoMoCAT	Cobalt-molybdenum catalytic.
CPCL	Cetylpyridinium chloride.
CTAB	Cetyltrimethylammonium bromide.
CVD	Chemical vapour deposition.
DGU	Density gradient ultracentrifugation.
DI	Deionized water.
DMA	N,N-dimethylacetamide.
DMF	Dimethylformamide.
DNA	Deoxyribonucleic acid.
DOB-719	Indopentamethinedioxaborine dye.
DTAB	Dodecyltrimethylammonium bromide.
DWNTs	Double wall carbon nanotubes.
EDF	Erbium-doped fibre.
EDFL	Erbium-doped fibre laser.
EET	Exciton energy transfer.
FWHM	Full width at half maximum.
HiPco	High pressure carbon monoxide.
HRTEM	High-resolution Transmission Electron Microscopy.
LA	Laser ablation.
LD	Laser diode.
MQW	Multiple quantum well.
m-SWNTs	Metallic Single-wall carbon nanotubes.
MWNT	Multiwall carbon nanotube.
NA	Numerical aperture.
Na-CMC	Sodium carboxymethylcellulose.
NIR	Near infra-red range.
NMP	N- N-methyl-2-pyrrolidone.
NOLM	Nonlinear loop mirror.
NPR	Nonlinear polarization.

PC	Polarization controller.
PANi	Polyaniline.
PL	Photoluminescence.
PLE	Photoluminescence excitation-emission.
PMMA	Polymethylmethacrylate
PS	Polystyrene.
PTFEMA	Poly 2,2,2-trifluoroethyl methacrylate.
PVAc	Polyvinyl acetate.
PVA	Polyvinyl alcohol.
PVP	Polyvinylpyrrolidone.
RBM	Radial breathing mode.
RET	Resonance energy transfer.
SA	Saturable absorber.
SC	Sodium cholate.
SDBS	Sodium dodecylbenzenesulphonate.
SDOC	Sodium deoxycholate.
SDS	Sodium dodecyl sulphate.
$sech^2$	Hyperbolic secant squared pulse profile.
SESAMs	Semiconductor saturable absorber mirrors.
SMF	Single mode fibre.
SNR	Signal-to-noise ratio.
s- SWNTs	Semi-conducting Single-wall carbon nanotubes.
STDOC	Sodium taurodeoxycholate.
STM	Scanning Tunnelling Microscopy.
SWeNT	SouthWest NanoTechnologies.
SWNTs	Single-wall carbon nanotubes.
TEM	Transmission Electron Microscopy.
TFT	Thin film transistor.
U-DGU	Uniform density gradient ultracentrifugation.
VLSI	Very-large-scale integration.
VOA	Variable optical attenuator.
WDM	Wavelength division multiplexing.
0D	Zero-dimensional.
1D	One-dimensional.
2D	Two-dimensional.
3D	Three-dimensional.

Symbols

α The length of the unit lattice vector of graphene sheet and equal to 2.49 Å

A_λ Optical absorbance of the material at known wavelength, λ (a.u.).

α_λ Absorption coefficient at wavelength, λ ($Lg^{-1}m^{-1}$).

α_{lin} Linear absorption of the absorber (a.u.).

α_{ns} Non-saturable absorption (a.u.).

α_0 Modulation depth in %.

C Speed of light in vacuum $=3\times10^8$ m/s.

$\vec{C}_h$ Chiral vector.

d_t Nanotube diameter (nm).

ε_{bg} Dielectric constant of both the SWNTs and the background of their surrounding environment.

F_{sat} Saturation fluence (saturation energy per unit area).

f_{rep} Fundamental repetition rate in Hz.

G_{mix} Gibbs free energy of mixing.

H_{mix} Enthalpy of mixing.

h Planck's constant (6.63×10^{-34} joule-seconds).

I_{sat} Saturation intensity (power per unit area).

n Average refractive index of the cavity. $n \approx 1.5$ for single mode-fibre.

P_{avg} Average output power.

P_{max} Maximum pump power.

$P_{p.th}$ Threshold pump power.

P_{pump} Pump power.

P_{sat} Saturation power.

S_{mix} Entropy of mixing.

$\tau_{A.c}$ Autocorrelation trace pulse duration.

τ_p Pulse duration for the SA device.

λ_{EX} Excitation wavelength (nm).

λ_{EM} Emission wavelength (nm).

λ_M Dye monomer peak at a particular wavelength (nm).

$\Delta\lambda$ Spectral bandwidth (nm).

θ Chiral angle.

List of figures

16

List of tables

List of publications

[1]   C. Zou, T. Wang, Z. Yan, Q. Huang, M. Al Araimi, A. Rozhin, *et al.*, "Wavelength-tunable passively mode-locked Erbium-doped fiber laser based on carbon nanotube and a 45° tilted fiber grating," *Optics Communications,* vol. 406, pp. 151-157, 2017/06/20/ 2018.

[2]   Q. Huang, T. Wang, C. Zou, M. Al Araimi, A. Rozhin, and C. Mou, "Passively harmonic mode-locked erbium-doped fiber laser at a 580 MHz repetition rate based on carbon nanotubes film," *Chinese Optics Letters,* vol. 16, p. 030019, 2018/03/10 2018.

[3]   M. Chernysheva, M. A. Araimi, G. A. Rance, N. J. Weston, B. Shi, S. Saied, *et al.*, "Revealing the nature of morphological changes in carbon nanotube-polymer saturable absorber under high-power laser irradiation," *Scientific Reports,* vol. 8, p. 7491, 2018/05/10 2018.

[4]   K. Hani, S. S. V., M. Chengbo, G. A. Martinez, A. M. Al, R. Aleksei, *et al.*, "Bright-Dark Rogue Waves," *Annalen der Physik,* vol. 530, p. 1700362, 2018.

[5]   C. Zou, Z. Yan, Q. Huang, T. Wang, C. Mou, M. Al Araimi, *et al.*, "Wavelength switchable bidirectional Q-switched fiber laser based on 45° tilted fiber grating and carbon nanotube," in *Advanced Photonics 2018 (BGPP, IPR, NP, NOMA, Sensors, Networks, SPPCom, SOF)*, Zurich, 2018, p. JTu2A.13.

[6]   Q. Huang, C. Zou, M. Al Araimi, C. Mou, and A. Rozhin, "L-band passively harmonic mode-locked Erbium-doped fiber laser based on carbon nanotubes film," in *Advanced Photonics 2018 (BGPP, IPR, NP, NOMA, Sensors, Networks, SPPCom, SOF)*, Zurich, 2018, p. NpTh1G.6.

[7]   M. Chernysheva, A. Bednyakova, M. Al Araimi, R. C. Howe, G. Hu, T. Hasan, *et al.*, "Double-Wall Carbon Nanotube Hybrid Mode-Locker in Tm-doped Fibre Laser: A Novel Mechanism for Robust Bound-State Solitons Generation," *Sci Rep,* vol. 7, p. 44314, Mar 13 2017.

[8]   C. Mou, Q. Huang, C. Zou, T. Wang, M. Al Araimi, and A. Rozhin, "Passively harmonic mode-locking in an Erbium-doped fiber laser based on carbon nanotubes film at repetition rates to 500MHz," in *Asia Communications and Photonics Conference*, Guangzhou, Guangdong, 2017, p. M3H.6.

[9]   C. Mou, C. Zou, M. AlAraimi, Q. Huang, T. Wang, and A. Rozhin, "Effect of carbon nanotube fabricated by cobalt molybdenum catalyst on performance of Erbium-

doped mode locked fiber laser," in *Asia Communications and Photonics Conference*, Guangzhou, Guangdong, 2017, p. Su2A.87.

[10] T. Wang, Y. Zhao, C. Wang, Z. Liu, C. Mou, Y. Liu*, et al.*, "Passively Q-switched erbium fiber laser using few-mode fiber long-period grating and carbon nanotube for cylindrical vector beam generation," in *Conference on Lasers and Electro-Optics*, San Jose, California, 2017, p. STu4K.6.

[11] A. Martinez, M. Al Araimi, A. Dmitriev, P. Lutsyk, S. Li, C. B. Mou*, et al.*, "Low-loss saturable absorbers based on tapered fibers embedded in carbon nanotube/polymer composites," *Apl Photonics,* vol. 2, p. 126103, Dec 2017.

[12] H. Kbashi, M. Al Araimi, A. Rozhin, and S. V. Sergeyev, "Vector Rogue Waves in a Carbon Nanotube Mode-Locked Fiber Laser," in *2017 European Conference on Lasers and Electro-Optics and European Quantum Electronics Conference*, Munich, 2017, p. EF_6_2.

[13] C. Zou, T. Wang, Z. Yan, Q. Huang, M. Al Araimi, A. Rozhin*, et al.*, "Wavelength-tunable mode-locked fiber laser with birefringence-enhanced cavity," in *2017 16th International Conference on Optical Communications and Networks (ICOCN)*, 2017, pp. 1-3.

[14] T. Wang, C. Zou, Z. Yan, Q. Huang, C. Mou, K. Zhou*, et al.*, "Tunable mode locked Erbium-doped fiber laser based a tilted fiber grating and carbon nanotube saturable absorber," in *2017 Conference on Lasers and Electro-Optics Pacific Rim (CLEO-PR)*, 2017, pp. 1-2.

[15] A. Manilov, A. Kozinetz, I. Gavrilchenko, Y. Milovanov, T. Mukhamedzhanov, S. Alekseev*, et al.*, "Photoelectric Signal Conversion in Deep pn Junction for Detection of Carbon Nanotubes with Adsorbed SDBS in Aqueous Solution," *Journal of Nano- and Electronic Physics,* vol. 9, pp. 4020-1, 2017.

[16] P. Lutsyk, Y. Piryatinski, M. Al Araimi, R. Arif, M. Shandura, O. Kachkovsky*, et al.*, "Emergence of Additional Visible-Range Photoluminescence Due to Aggregation of Cyanine Dye: Astraphloxin on Carbon Nanotubes Dispersed with Anionic Surfactant," *Journal of Physical Chemistry C,* vol. 120, pp. 20378-20386, Sep 15 2016.

[17] M. Al Araimi, P. Lutsyk, A. Verbitsky, Y. Piryatinski, M. Shandura, and A. Rozhin, "A dioxaborine cyanine dye as a photoluminescence probe for sensing carbon nanotubes," *Beilstein J Nanotechnol,* vol. 7, pp. 1991-1999, 2016.

[18]   M. Chernysheva, M. A. Araimi, S. Sukhanov, R. Arif, and A. Rozhin, "Uni- and bidirectional hybrid mode-locked erbium-doped isolator-free fibre laser," in *2016 International Conference Laser Optics (LO)*, 2016, pp. R1-29-R1-29.

[19]   M. Chernysheva, C. Mou, R. Arif, M. Al Araimi, M. Rummeli, S. Turitsyn*, et al.*, "High Power Q-Switched Thulium Doped Fibre Laser using Carbon Nanotube Polymer Composite Saturable Absorber," *Sci Rep,* vol. 6, p. 24220, Apr 11 2016.

[20]   M. Chernysheva, M. A. Araimi, H. Kbashi, R. Arif, S. V. Sergeyev, and A. Rozhin, "Isolator-free switchable uni- and bidirectional hybrid mode-locked erbium-doped fiber laser," *Opt Express,* vol. 24, pp. 15721-9, Jul 11 2016.

[21]   I. Chernikov, B. Zousman, M. Al Araimi, A. Rozhin, R. Arif, P. Lutsyk*, et al.*, "Nano-diamond ink formulation with strong photoluminescence properties," *Conference: International Conference on Diamond and Carbon Materials, 2016*.

Chapter 1: Introduction and Thesis Structure

1.1 Introduction

The discovery of carbon nanostructure materials, such as the fullerenes (0D), carbon nanotubes (1D) and graphene (2D), significantly contributed to the development of nanoscience and nanotechnology [1]. Within these nanostructure materials, carbon nanotubes (CNTs) have been suggested for a broad range of applications, due to their high mechanical strength, large specific surface area, and excellent electrical and thermal conductivity. These unique properties qualified them for several applications, such as microelectronic devices, including transistors and nonvolatile memories, energy storage devices including lithium-ion batteries, supercapacitors and fuel cells, water purification, and biotechnology [2, 3]. However, one of the main challenges in the development of carbon nanotube-based technology is obtaining a stable dispersion in liquids. These are the result of hydrophobically driven van der Waals interactions, which are an inherent consequence of their carbon sp^2 hybridization network. This is important because it negates the ability to fully take advantage of a nanotubes high aspect ratio and surface area. Thus, to fully take advantage of their properties effectively, SWNTs must be debundled into individual nanotubes and or small bundels. Although several strategies have been suggested in the litrature to overcome these challenges, non-covalently functionalization of the nanotubes have gained significant attention.

Particularly, single-wall carbon nanotubes (SWNTs) feature a unique prototype of 1D materials, allowing unpreceded testing of fundamental physical properties. It appeared that the surface of the SWNTs could result in strong interactions with the surrounding environment and can be exploited to design new functional materials. Practically, this approach can lead to constructing a nanosystem, combining specific properties and designing materials with advanced optical properties to be applied as an effective chemical probe, labels for diagnostics and treatment of live tissue, etc.[4-10].

However, the interaction of SWNTs with the surrounding environment resulted in quenching of the tubes photoluminescence (PL) quantum yield [11, 12] or degrading of their electronic transport properties [13, 14]. Several approaches were suggested to overcome these effects, such as the encapsulation of nanotubes in micelles of surfactants [15, 16] or

polymers [17], or the use of suspended nanotubes [11, 18]. Despite all these approaches, SWNTs still exhibit low PL in the near infra-red range (NIR) [19, 20].

The optical properties of SWNTs are promising for the development of next-generation devices [3]. For example, SWNTs can be used as components of biosensors and medical devices, due to their low dimensionality and chemical compatibility with biomolecules, such as proteins and Deoxyribonucleic acid (DNA). Besides, they are direct bandgap materials that feature PL emission in the NIR, which covers a broad range of wavelengths from 800 to 2000 nm [15, 21, 22]. Importantly, this range covers the biological tissue window (800-1000 nm) [23], optical sensors [24] and optical telecommunication systems [25]. For example, the E_{11} absorption for SWNTs matches the telecommunications C band (1530–1565 nm) making them suitable materials for various requirements in optical communications for real-life applications. Saturable absorbers (SAs) are the most successful photonic applications of SWNTs in fibre laser technologies. SAs serve as optical switches to modulate the laser continuous output wave into a train of ultrashort pulses [26]. SWNT-based SAs have been used as all-optical switches, optical amplifier noise suppressors, or mode-lockers to generate ultrashort laser pulses in fibre lasers. To satisfy the increasingly stringent requirements for fibre lasers, it is necessary to improve the nonlinear parameters of SWNT-SAs such as the modulation depth, saturation fluence, non-saturable loss and optical damage threshold. One way to realize this is to control the SWNT diameter distribution, length and bundling during the growth process of the nanotubes and to enhance the interaction of SWNTs with light during the integration process.

Taking the above into account, it is worth emphasizing that the easy fabrication and integration of the SWNTs in photonic devices are extremely valuable for various new photonic systems.

1.2 Aim and Objectives:

This thesis aims to develop photonic systems based on carbon nanotubes with enhanced optical properties. This aim will be achieved through the following objectives:

1-   Development of novel nanostructured complexes based on SWNTs and organic dyes to enhance the photoluminescent (PL) signal of the tubes in the range of excitation wavelengths, where the PL emission of the SWNTs is extremely low. Next, to study the new optical features of the resultant complexed materials with respect to the effect of each component in the complex. Following this, the obtained results from the studied system can

be used to propose the mechanism of interaction between the dye and SWNTs. The developed complex can be promising for several applications, such as reinforced composite materials, ultrafast photonics, chemical and biological sensing, drug delivery, energy storage, scanning probe microscopy, etc.

2-   Characterize the nature of the SWNT-polyvinyl alcohol (PVA) composite thermal degradation and evaluate the modification of the composite properties under continuous high power ultrashort pulse laser operation. This aim is motivated by the continuous development of ultrafast lasers towards high average power for various industrial application requirements. To date, the polymer composites method is widely used to fabricate flexible and freestanding SA devices, which can be sandwiched between two fibre connectors. However, there is a common understanding that SWNTs' composites suffer from a low thermal damage threshold, which can limit the long-term stability of such lasers. Therefore, it is important to understand and evaluate the nature of induced thermal damage in the composite under high power laser irradiation. The obtained results can be used to suggest alternative approaches to improve the stability of SA devices sandwiched between two fibre connectors, and possibly optimize the fabrication of SWNTs' polymer composites as reliable SAs in high power ultrafast lasers.

3-   Demonstrate a feasible, efficient and straightforward method to develop SAs, using the inkjet-printed SWNTs' technique.

4-   Develop a method for the fabrication of efficient SAs with controllable nonlinear parameters that can be utilized for the fabrication of better lasers and other nanomaterial-based nonlinear fibre devices.

1.3   Thesis Structure

This thesis consists of seven chapters; the contents are outlined as follows:

__Chapter 1__: discusses the potential limitations associated with carbon nanotubes. The chapter concludes by establishing the aim and objectives of the research that targeted to overcome some of the limitations to integrate SWNTs in photonic systems. Finally, the thesis layout and flow of subsequent chapters are outlined.

__Chapter 2__: presents an overview of SWNTs from the structure, growth techniques, dispersion in liquids and characterization.

__Chapter 3__: focuses on the interaction between organic dye (DOB-719) and the SWNTs dispersed with anionic surfactants. The research outcomes from this study reveal new

optical features in the spectral range of the intrinsic excitation of the dye, due to RET from DOB-719 to SWNTs.

Chapter 4: reveals the nature of morphological changes of the SWNTs' polymer composite based saturable absorber under a high power laser irradiation. The study discovers the nature of the SWNT-polyvinyl alcohol (PVA) film thermal degradation, and evaluates the modification of the composite elemental properties under a continuous high power laser regime. The obtained results show that high power laser radiation resulted in measurable changes in the composition and morphology of the SWNT-PVA film, due to efficient heat transfer from SWNT into the polymer matrix.

Chapter 5: demonstrates the inkjet printing method as an efficient and straightforward technique for the integration of SWNTs into fibre ferrule to serve as a saturable absorber. In addition, the study presents the performance of a mode-locked fibre laser, based on the printed nanotube layer in the saturable absorber. A set of SWNTs' layers were printed onto fibre connectors and exploited as SAs for the fibre laser. All samples were characterized in terms of nonlinear optical properties, and tested using an Erbium-doped fibre laser.

Chapter 6: develops a method for the fabrication of highly efficient SAs with controllable saturation fluence that can be achieved for the fabrication of better lasers and other nanomaterial-based SA devices. It also presents guidelines for the design of SAs according to their application.

Chapter 7: will present the overall thesis conclusion.

Chapter 2: Carbon Nanotubes for Photonics

This chapter is structured as follows; section 2.1 overviews the structure of nanotubes. Section 2.2 reviews the growth techniques for CNTs and highlights strengths and weaknesses of each. Section 2.3 discusses SWNTs' dispersion via liquid phase, which is crucial for SWNTs' functionalization. The discussion is extended to address dispersion of SWNTs in water and organic solvents individually in subsections 2.3.1 and 2.3.2, respectively. Section 2.4 discusses SWNTs' separation. Optical characterization of the functionalized SWNT, optical absorption, photoluminescent (PLE) and Raman spectroscopy, is presented in sections 2.5. Section 2.6 briefly introduces the optical properties of SWNTs and their potential application in photonics. Finally, section 2.7 concludes this chapter.

2.1 Carbon nanotubes structure

The history of CNTs can be traced back to 1952 when L V. Radushkevich *et al*. published the first Transmission Electron Microscopy (TEM) image in Russian script and did not receive the attention of the research community due to the cold war [27]. Four decades later, Iijima and his group published the famous paper called helical microtubules of graphitic carbon which gained the global research attention [28]. This has fuelled the research interest to explore the SWNTs structure using high-resolution TEM (HRTEM) and Scanning Tunnelling Microscopy (STM) [29]. The nanotubes can be imagined as a 2D graphene layer, where carbon atoms are arranged in the hexagonal structure. The tubes are formed by wrapping the graphene layer into a cylindrical form. The wrapping direction of the graphene layer is a crucial parameter because it will produce different chiralities defined by a pair of integers *(n,m)*, which is directly responsible for determining the tubes electronic properties. For example, the tube is known as zigzag when *m* = 0, armchair when *n* = *m* and otherwise the tube is called chiral. Moreover, they can be either metallic or semi-conducting, depending on tube chirality.

The hexagonal arrangement of atoms in CNT can be represented according to the tube chirality using the chiral vector ($\vec{C}_h$) and the chiral angle (*θ*). The following equation can define $\vec{C}_h$ along the wrapping direction *θ*:

$$\vec{C}_h = n\vec{a}_1 + m\vec{a}_2 \hspace{4cm} \text{Equation (2.1)}$$

where *n* and *m* are a pair of integers which define the number of steps along the unit vectors $\vec{a}_1$ and $\vec{a}_2$, as shown in figure 2.1.

Other parameters such as the tube diameter (d_t) and chiral angle (θ) can be defined as:

$$d_t = \frac{a}{\pi}\sqrt{n^2 + m^2 + nm}$$

Equation (2.2)

where a is the length of the unit lattice vector and equal to 2.49 Å

and, $\sin\theta = \dfrac{\sqrt{3}m}{2\sqrt{n^2 + m^2 + nm}}$ where $0 \leq \theta \leq 30$ Equation (2.3)
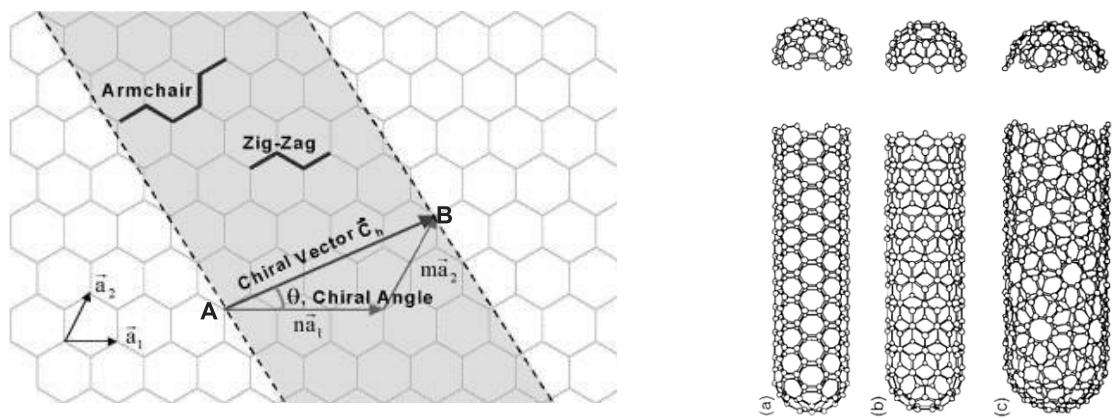
Figure 2.1   Schematic representation showing the wrapping effect on forming the nanotubes type on the right illustration of three types of tubes a) Armchair nanotubes b) zigzag nanotubes c) chiral nanotubes. Adapted from [30, 31]

In addition to chirality, the number of layers is another factor that is considered for classification of CNTs. Hence, they are classified as *single-wall carbon nanotube* (SWNT) and *multiwall carbon nanotube* (MWNT). SWNTs are the most basic structure of nanotubes. Their average diameter is around 1 nm, and possible lengths are more than 1000 orders of magnitude beyond that. However, MWNTs are made of multiple concentric cylindrical layers of different diameters sharing the same centre. The diameter and length of the MWNTs range from 5 to 50 nm and 10 µm, respectively. Importantly, double wall carbon nanotubes (DWNTs) can have inner and outer wall arrangements with different electronic properties (semi-conducting (s), or metallic (m)) in their structures. The concentric tube combinations of DWNTs made them an attractive platform for a wide range of applications [32, 33].

2.2 Growth of carbon nanotubes

Growth processes play an important role in the properties of carbon nanotubes. In this section will review the growth process of CNTs and highlight strengths and weaknesses of each. Presently, carbon nanotubes are fabricated using different methods, such as arc discharge (AD), laser ablation (LA) or chemical vapour deposition (CVD) but all these methods are still under industrial research improvement. The quality of carbon nanotubes, their yield, cost, and uniformity are still challenging. There are many possibilities of these methods functioning under different conditions with different set-ups and parameters. Each method has its own strengths and weaknesses over the production quality. Nowadays, the main issue concerns the large-scale and low-cost production of nanotubes for industrial applications.

2.2.1 Arc discharge method

Carbon AD (figure 2.2) is the first technique used to grow CNTs [28]. The process is obtained at vacuum chamber with two carbon electrodes. A gas source (usually Helium or Argon) is generated to successfully perform carbon deposition process. When high dc voltage is supplied between the anode and cathode, plasma of the inert gas is produced to evaporate the carbon atoms. The ejected carbon atoms are then deposited on the negative electrode to produce carbon nanotubes. Both SWNTs and MWNTs can be fabricated using this technique with maximum lengths of 50 nm, using high quality CNTs with fewer structural defects [34]. However, very low yield can be obtained from this method.
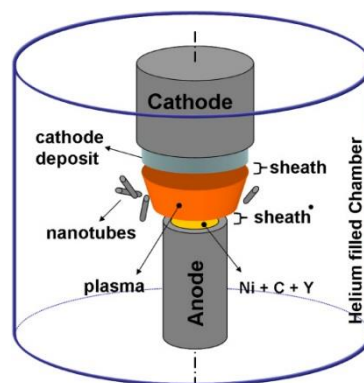
Figure.2.2.   Schematic of arc discharge technique. Adapted from [35]

2.2.2 Laser ablation method

In the laser ablation (figure 2.3) technique, carbon atoms are ablated by intense laser pulses at very high temperature in the presence of an inert gas and a catalyst. CNTs are produced and collected on a cold substrate. Both the AD and LAs technique require a high

temperature to produce CNTs, which is about 3000–4000 Celsius for the evaporation of carbon atoms from the initial carbon source. The method was established by Smalley *et al.* to grow MWNTs [36]. Later, the method was developed by the same team to produce SWNTs with controllable diameter [37]. However, this method is much more expensive than either AD or CVD.
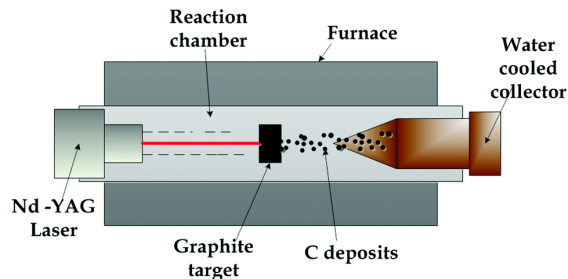
Figure 2.3.   Schematics of a laser ablation technique. Adapted from [38]

2.2.3 Chemical Vapour Deposition method (CVD)

The CVD (figure 2.4) technique was reported in 1993 by Yacamán and co-workers [37]. In a CVD system, a gas source (usually methane, acetylene or ethylene) is generated in the reaction chamber. The carbon atoms are then heated with a temperature range between 550 and 1000 Celsius. The carbon atoms react in the presence of catalysts (usually Nickel (Ni), Iron (Fe) or Cobalt (Co)) that are coated on the substrate to produce the CNTs. Compared with the first two techniques, CNTs can be produced at low temperature using the CVD method. Therefore, it is the most widely used method for the production of carbon nanotubes. This enhances CNTs' electronic properties in different applications. High quality SWNTs can be produced by the optimization of the catalysts. However, one of the main setbacks of CVD technique is the relatively high defects in MWNTs, which can be attributed to insufficient thermal energy.

Among the aforementioned methods, CVD has the most promising growth, not only because of high purity and large-scale production, but also because the diameter and the length of the CNTs can be easily controlled during the growth process.
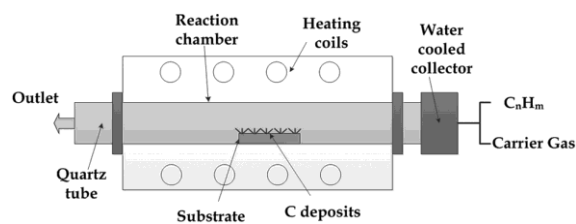
Figure 2.4   Schematics of a chemical vapour deposition technique. Adapted from [38]

In all of these three methods, CNTs are contaminated with impurities, which may have negative impact on CNTs intrinsic properties. In order to improve the quality of the nanotube, a purification process is needed after producing the carbon nanotubes. Normally, the most common impurities are carbonaceous impurities and metallic impurities. The carbonaceous impurities are due to the reaction process, while the metallic impurities are residual catalysts. Usually the oxidation method is used to remove carbonaceous impurities, whereas heating the samples can be used to evaporate the metallic impurities.

In the CVD method, the process can involve a gaseous catalyst, as in the high pressure carbon monoxide method (HiPco) or by means of a supported catalyst as in the Cobalt-molybdenum catalytic method (CoMoCAT). Compared with AD and LAs methods, the main advantage of CVD is the more straightforward way to scale up production to industrial levels. Additionally, the CVD method allows more chirality control during synthesis of the nanotubes. Therefore, nanotubes produced with HiPco and CoMoCAT methods are typically used for scientific and research purposes.

Commercially available CoMoCAT and HiPco SWNTs are used as source materials in this research. These tubes feature a strong optical absorption and photoluminescent (PL) in the range 1000 - 1600 nm, which corresponds to a typical tube diameter distribution of 0.7 - 1.3 nm.

2.3   Dispersion of carbon nanotubes in liquid

The current growth methods are incapable of controlling chiralities and diameters of SWNTs. Moreover, the hydrophobic nature of the nanotubes in liquids hinder the path towards the practical applications of these unique materials. Therefore, for photonics application, two major challenges need to be overcome: 1) dispersion in a solvent and 2) efficient separation according to the chirality [39-43].

To face the SWNTs' dispersibility issue, a considerable research effort has been devoted to improve the dispersion of SWNTs. These can be classified into two routes: covalent and non-covalent functionalization [44]. Covalent functionalization involves the use of chemical reactions to attach a functional group to the nanotube surface. This approach may introduce defects in the nanotube surface and modify the π-electron system, which can result in the degradation of the electronic properties of the nanotube [45-49]. Non-covalent functionalization normally takes advantage of the dispersing agent, such as deoxyribonucleic acid (DNA) or surfactants or polymer. In general, non-covalent functionalization preserves the physical and electronic properties of the nanotubes, at the same time giving them unique advantages associated with the organic conjugates [50, 51]. Figure 2.5 presents the preparation procedure for nanotubes' dispersion using a non-

covalent functionalization approach. It is essential to expose the nanotubes to ultrasonic treatments in the presence of liquid (water or organic solvent) and dispersant (such as surfactants polymer…. etc.). After the ultrasonication process, the mixture can be subjected to a high-speed ultracentrifugation process to phase out catalysts, and large bundles. Therefore, the non-covalent functionalization approach is considered throughout this thesis (chapters 3-5) to prepare SWNTs' dispersion.
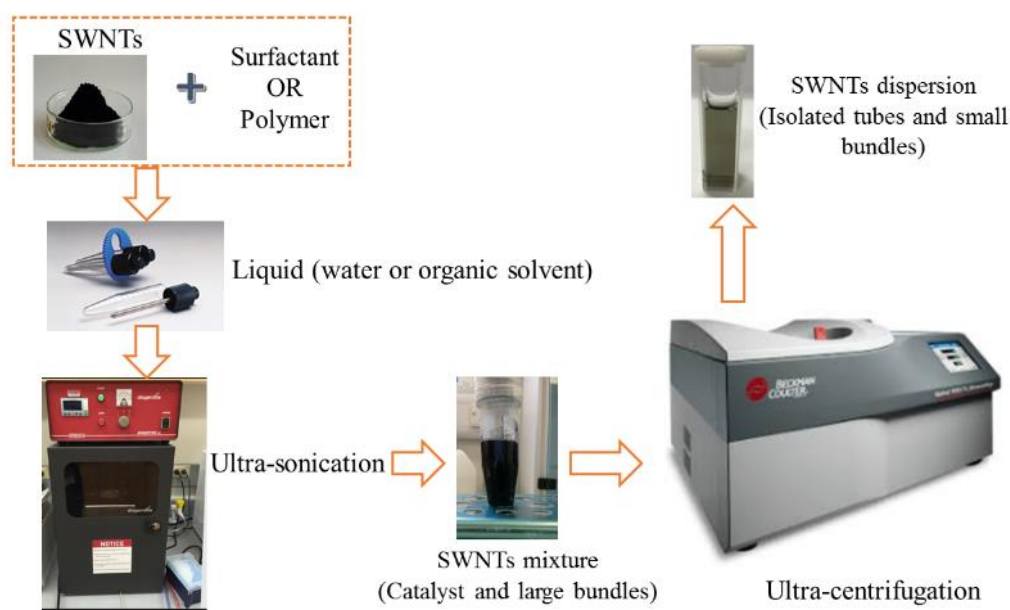
Figure 2.5   Preparation procedure for carbon nanotubes dispersion in solvents

The second challenge is related to the separation of the nanotubes by electronic properties (s- SWNTs and m-SWNTs) and chirality. Additionally, the terms "solubilization" and "dispersion" of nanotubes are unclearly employed in the literature. For nanotubes obtained in a liquid phase (water or organic solvents) the term dispersion is more relevant because nanotubes are not thermodynamically stable "solutions" and more likely are metastable [52]. Therefore, throughout this thesis, the term "dispersion" is considered.

2.3.1 Dispersion of carbon nanotubes in water

The hydrophobic nature of carbon nanotubes hinders their direct dispersion in a highly polar liquid such as water without any functionalization [44, 53]. To date, stable dispersions of SWNTs in water have been reported in the literature using surfactants [15, 54-58], polymers [55, 59-61], DNA [62-65] , polypeptides [66-68] and cellulose derivatives [69, 70]. Surfactants have been reported to produce stable nanotube dispersion in water with different dispersion efficiency [71, 72]. In SWNT water-based dispersion, a surfactant tends to form a micelle around the nanotubes' surface. The hydrophobic tails of the surfactant are

attached to the nanotube sidewall, while the hydrophilic heads are in contact with water. They are classified according to the charged group in their heads to ionic and non-ionic. The most common ionic surfactants for dispersing SWNTs are sodium dodecyl sulphate (SDS), sodium dodecylbenzenesulphonate (SDBS), sodium cholate (SC), sodium deoxycholate (SDOC), sodium taurodeoxycholate (STDOC), dodecyltrimethylammonium bromide (DTAB) cetyltrimethylammonium bromide (CTAB) and cetylpyridinium chloride (CPCL) [72]. Furthermore, these are sub-classified into anionic (negative charge carrier, such as SDS, SDBS, SC, SDOC and STDOC) and cationic (positive charge carrier, such as DTAB, CTAB and CPCL). On the other hand, Triton X, Pluronic, Igepal, and Brij series are non-ionic surfactants.

Water-soluble polymers are reported to wrap around the nanotubes [59, 60], supporting their dispersion and debundling. Mainly polyvinylpyrrolidone (PVP) and its copolymers with acrylic acid, vinyl acetate, dimethylaminoethyl methacrylate, polyvinyl sulphate, polystyrene sulphonate can stabilize the SWNTs dispersion in water [60]. In general, the wrapping of water-soluble polymers is thermodynamically favoured by the removal of the hydrophobic interface between the SWNT sidewalls and the water [59, 60].

Zhang *et al*. [32] proposed that single-stranded DNA (ss-DNA) forms a helical wrap around the nanotube surface via π-stacking [65].They also reported that the binding free energy of single-stranded DNA to SWNTs is higher than that between two tubes, promoting SWNTs' dispersion.

Cellulose derivatives, such as sodium carboxymethylcellulose (Na-CMC) [70, 73] and hydroxyethylcellulose [73] were also reported to disperse a high amount of SWNT in water without any visible aggregations.

2.3.2 Dispersion of carbon nanotubes in organic solvents

Many efforts have been devoted towards dispersing the nanotubes in organic solvents, such as N- N-methyl-2-pyrrolidone (NMP), dimethylformamide (DMF) and N,N-dimethylacetamide (DMA) [74-83]. Additionally, various surfactants and polymers have been reported as dispersing agents in such solvents to facilitate the dispersibility of SWNT [25, 79, 80, 84-86]. Among the solvents mentioned above, NMP has been reported as one of the most efficient for dispersing SWNTs [74, 75, 78, 79]. NMP is reported to disperse up to ~70% of individual SWNTs at a very low concentration (~0.004 gL^{-1}) [78]. A significant improvement would be to disperse SWNTs in organic solvent without the need for dispersant molecules. Ideally, stable SWNTs' dispersion in organic solvents can be achieved if the free energy of mixing (ΔG_{mix}) is negative [87].

$\Delta G_{mix} = \Delta H_{mix} - T\Delta S_{mix}$ Equation (2.4)

where T is the absolute temperature, ΔH_{mix} and ΔS_{mix} are defined as the enthalpy and entropy of mixing, respectively [88]. For SWNTs, the large molecular weight and high rigidity lead to an extremely small ΔS_{mix} [76, 89]. Due to their large mutual attraction, ΔH_{mix} is expected to be positive for all polymer–nanotube dispersion [76], resulting in a positive ΔG_{mix}, prohibiting nanotube dispersion. Therefore, for dispersion and stabilization of SWNTs in solvents, ΔH_{mix} needs to be very small. NMP is one of the most efficient organic solvents for dispersing pristine SWNTs. Hassan *et al.* studied the dispersion of SWNTs in NMP, using a range of non-ionic surfactants, including Triton X 100, Pluronic F98, Igepal DM-970 in NMP [79, 90]. They reported a higher amount of SWNTs dispersed with the above surfactants, compared to SWNTs obtained in NMP. However, the presence of non-ionic surfactants in SWNTs dispersion does not facilitate isolation or stabilizing of SWNTs [79, 90]. Importantly, they reported the addition of PVP polymer to SWNTs/NMP dispersion, resulting in debundling of the nanotubes [79], even after re-aggregation [90]. At the same time, the relationship between the increase in PL intensity and SWNTs' diameter revealed that the debundling process depends on the diameter and chirality, and is more efficient for larger diameters.

2.4   SWNTs' sorting

This section introduces post-growth separation techniques designed to achieve a homogeneous dispersion of SWNTs with a specific diameter or electronic properties. Although a wide variety of techniques have been reported in the literature, the most successful methods in terms of bulk separation or obtaining individual chiral nanotubes are discussed.

The carbon nanotubes' growth techniques, discussed in section 2.2, are producing a heterogeneous mixture of nanotubes with mixed electronic properties (m-SWNTs and s-SWNTs) and different diameters. Separation is crucial for many of the potential applications [91]. For example, m-SWNTs have attracted research interest for their electrical properties as Very-large-scale integration (VLSI) interconnects. They feature high thermal stability and conductivity, and large current carrying capacity, compared to copper [92]. On the other hand, small diameter s-SWNTs (large band gap) are ideal ballistic conductors for applications in field effect transistor (FET). However, the presence of m-SWNTs or even the large diameter of s-SWNTs (small band gap) can shorten the device [93].

Indeed, the growth control is the ideal method for sorting the SWNTs. This approach does not need additional treatment and could preserve the tubes' intrinsic properties. However,

this approach is not yet capable of satisfying the basic research and technical applications [94].

To date, post-growth separation approaches, such as dielectrophoresis [93, 95, 96], density gradient ultracentrifugation (DGU) [63, 71, 97, 98] and gel chromatography [99], are the most widely used routes for SWNT sorting. The dielectrophoresis method was first reported by Krupke *et al*. in 2003 [93]. They exploited the difference of relative dielectric constants between two types of SWNTs and developed alternating current (AC) dielectrophoresis. They reported that sorting SWNTs by electronic type (s-SWNT and m-SWNTs) could be successfully obtained by exploiting the difference in dielectric constant between s-SWNT and m-SWNTs. Dielectrophoresis is a simple and easy method for separation s-SWNT and m-SWNTs. However, the limitation of this method is the low yield, limited electronic purity of the separated tubes and not being suitable for chirality separation [94].

In 2005, Arnold *et al.* reported SWNTs diameter separation using the DGU [63]. In this process, the different structures of SWNTs have different densities, due to the selective adsorption of surfactants into the surface of the tubes. During the separation process, the different structures of the nanotubes move towards their isopycnic point, where their density positions along the centrifuge tube is equal to that of the surrounding medium.

Later, Feng *et al*. reported uniform DGU (U-DGU) with improved mass production for both s-SWNTs and m-SWNTs [100]. In this process, SWNT dispersion (after ultrasonication and pre ultracentrifugation) is mixed with the density gradient agent iodixanol and loaded to centrifuge tubes to separate the structure of SWNTs. Recent work on the optimization of this technique has resulted in an extraction yield of 65% and a purity exceeding 95% for both s-SWNTs and m-SWNTs [101].

Summarizing, the DGU technique shows a powerful ability for not only the separation of s-SWNTs and m-SWNTs but also the separation of various (n, m) chiralities. Although the separated s-SWNTs and m-SWNTs were commercialized, this method suffers from the disadvantages of high cost, and, moreover, is time-consuming, which thus extremely limits the yield of the separated nanotubes, especially the single-chirality nanotubes [94, 102].

As an alternative approach, Kataura *et al*. developed a gel chromatography technique. In 2008, they reported the use of gel chromatography for the separation of SWNTs, which can be achieved by using gel electrophoresis. They demonstrated m-SWNTs were driven from the input end of a gel column to the other under the electric field due to their weak adsorption onto the gel, whereas the s-SWNTs were absorbed onto the gel medium and remained stationary [103]. Over the past years, the Kataura group has successfully demonstrated the large-scale separation of single-chirality using the gel chromatography method [104-106]. Recently, it has proposed an advanced approach via column chromatography using mixed surfactants. They reported that the synergistic effect of the triple surfactants could be used

to amplify the difference in the surfactant coverage around different nanotubes to improve the separation efficiency, purity, and yields of SWNTs [106]. Using this technique, they successfully separated 12 different *(n,m)* single-chirality species of s-SWNTs with the purity exceeding 90%.

To sum up, among the discussed approaches, gel chromatography exhibits high resolution for sorting different-structure SWNTs and producing single-structure chirality with identical properties. Additionally, gel chromatography methods are the most suitable for large-scale production.

The major limitation facing all the discussed methods is the dependence on initial high quality SWNT dispersions produced via ultrasonication process, where the SWNTs can be inherently defected during ultrasonication, resulting in the degradation of separation purity.

2.5   Optical characterizations

Optical absorption spectroscopy, photoluminescence (PL) and Raman are widely used as optical tools to characterize the carbon nanotubes. The techniques are readily available, relatively simple and can be done under standard laboratory conditions. Furthermore, the optical techniques are non-destructive and rely on the photon, a massless and charge-less particle, as a probe. In this section, I discuss the characterization of SWNTs' dispersion using optical spectroscopy techniques. Additionally, primary attention is given to the effect of isolated s-SWNTs and small-size bundles of nanotubes.

Since the discovery of carbon nanotubes, considerable efforts have been devoted towards understanding their physical and optical properties. The unique 1D structure of SWNTs leads to strong electron confinement, characterized by the electronic density of states (DOS) of the nanotubes. Such electron confinement gives rise to series of sharp peaks called Van Hove singularities, which represent the electronic and optical properties of the nanotube. The Van Hove peaks correspond to energy levels, commonly abbreviated as E_{ii}, where E represents the optical energy transition from E_i in the valence band to E_{ii} in the conduction band. For the first time in 1999, Kataura *et al*. calculated the bandgap energies for SWNTs and revealed the energy separation between the Van Hove singularities as a function of the diameter of the tube [107]. Figure 2.6 shows the schematic for Van Hove peaks related to electronic state density of s-SWNTs. The figure presents an example for absorption of a photon in the high energy band at E_{22} (V_2 to C_2) and its subsequent emission near low energy band E_{11} (C_1 to V_1) after non-radiative relaxation of the electron in the conduction band (C_1) and hole in the valence band (V_1).
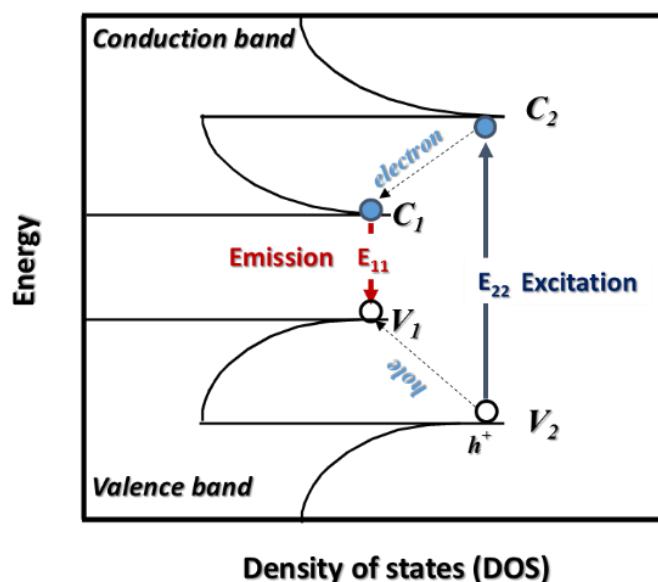
Figure 2.6: Schematic representation for density of electronic state of semiconductor SWNTs. The sharp peaks represent Van Have singularities.

Later, it turned out that, due to the existence of excitonic effects in the nanotubes the single-particle picture is not enough for a detailed analysis. The first direct proof for excitonic effects in SWNTs was experimentally demonstrated in 2005, using two-photon PL excitation spectroscopy [108, 109]. It is now generally accepted that exciton dominates the optical properties of the nanotubes, including the optical dynamics and optical nonlinear response, even at room temperature [110].

2.5.1 Optical absorption

UV/Vis/NIR absorption spectroscopy has proven to be a reliable and inexpensive technique for SWNT samples' characterization. It is capable of revealing the physical and electronic properties of SWNTs within liquid dispersion or composites.

A standard technique for optical absorption measurement consists of a light beam of selected wavelength transmitted from an optical monochromator passing straight through the sample and into the detector. The response of the s-SWNTs to the incident light beam is dominated by a sharp interband transitions arising from a series of Van Hove singularities [111]. Figure 2.7 presents absorption spectra for carbon nanotubes with different growth methods, i.e. LAs (curve 1), HiPco (curve 2), AD (curve 3), CoMoCAT (curve 4) and DWNTs (curve 5). The shape of the peaks is widely used to probe the presence of isolated SWNTs [15, 55, 112]. For example, curve 2 in figure 2.7 represents three main absorption bands in the spectrum, due to SWNT interband transitions. The spectral features from 1600 to 1100 nm and from 900 to 700 nm match the first (E_{11}) and second (E_{22}) excitonic transitions of s-SWNTs, respectively [15, 107].The spectral feature below 550 nm is related to the M_{11}

transition of m-SWNTs [107]. Moreover, these peaks can broaden and redshift as a result of SWNTs bundling [19, 113-116]. On the other hand, the shift in the absorption spectra is also attributed to the dielectric constant (ε) of the surrounding environment [113, 117-119].
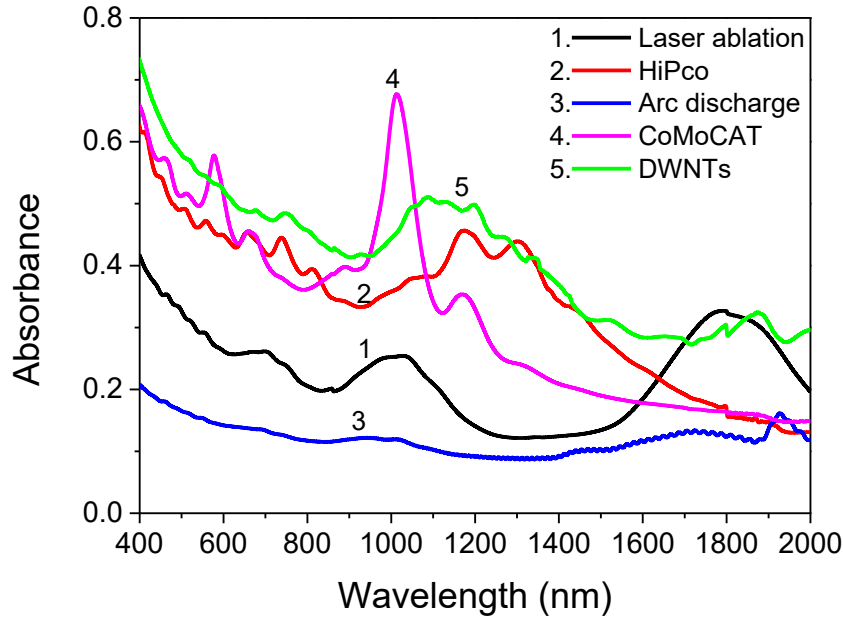
Figure 2.7   Absorption spectra for different types of carbon nanotubes hosted in PVA composite: laser ablation (LA) (1), HiPco (2), arc discharge (3), CoMoCAT (4) and DWNTs (5)

Curve 5 in figure 2.7 exhibits two absorption bands for DWNT spectrum (max at $\sim$ 1100 nm and $\sim$ 1900 nm), which are a combination of excitonic transitions from both inner and outer walls of DWNTs' structure [120, 121]. This corresponds to the tube diameter range from 0.75 to 1.15 nm (E_{11} at $\sim$ 1100 nm) and 1.5 to 1.9 nm (E_{11} at $\sim$ 2000 nm and E_{22} at $\sim$ 1100 nm) [120, 122], respectively. Additionally, this matches with the statistical DWNTs' inner and outer diameter distributions [120]. The 8% of the existing SWNTs in the sample have a diameter range similar to that of the inner wall of DWNTs. Therefore, E_{11} absorption of these SWNTs also contributes to the $\sim$ 1100 nm absorption peak from the E_{11} of inner and E_{22} of the outer walls of DWNTs.

Estimation of SWNTs' concentration in the final SWNTs' dispersion is commonly carried out using optical absorption spectroscopy. In the absence of scattering losses, the absorbance of SWNTs' dispersion is related to its concentration by the Beer-Lambert law:

$$A_{\lambda} = \alpha_{\lambda}.l.C \hspace{6cm} \text{Equation (2.5)}$$

where *C* is the concentration of SWNTs in the dispersion (g. L $^{-1}$), A_λ is the absorbance of the SWNTs at known wavelength λ (in arbitrary units), α_λ is the corresponding absorption coefficient (Lg^{-1}. m^{-1}) and *l* is optical path length in (m).

It is essential to measure the value of α_λ at different wavelengths from a set of SWNTs' dispersions with known concentration [78, 79, 83]. These wavelengths are carefully chosen to match the distinct peaks of the SWNTs in the absorption spectra. The obtained values of α_λ can then be used to assess the concentrations of SWNTs in the unknown SWNTs' dispersion. Additionally, the absorption coefficients for HiPco [56, 78, 79, 83, 123] and CoMoCAT [124] are previously reported in the literature at different absorption wavelengths for a range of liquids. For example, reference [78] reported the absorption coefficient for HiPco nanotubes dispersed in NMP at $\alpha_{660\ nm}$ =3250-3500 L g^{-1}.m^{-1} for a concentration of 0.1-0.001 g/L. Later, Hasan *et al*. estimated the absorption coefficient for the same dispersion at different wavelengths and reported $\alpha_{660\ nm}$ =4200 L g^{-1}.m^{-1} [79]. The difference between the two values can be explained by the different sample processing conditions. Additionally, reference [79] considered the presence of the 20 wt% of impurities and excluded them from the total used concentration in the HiPco powder. Therefore, for reliable estimation, it is crucial to consider comparable sample parameters involved in preparing the SWNTs' dispersion before using absorption coefficients from the literature to estimate the nanotubes' concentration. These parameters include materials properties, sonication (bath or tip sonication) and filtration (centrifugation or vacuum filtration).

2.5.2 Photoluminescence

Photoluminescence (PL) spectroscopy provides another optical characterization technique for SWNTs in liquids and composites. The first demonstration of PL for SWNTs goes back to 2002, when O'Connell *et al*. reported, for the first time, fluorescence across the band gaps of individual SWNTs in aqueous dispersion [15]. s-SWNTs fluorescence is remarkably photo-stable with no evidence of blinking or photo-bleaching after extended exposure to excitation [21]. Basically, the nanotubes (excited at the visible wavelengths) emit PL in the NIR range. Figure 2.8 illustrates different representations of PL data for SWNTs' dispersion in DI water, such as 3D (figure 2.8a) and 2D (figure 2.8b) maps for SWNTs' dispersion in deionized water (DI). Additionally, these maps can be further analyzed by extracting the PL intensity as a function of emission (figure 2.8c) or excitation (figure 2.8d) wavelengths.
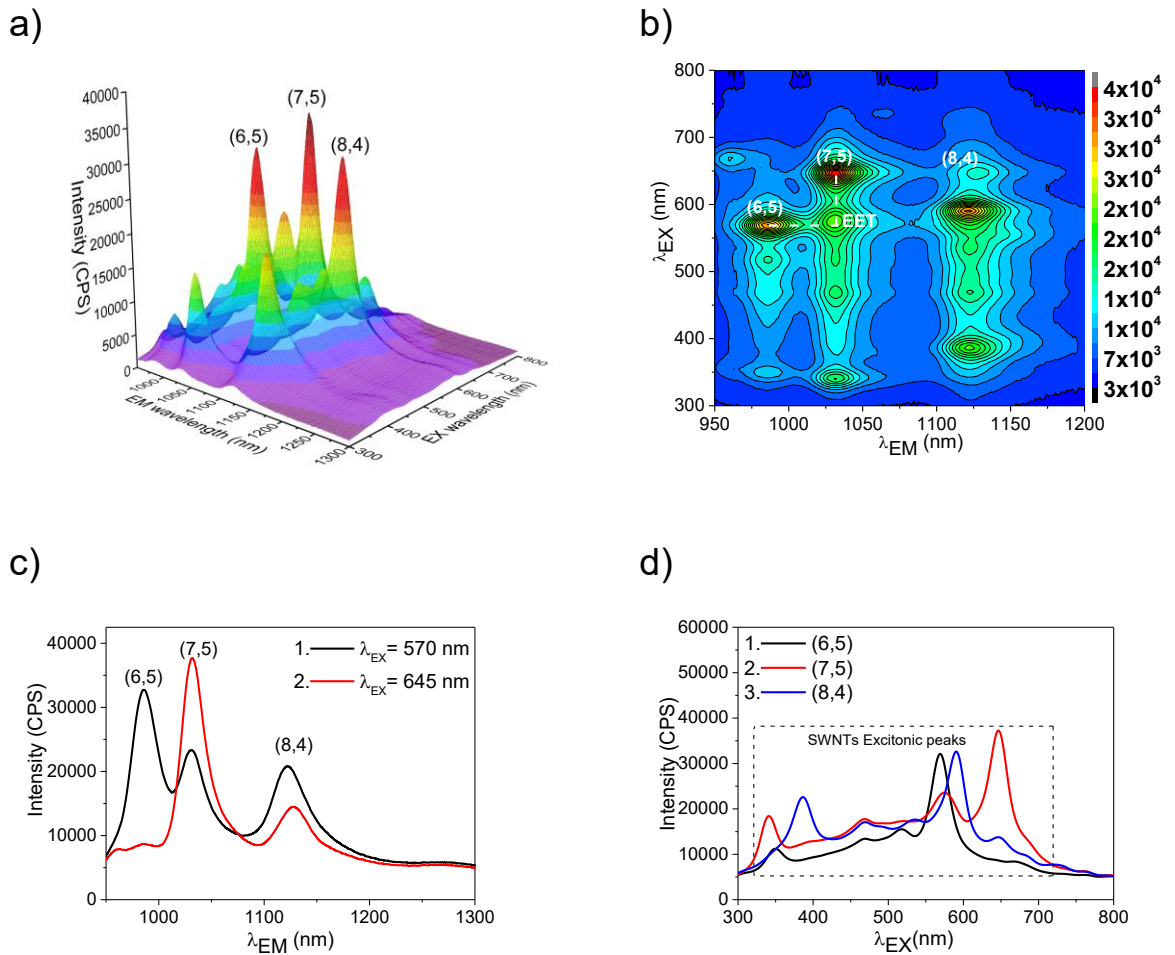
Figure 2.8   Examples of PLE map 3D (a), 2 D (b) and PL emission (c), PL excitation spectra for (6,5), (7,5) and (8,4) chiralities (d) for CoMoCAT SWNTs dispersion in DI water.

In PL excitation-emission (PLE) maps, the PL intensity is recorded in NIR range as a function of excitation (λ_{EX}) and emission (λ_{EM}) wavelengths. The excitation occurs at λ_{EX} = E_{22}, E_{33}, and E_{44} (300-800 nm), while λ_{EM} is only at E_{11} (950-1250 nm) [125, 126]. The resulting PL peak corresponds to the bandgap of each s-SWNTs (n, m) chiralities of the nanotube in the sample (figure 2.8). This typically corresponds to (6,5), (7,5), and (8,4) chiralities of the SWNTs, as shown in figures 2.8 a-b. Additionally, the PLE map in figure 2.8b near (570 nm, 1025nm) is associated with the resonant excitation of eh_{22} (6,5) sideband and emission from eh_{11} of (7,5). Tan *et al* [116] reported this feature due to energy transfer from the excitonic sidebands of the eh_{22} excitons from (6,5) donors to eh_{11} of (7,5) acceptors.

Moreover, PL emission from the nanotubes can be detected only from individual s-SWNTs and small size bundles of tubes. However, the presence of m-SWNTs in the bundles promotes overall metallic behaviour and results in quenched PL. The PL quantum yield for SWNTs was reported in the range up to a low percentage [19, 20], and it was further improved to 20% by optimizing the dispersion procedure of individual nanotubes [127].

Furthermore, Weisman and Bachilo defined E_{11} and E_{22} energy transitions as a function of chirality *(n,m)*. for a wide range of s-SWNTs [128].

SWNTs' PL peaks can shift in the emission wavelength or change in their intensity, due to changes in the surrounding environment. This opens the horizon to build efficient sensitive and robust optical sensors in complex chemical and biological environments.

2.5.3 Raman spectroscopy

Raman spectroscopy is the most sensitive optical tool to investigate the structure of carbon nanotubes before dispersion (in powder) and after (in liquid, or film) forms. Moreover, it is very informative and can be used to study several parameters, such as diameter, chirality, metallic or the semi-conducting nature of the tubes and quality of the sample. For example, figure 2.9 presents typical Raman spectra for SWNT/PVA composite. The spectra consist of four bands in the studied range, namely radial breathing mode (RBM, 150-300 cm^{-1}), Disordered (D-mode, ~1350 cm^{-1}), graphite (G mode, 1590 cm^{-1}), and 2D mode (second-order Raman scattering from D-band variation, also called G', ~2500-2900 cm^{-1}).

The RBM mode is the most important feature and appears only in carbon nanotubes as well as fullerene structures [129, 130]. This mode is used to estimate the diameter and chirality of SWNT [131]. Moreover, the frequency of the RBM mode (ω_{RBM}) is inversely proportional to the tube diameter (d_t) and located at the frequency range ω_{RBM} =120 - 250 cm^{-1} corresponds to tubes diameters 1-2 nm. These features are helpful for determining the nanotube diameters using the following relation:

$$\omega_{RBM} = A / d_t + B \qquad\qquad\qquad \text{Equation (2.6)}$$

where *A* and *B* are constants and can be obtained experimentally. For example, reference [132] have reported *A* = 234 cm^{-1} and *B* = 10 cm^{-1} for SWNT bundles. On the other hand, reference [131] have reported *A* = 248 cm^{-1} and *B* = 0 for isolated SWNTs on an oxidized silicon substrate.
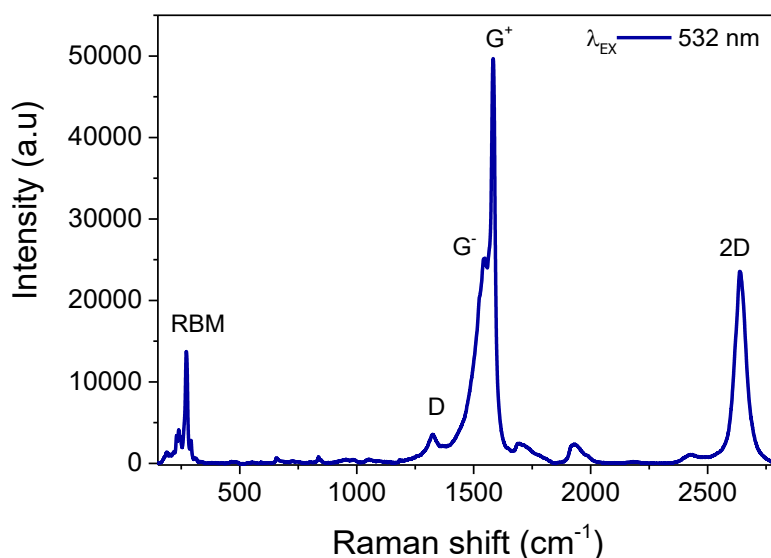
Figure 2.9   Raman spectrum for SWNT/PVA composite measured at excitation wavelengths 532 nm.

Raman spectroscopy is a valuable tool to determine the defects that have occurred on the surface of the tubes during the sample preparation by monitoring the increase in the intensity of D mode [133-135]. This mode occurs due to the breathing mode of the hexagonal ring of the carbon atom, and it is located in the frequency range 1200 and 1400 cm^{-1} [133-135]. The ratio of intensity at the D peak to the G peak (I_D/I_G) is widely used to probe the structural quality of SWNTs samples [136]. For example, I_D/I_G can be used to determine the possible defects in the nanotube, due to the sample preparation process as well as laser irradiation damage for SWNTs/PVA composite.

While the G band in graphite is dominated by a single strong peak at 1582 cm^{-1}, the G band in SWNTs features with two strong peaks (G+ and G-). The splitting of these peaks resulted mainly from the tube curvature. The overall shape and intensity of the G band can be used to determine whether the tubes are m-SWNTs or s-SWNTs.

The 2D-band is second-order Raman scattering from D-band variation, and it is located at 2600 cm^{-1}. The spectral position of 2D mode depends on the tubes' diameter, so it can be used to estimate the SWNTs' diameter [137].

Additionally, reference [138] performed Raman studies for SWNTs-surfactant-dye system. They reported no significant shifts in the intensity or position of D, G and 2D modes for the mixture of dye with SWNTs compared to neat SWNTs. Furthermore, no signatures of new chemical bonds were reported. Therefore, they explained the interaction of the cationic dye and anionic micelle SWNTs by non-covalent interaction (Coulomb attraction).

2.6 Photonics applications

SWNTs are known for their fascinating physical properties that are paving the way for the design and implementation of promising devices, including light harvesting, photonics sensors, drug delivery, and energy storage systems [3, 50, 51, 139]. Moreover, SWNTs' surface offers strong interactions with the surrounding environment that can result in a remarkable change of their properties. The intrinsic PL emission of SWNTs can shift and/or change when interacting with molecules, indicating alteration of their electronic properties [140, 141]. On the other hand, the advantage of the nanotubes interacting with the surrounding environment can be exploited to develop new functional materials and build efficient sensitive and robust optical sensor. For example, the recent work on a new mechanism for detection of SWNTs dispersed with anionic surfactants in water using cationic dyes shows the formation of a very promising three-component system made of dye-surfactant-SWNT [138]. The three components in the system can interact, thus forming complexes with enhanced PL. The complexes have strongly increased PL intensity from SWNT levels in the NIR range, due to resonance energy transfer from the dye.

The most successful photonic application of SWNTs is SAs for ultrafast mode-locked fibre lasers. Currently, the commercially employed SAs are group III–V binary and ternary semiconductors in the structure of multi-quantum wells (MQWs). These are termed semiconductor SA mirrors (SESAMs). Compared to SESAMs, SWNTs feature broad spectral range, low saturation intensity, large third order nonlinear susceptibilities, faster recovery time and easy fabrication [5]. Ultrafast laser pulses (i.e. ps and fs) are in high demand in a wide variety of fields, including medical applications [26, 142, 143], time-resolved spectroscopy [26, 142, 143] and materials processing [26, 142, 144, 145]. To date, SWNT-based SAs have attracted significant research interest into mode-locked fibre lasers [25, 146-148], waveguide lasers [149, 150], solid-state lasers [151, 152], and semiconductor lasers [153], for broad operation wavelengths ranging from 780 to 2000 nm [25, 154-164].

2.7 Chapter conclusion

The unique optical properties of SWNTs promote them as a potential candidate for photonics applications. However, a gap still exists between the reported experimental results and the theoretical predictions [165-167]. Several fundamental processing challenges should be overcome to enable full utilization of optical properties of carbon nanotubes. The main difficulties with SWNTs are related to their heterogeneity, presence of impurities and dispersibility in the liquid phase. There are still various improvements needing to be done for the development of SWNTs for photonic applications, such as

stability of SWNTs' dispersion over time, controlling SWNTs' bundle (e.g., size of the bundle, the ratio of s-SWNTs to m-SWNTs in the bundle …. etc.) to enhance their optical properties.

Chapter 3: Dioxaborine dye as a selective photoluminescence probe for single-wall carbon nanotubes

3.1 Introduction

Functionalization of nanostructured systems have different chemical compositions underpinning advance applications in nanotechnology. Particularly, one of the most important up-to-date challenges is the construction of photoluminescent nano-ensembles, which can be applied as effective chemical probes, labels for diagnostics and treatment of live tissues, etc. [4, 5, 7-10, 168]. Thus far, the two-component system made of single-wall carbon nanotube (SWNT)/surfactant has been extensively studied to produce highly stable SWNT dispersion, considering attraction of the hydrophobic part of the surfactant to the SWNT surface. However, SWNT/surfactant systems demonstrate NIR range photoluminescence (PL) with the PL quantum yield in the range up to a low percentage [19, 20]. The increase in the PL signal from SWNTs was reported in the literature via covalent formation of sp^3 defects on the SWNT surface [169], encapsulation of small organic molecules inside the SWNTs [170] and non-covalent functionalization of the tube surface with π-conjugated organic compounds [171-173]. Non-covalent functionalization using surfactants is an attractive route to achieve homogenous dispersions with a high concentration of SWNTs. In general, non-covalent functionalization preserves the physical and electronic properties of the nanotubes, at the same time giving them novel advantages associated with the organic conjugates [50, 51].

The recent work on a new mechanism for detection of SWNTs dispersed with anionic surfactants in water using cationic dyes shows the formation of a very promising three-component system made of dye-surfactant-SWNT [138]. The three components in the system can interact and thus form complexes with enhanced PL. The complexes have strongly increased PL intensity from SWNT levels (E_{11}) in NIR range, due to resonance energy transfer (RET) from dye. However, the limitation of the studied cyanine based complex is the RET in the range of PL excitation wavelengths, where the SWNTs have strong intrinsic emission [138]. Therefore, PL intensity is increased relatively to SWNT intrinsic emission, so the complexation effect has limited relative sensitivity.

This chapter focuses on studies of an interaction of the SWNT with indopentamethinedioxaborine dye (DOB-719) having an extended π-conjugated system (figure. 3.1) and absorption in NIR range. The choice of the dye is motivated by its unique interaction with the SWNT, which has resulted in the development of new PL peaks in the

range of excitation wavelength at 650-780 nm, where the PL emission of the SWNT is very low.
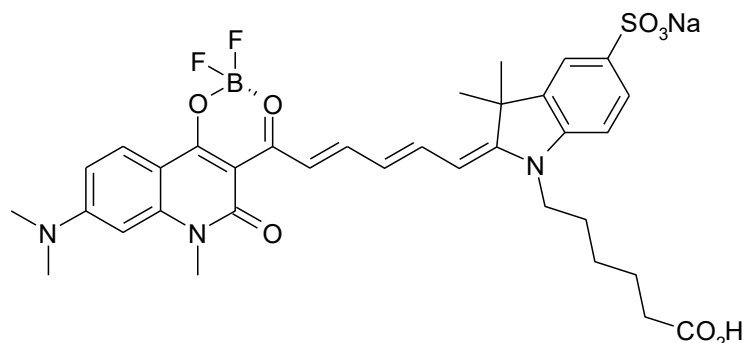
Figure 3.1 Molecular structure of DOB-719

Generally, polymethine dyes with dioxaborine terminal group own intense PL signals, efficient two-photon absorption, high hyperpolarizability [174], and features of effective PL probe for amines and ammonia [175-177]. Optical properties (absorption and PL) of monomeric and dimeric forms of DOB-719 were reported by Shandura *et al* [177] showing that there are weak interactions of the SWNT with DOB-719. The novelty of this study is in the elucidation of the interaction between the dye and SWNT, providing clear evidence of the RET from DOB-719 to the SWNT [178]. The obtained results from this study allowed the proposal to mechanism of interaction between the SWNT and DOB-719, where the dye is attracted to the SWNT surface via π-π stacking, with the hydrophobic part facing the aqueous medium by polar groups [178].

3.2   Materials and methods

3.2.1   Materials

The indopentamethinedioxaborine dye (DOB-719) used in this study was supplied by the Institute of Organic Chemistry (NASU, Ukraine). Further details about purity and synthesis of the dye is reported by reference [178]. According to the SouthWest NanoTechnologies (SWeNT Inc). technical data sheet, SWNT (purchased from SWeNT Inc., CG100, Lot # 000-0012) powder has carbon purity of 90 wt% with nanotube diameters distribution from 0.7 -1.3 nm.

Dispersions of SWNT were prepared using a range of surfactants. The choice of surfactants is motivated by their efficiency in dispersing SWNTs [72]. This includes anionic surfactants, such as sodium dodecylbenzene sulfonate (SDBS), sodium taurodeoxycholate (STDOC),

sodium deoxycholate (SDOC). Furthermore, neutral surfactant, polyvinylpyrrolidone (PVP) and the cationic surfactants cetyltrimethylammonium bromide (CTABr), cetylpyridinium chloride (CPCL) were also used to study their effect on RET. Figure 3.2 presents the molecular structure of surfactants used in this study.
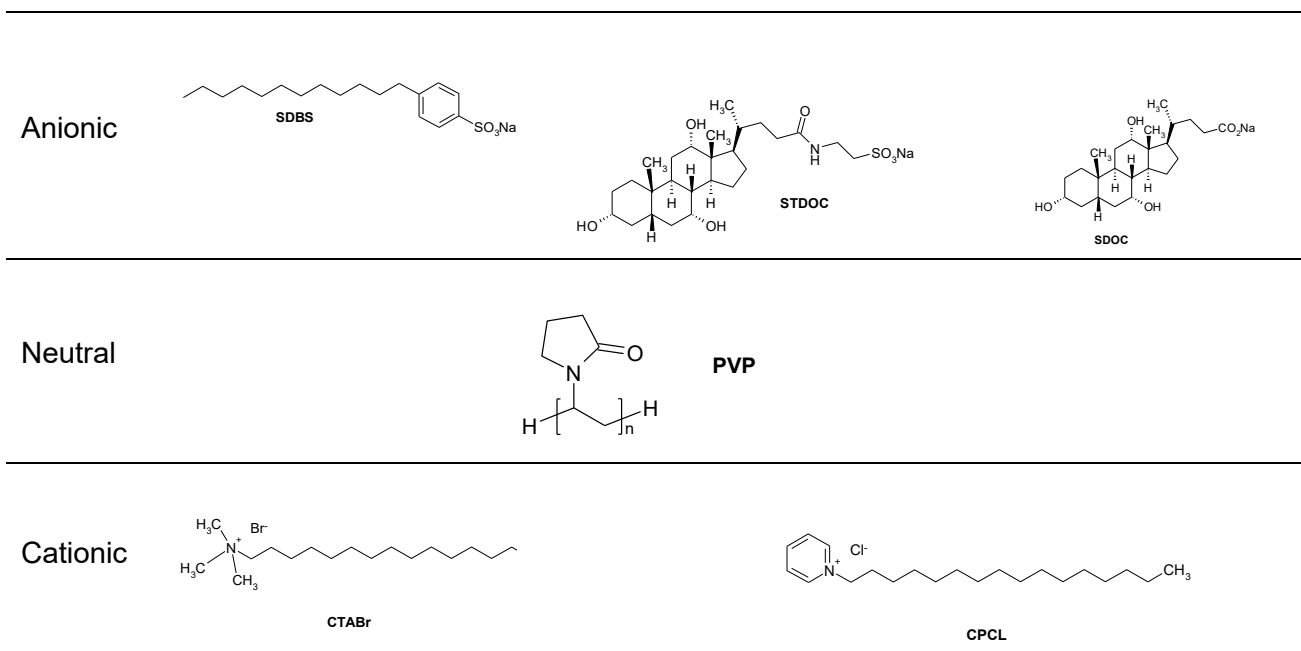
Figure 3.2   Molecular structure of surfactants used in this study. Abbreviations: SDBS: sodium dodecylbenzene sulfonate, STDOC: sodium taurodeoxycholate, SDOC: sodium deoxycholate, PVP: polyvinylpyrrolidone, CTABr: cetyltrimethylammonium bromide, CPCL cetylpyridinium chloride.

3.2.2 Sample preparation:

In this section, I describe the sample preparation procedure. The samples under study are neat SWNT dispersions, dye solutions and mixtures of SWNT, with dye as prepared and aged (measured 24 hours after the mixing) all in deionized water (DI). Table 3.1 shows different amount of initial SWNT dispersions used to prepare mixtures of DOB-719 and SWNTs with various surfactants. I used different amounts of initial SWNT dispersions because of different efficiency of the used surfactants to yield various concentrations of nanotubes in the dispersions. 1.2 mg of SWNTs (CoMoCAT CG 100) was dispersed in 20 mL of DI water in the presence of one of the surfactants mentioned in table 3.1. The use of higher amounts of Triton X-100 and PVP is justified by the need to increase the concentration of individual tubes to have a reasonable PL signal from their dispersions. Whereas, the different concentration of surfactants at the initial SWNTs dispersion (table 3.1) was chosen to maintain the surfactant concentrations at CMC [179]. Next, the mixtures

of SWNTs and surfactant in DI were subjected to ultrasonication using a NanoRuptor (Diagenode) processor for one hour at 21 kHz and 250 W. Then, the mixture was ultracentrifuged using Beckman Coulter Optima Max-XP for two hours and 30 minutes at 17 °C using (MLS 50 rotor) at 45000 RPM. The top 70% of the final dispersion was used as an initial SWNTs dispersion to carry out this study. Importantly, the concentrations of specific SWNTs in all the mixtures and neat SWNT dispersions were the same in our experiments, unless otherwise stated.

Table 3.1: Surfactant parameters for SWNTs' dispersions used in this study.

Surfactant		Initial concentration (mg/mL)	Relative SWNTs concentration used from the initial SWNTs dispersion to prepare the dye-SWNTs mixture (%)
Anionic	SDBS	0.33	20
	STDOC	0.28	10
	SDOC	0.33	3
Neutral	Triton X-100	0.85	95
	PVP	0.98	95
Cationic	CTABr	0.37	20
	CPCL	0.06	20

3.2.3   Experimental setup

The optical absorption spectra were recorded using Lambda 1050 UV/VIS/NIR (Perkin Elmer) spectrometer with 1.5 nm increment. According to the technical specifications of Lambda 1050 UV/VIS/NIR, the spectrometer has wavelength accuracy of ± 0.08 nm at UV/Vis and ± 0.3 nm at NIR. The deionized water (DI) was used as a reference in all measurements of the absorption spectra. The PL emission spectra at various excitation wavelengths were registered, using a Horiba NanoLog excitation-emission spectrofluorometer equipped with an InGaAs array detector (cooled by liquid nitrogen) and Si detector. The PL measurements in the NIR were recorded using entrance/exit slits of 14 nm in width for both the excitation and emission monochromators. An entrance/exit of 2 nm slits was used for both the excitation and emission monochromators in the visible range measurements. According to the technical specifications, the NanoLog excitation monochromator accuracy is 0.5 nm and 0.3 nm emission imaging spectrograph.

3.3   Results and discussion

This section presents experimental studies on the interaction of DOB-719 and SWNTs using absorption and photoluminescence (PL) spectroscopy. First, subsection 3.3.1 characterizes the effect of the dye concentration on the energy transfer to the tubes. Next, the effect of dye ageing using as prepared and aged (measured 24 hours after the mixing) solutions of neat DOB-719 and mixtures of DOB-719 with the SWNT in water is studied in subsection 3.3.2. Then, SWNT dispersions in the presence of anionic, cationic, and neutral surfactants are separately examined in subsection 3.3.3 to compare their PL spectral properties, particularly at excitation wavelength (λ_{EX}) = 735 nm, where the RET has its maximum.

3.3.1   Effect of DOB-719 concentrations on energy transfer to SWNT

Weak interaction of the SWNT with DOB-719 was reported in the literature [177]. Shandura *et al*. have used high concentrations of the dye (0.001-0.02 mg/mL) in their studies, showing low PL emission from the E_{11} levels of SWNTs in NIR range with λ_{EX} = 700-760 nm and thus evidencing weak interaction of the SWNT with DOB-719. Recently, we have revealed that at lower concentrations of the dye, the features of the interaction of SWNT and DOB-719 become much stronger, resulting in the emergence of new spectroscopic features[178]. I studied DOB-719 concentrations of 0.00025, 0.0005, and 0.001 mg/mL observing strong interaction of the dye with SWNTs dispersed using SDBS. The choice of SDBS can be explained with high efficiency in dispersing SWNTs, due to the presence of a small head group with the benzene ring and long alkyl chain [54].

The normalized absorption spectra of DOB-719 in water shown in figure 3.3a define the presence of monomeric form (free molecules) of the dye with a maximum spectral peak at wavelength λ_M = 687 nm. Moreover, λ_M is constant, regardless of the dye concentration, with good agreement with Shandura *et al*. [177]. Additionally, an increase of the concentration of the dye in aqueous solution above 0.001 mg/mL results in growing contribution of DOB-719 dimers (two dye monomers attached together) featured by a blue-shifted peak. A growth of the second maximum in the spectral range of 600–650 nm occurs at concentrations higher than 0.00025 mg/mL evidencing formation of DOB-719 dimers. The dimers start to form considerably at the concentrations higher than 0.00025 mg/mL resulting in growth of the second maximum in the spectral range of 600–650 nm as shown in figure 3.3b. Based on Gaussian deconvolution, the second vibrational transition of the dye monomers has a band with a maximum at absorption λ = 629 nm and dimeric peak at

the absorption λ = 600 nm. Additionally, Gaussian deconvolution confirms the dye monomer peak at λ_M = 687 nm.

a)

b)
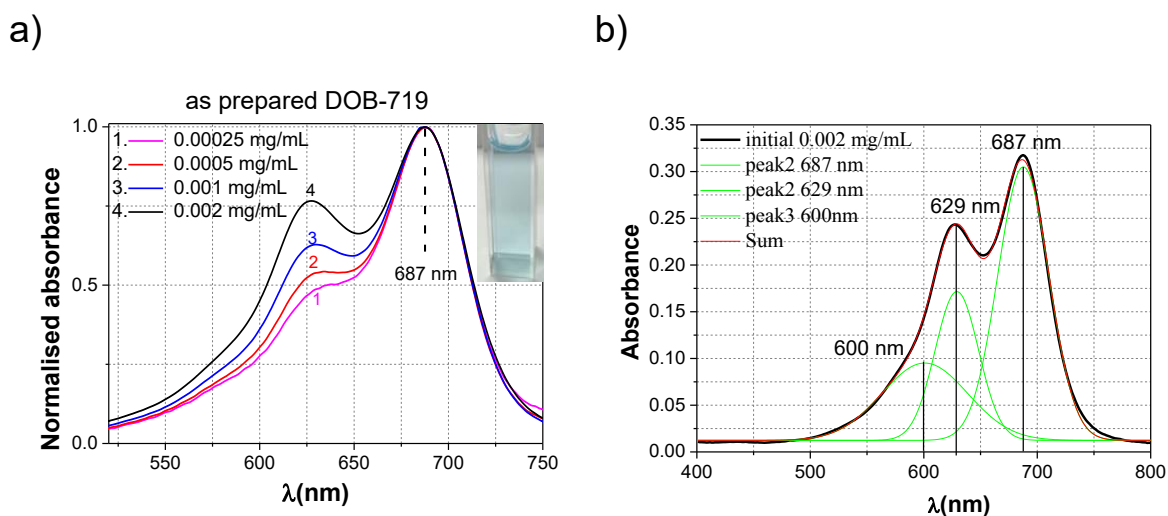
Figure 3.3   a) Normalized absorption spectra for aqueous solutions of as prepared DOB-719 concentrations of 0.00025 mg/mL (1), 0.0005 mg/mL (2), 0.001 mg/mL (3) and 0.002 mg/mL (4). b) Deconvolution of absorption spectrum for DOB-719 at concentration 0.002 mg/mL. Inset: Aqueous solution of as prepared DOB-719 at concentration of 0.001 mg/mL.

Figure 3.4 shows the absorption spectra for the mixtures of DOB-719 and SWNT at the studied dye concentrations. The absorption of neat SWNT dispersion in the range of 400-800 nm (figure 3.4a, curve 1) characterizes low-intensity E_{22} and M_{11} excitonic transitions [128]. The absorption spectra for the mixtures of DOB-719 with SWNTs features a new absorption peak at λ =742 nm, regardless of the dye concentration in the mixtures (figure 3.4a, curves 3-5). Importantly, the absorption spectrum for SWNT mixture containing DOB-719 at a concentration of 0.001 mg/mL (figure 3.4a, curve 3) resulted in two maxima at absorption wavelengths 692 nm and 742 nm. The former peak is a signature of the dye monomers in the mixture and the latter peak corresponds to the dye molecules associated with the SWNTs. On the other hand, SWNTs' dispersion, containing dye at concentrations lower than 0.001 mg/mL (curves 4-5 in figure 3.4a) displayed no peak corresponding to the dye monomer at absorption wavelengths 692 nm. This finding indicates that all dye molecules at concentrations below 0.001 mg/mL are complexed with SWNTs. However, at a dye concentration of 0.001 mg/mL (figure 3.4a, curve 3) the monomer signature appeared at λ =692 nm, evidencing the presence of free DOB-719 molecules in the mixture.

To sum up, the presence of the DOB-719 at a concentration of 0.001 mg/mL at SWNTs' dispersion resulted in the emergence of the new 50 nm redshifted absorption peak (figure 3.4a, curves 3), compared to the peak of DOB-719 monomer (figure 3.4a. curve 2). The

new peak can be explained with the complexation of the dye with the SWNT. Therefore, the ratio of absorption intensity for these peaks allows monitoring the amount of the dye monomers in the mixture as well as the amount of the dye complexed with the SWNT. Similar behaviour has been reported for the interaction of SWNT/porphyrin, where a 20 nm split in the porphyrin band was observed, due to the presence of the nanotubes [180]. Figure 3.4b, curve 1 presents the absorption spectrum of the neat SWNT in the range of 950-1200 nm exhibits E_{11} peaks at λ = 986, 1031, and 1127 nm. These peaks correspond to E_{11} excitonic transitions of chiralities (6,5), (7,5) and (8,4), respectively [128]. The presence of DOB-719 in the SWNTs mixture resulted in redshifted E_{11}^* peaks (figure 3.4b, curves 3-5), compared to neat SWNTs dispersion.

a)   b)
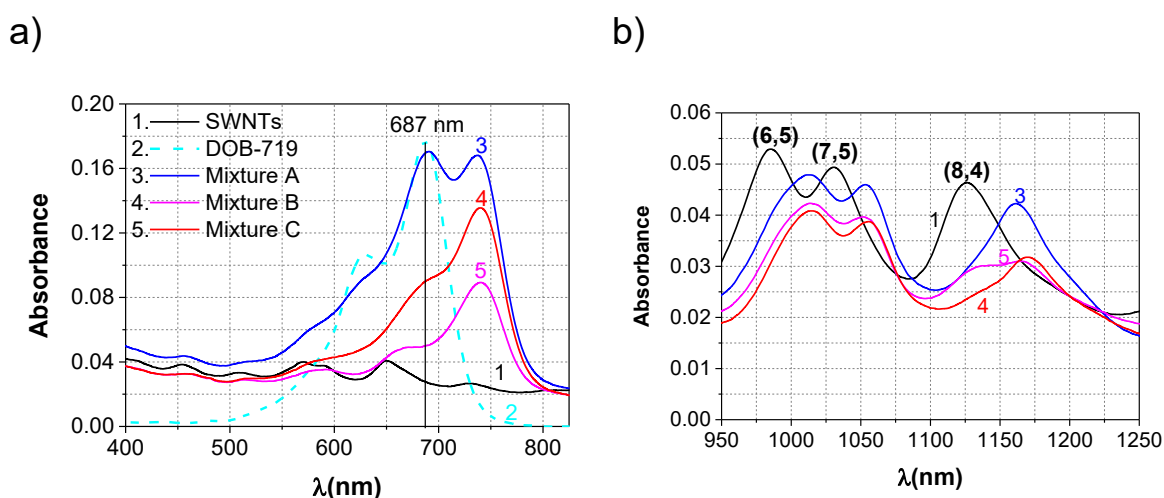
Figure 3.4   Absorption spectra in (a) visible and (b) NIR ranges for dispersions of SWNT with SDBS (1), as prepared aqueous solutions of neat DOB-719 at concentration of 0.001 mg/mL (2), mixtures of as prepared DOB-719 with SWNT at DOB-719 concentrations of 0.001 mg/mL for mixture A (3), and 0.0005 mg/mL for mixture B (4) and 0.00025 mg/mL for mixture C (5).

Table 3.2 summarizes the E_{11} and E_{11}^* absorption peak positions for neat SWNTs' dispersion and the mixtures of DOB-719 with SWNTs, respectively. Peaks corresponding to (6,5) chirality are redshifted in the range 25-30 nm, whereas (7,5) peaks are redshifted in the range of 21-24 nm, due to raising the concentration of the dye in the SWNT mixtures (table 3.2). However, the E_{11} peak corresponding to (8,4) chirality displays different scenario compared to (6,5) and (7,5) chiralities. Mainly, the admixture of DOB-719 at the lowest concentration (0.00025 mg/mL) to SWNT (figure 3.4b, curve 5) resulted in a decreased peak intensity for (8,4) chirality, compared to neat SWNTs (at λ =1127 nm) and formation of a new peak at λ =1176 nm, related to the dye molecules associated with the SWNT. Thus, increasing the dye concentration in the mixtures diminishes further the neat SWNT contribution and enhances the redshifted E_{11}^* peak for SWNTs interacted with dye.

From this observation, a new mechanism describing the interaction of DOB-719 with nanotubes of all chiralities can be proposed. The admixture of the dye to SWNT results in a decrease of the E_{11} peaks for neat SWNTs and a formation of a new redshifted peak E_{11}^*, related to the dye molecules associated with the SWNT regardless of the chirality. Therefore, the observed effect for (8,4) chiralities could imply the same behaviour for (6,5) and (7,5) chiralities at dye concentrations below 0.00025 mg/mL.

Table 3.2: Peaks of absorption spectra for the neat SWNT dispersions (E_{11}) and the as prepared mixtures of SWNT with DOB-719 (E_{11}^*) at concentration of 0.00025, 0.0005 and 0.001 mg/mL.

SWNT predominant chirality		(6,5)	(7,5)	(8,4)
E_{11} peaks for dispersion of neat SWNT		986 nm	1031 nm	1127 nm
E_{11}^* peaks for as prepared mixtures of SWNT and DOB-719 at the following concentrations:	0.00025 mg/mL	1013 nm	1052 nm	1164.5 nm
	0.0005 mg/mL	1016 nm	1055 nm	1170.5 nm
	0.001 mg/mL	1011 nm	1053 nm	1161.5 nm
Redshifts $\Delta E_{11} = E_{11}^* - E_{11}$	0.00025 mg/mL	27 nm	21 nm	37.5 nm
	0.0005 mg/mL	30 nm	24 nm	43.5 nm
	0.001 mg/mL	25 nm	22 nm	34.5 nm

The E_{ii} transition energies of the nanotubes strongly depend on the dielectric constant of both the SWNTs and the background of their surrounding environment (ε_{bg}). The dielectric screening effect becomes particularly evident for SWNTs dispersed in liquids, compared to the nanotubes in the air [181]. Therefore, an increase of ε_{bg} results in a redshift of E_{ii} transition energies [181, 182]. In this work, the minimum shift obtained in E_{11} exciton energy is 21 nm (24 meV) for E_{11} peaks corresponds to (7,5) chirality due to the admixture of the dye to SWNTs (figure 3.4b, table 3.2). Moreover, the maximum is 43.5 nm (40.9 meV) for (8,4) chirality, due to the admixture of the dye to SWNTs (figure 3.4b, table 3.2), which is lower than the average shifts of $\Delta E_{11} = 55$ meV obtained in the literature [181]. On the other hand, the redshifts shown in table 3.2 are much lower than the redshift reported in reference [182], due to decreasing amounts of surfactant around nanotubes by dilution. In the studied complex of DOB-719 with SWNT, the local increase of ε_{bg} can be achieved in two ways; (i) better access of water to the SWNTs and/or (ii) by bringing polar groups of the dye near the nanotube surface. Thus, the observed redshifts of nanotube transitions at E_{11} can be

justified by the increase of ε_{bg} around the SWNTs, due to the presence of the DOB-719 molecules.

Figure 3.5 shows the PL excitation-emission (PLE) maps in the NIR range, with the X-axis representing emission wavelength (λ_{EM}) and Y-axis representing excitation wavelength (λ_{EX}) for the SWNT dispersed with SDBS (figure 3.5a) and as prepared mixtures of DOB-719 with the SWNT dispersion at different dye concentrations (figure 3.5 b-d). In figure 3.5a, the predominant (6,5), (7,5), and (8,4) chiralities of the SWNT in the studied dispersions are registered in the range of λ_{EX} at E_{22}, E_{33}, and E_{44} (300-800 nm) and λ_{EM} at E_{11} (950-1350 nm) [125, 126].

a)

b)

c)

d)
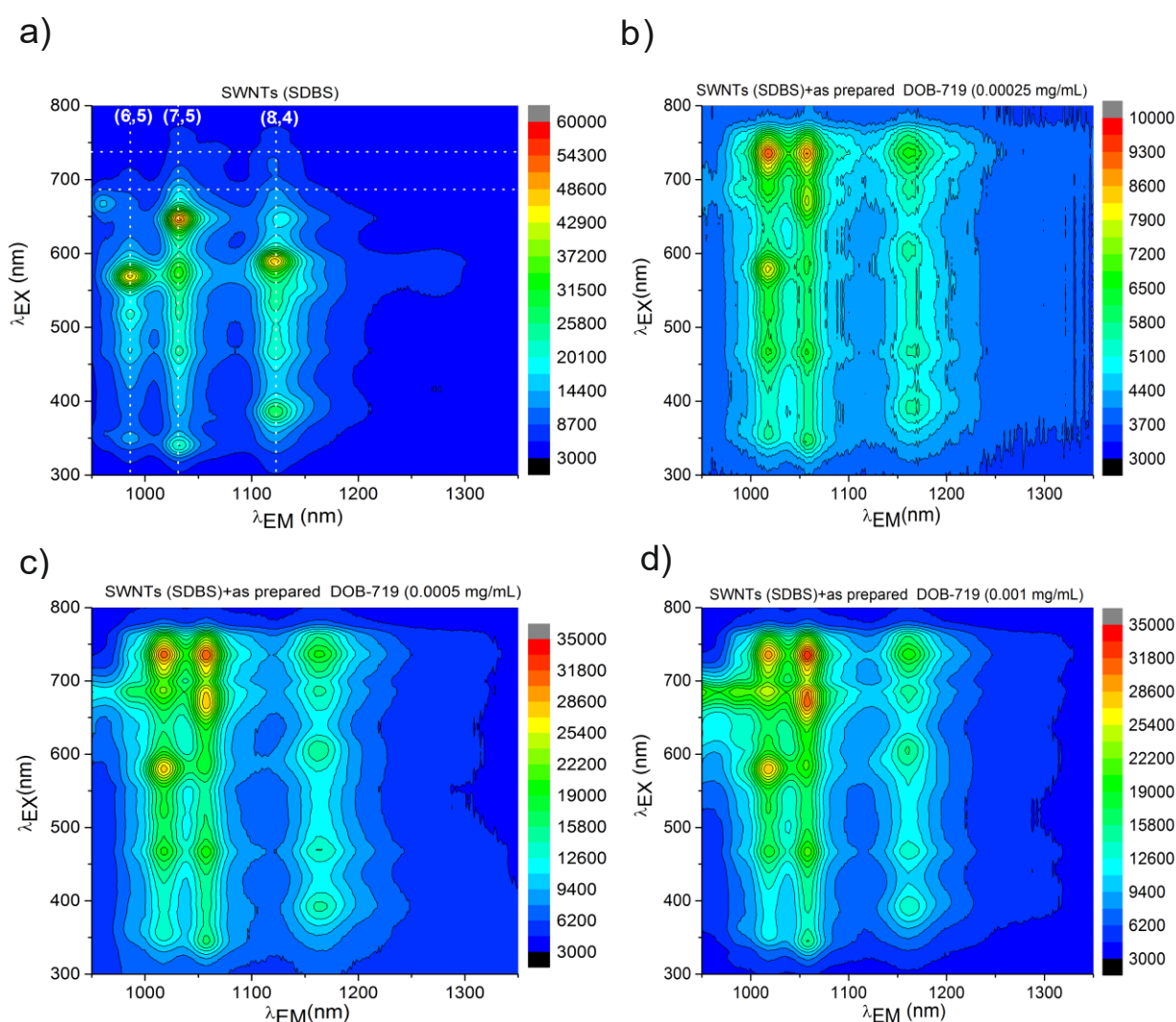
Figure 3.5   PLE maps for neat SWNTs' dispersion with SDBS (a) and mixtures of SWNTs with DOB-719 at concentrations of 0.00025 mg/mL (b), 0.0005 mg/mL (c) and 0.001 mg/mL (d). The vertical dashed lines show λ_{EM} for E_{11} of (6,5), (7,5), and (8,4) chiralities, The horizontal dashed lines show the position of new PL peaks at λ_{EX} = 735 nm (the RET from DOB-719 to the SWNT) and the position of DOB-719 monomers maximum at λ_{EX} = 685 nm. High PL intensities are indicated in red colour, whereas low intensities are indicated in blue colour.

Figures 3.5 b-c show additional new PLE features, compared to figure 3.5a in the range of λ_{EX} = 650-780 nm with a maximum PL inensity at λ_{EX} = 735 nm and $\lambda_{EM,}$ corresponding to the E_{11} SWNT emission. The new spectral features in the PLE maps for the mixtures of DOB-719 with the SWNT appear, due to the interaction of the dye with the nanotubes and development of nanostructure complexes, consisting of dye-surfactant-SWNT. A similar complexation phenomenon has been reported for SWNTs-astraphloxin system with a maximum PL intensity at λ_{EX} = 555 nm [138]. Importantly, at this excitation wavelength (λ_{EX} = 555 nm), SWNTs have stronge internsic emission specifically from (6,5) chirality. However, the excitation wavelength (λ_{EX} = 735 nm) for the SWNTs-DOB-719 system where the SWNTs' internsic emission is very low. Moreover, the SWNTs-DOB-719 system is distinct by a strong redshift of the intrinsic SWNT peaks in the λ_{EM} and quenching of these SWNT emission peaks. The strong redshifts for λ_{EM} maxima of the mixtures in comparison with the neat SWNTs for all chiralities are summarized in table 3.3.

Table 3.3: Peaks of PL emission spectra for the SWNTs dispersed with SDBS (E_{11}) and the mixture of SWNT and DOB-719 (E_{11}^{*}) at concentration of 0.00025, 0.0005 and 0.001 mg/mL.

SWNT chirality		(6,5) at λ_{EX} = 570 nm	(7,5) at λ_{EX} = 650 nm	(8,4) at λ_{EX} = 590 nm
λ_{EM} (E_{11} or E_{11}^{*})				
E_{11} peaks for dispersion of neat SWNT		987.0 nm	1032.1 nm	1120.5 nm
E_{11}^{*} peaks for as prepared mixtures of SWNT and DOB-719 at the following concentrations	0.00025 mg/mL	1017.7 nm	1056.8 nm	1160.3 nm
	0.0005 mg/mL	1018.8 nm	1057.1 nm	1163.7 nm
	0.001 mg/mL	1018.0 nm	1057.0 nm	1161.0 nm
Redshifts $\Delta E_{11} = E_{11}^{*} - E_{11}$	0.00025 mg/mL	30.7 nm	24.7 nm	39.8 nm
	0.0005 mg/mL	31.8 nm	25.0 nm	43.2 nm
	0.001 mg/mL	31.0 nm	24.9 nm	40.5 nm

The minimum and maximum redshifts observed at E_{11} peaks of PL emission spectra for mixtures of SWNT and DOB-719 in table 3.3 coincide with redshifts of E_{11} peaks obtained from absorption spectra in figure 3.4b (table 3.2). The minimum redshifts are observed for (7,5) chirality and the maximum ones are for (8,4) chirality. The variations in redshift for different SWNT chiralities (tables 3.2 and 3.3) can be explained by structural matching of the π-electron systems of specific chiral SWNT and extended π-electron system of the studied dye. The different redshifts provide not only another parameter for sensitivity to the nanotubes but also show selectivity of the PL detection towards the SWNTs' diameters.
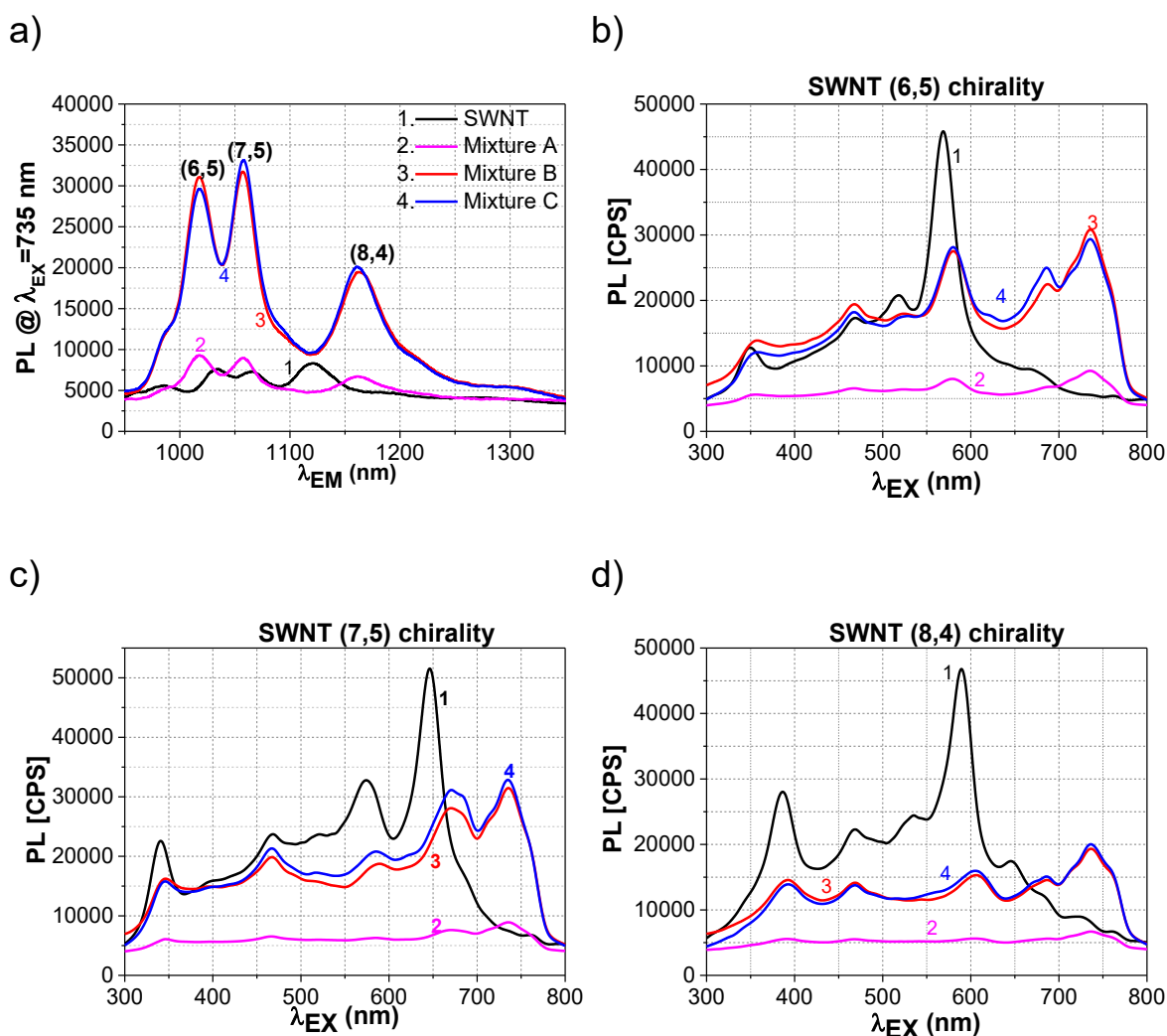
Figure 3.6   PL spectra for neat SWNTs' dispersion with SDBS (1) mixtures of as prepared DOB-719 with SWNT at DOB-719 concentrations of 0.00025 mg/mL for mixture A (2), and 0.0005 mg/mL for mixture B (3) and 0.001 mg/mL for mixture C (4). PL spectra at λ_{EX} = 735 nm (a) and PL excitation spectra for (6,5) (b), (7,5) (c), and (8,4) (d) chiralities. λ_{EM} for excitation spectra (1-4) are mentioned in table 3.3 as E_{11} and $E_{11}*$ peaks of PL emission spectra.

The PLE maps in figure 3.5 were analyzed to have a better understanding of the new spectral features. For this, the PL emission (figure 3.6a) and excitation (figures 3.6b-d) spectra were extracted from the PLE maps for neat SWNTs and mixtures of SWNTs with DOB-719 (figure 3.5). The PL emission spectra (figure 3.6a) were extracted at λ_{EX} = 735 nm, referring to the excitation maximum for the complexation of DOB-719 with the SWNT. The excitation spectra (figures 3.6b-d) for mixtures of DOB-719 and the SWNT were extracted at various λ_{EM}, corresponding to PL peaks for (6,5), (7,5), and (8,4) chiralities for neat SWNTs' dispersions and different concentrations of the dye in the mixtures (table 3.3). The PL spectra in figure 3.6a showed different effects of DOB-719 concentrations on SWNTs of each chirality, indicating selectivity in PL sensing of SWNTs of different

diameters. The peaks corresponding to (6,5) chirality display the maximum RET for the SWNTs' mixture containing the dye at concentration of 0.0005 mg/ mL, whereas RET for (7,5) and (8,4) chirality peaks has maximum at 0.001 mg/ mL.

Comparing the PL intensities at λ_{EX} = 735 nm (figures 3.6 b-d) for both neat SWNTs and mixtures of SWNTs with DOB-719 having new RET peak, I have estimated the sensitivity parameter: PL intensity enhancement. For example, the PL intensities for (6,5) and (7,5) chiralities in the mixtures have grown approximately five times, compared to PL intensity for the neat SWNT, due to raising the concentration of the dye in the SWNT mixtures up to 0.001 mg/mL. However, the PL intensity for (8,4) chirality has increased approximately 2.5 times only. This indicates that the RET from the dye attached to the (6,5) and (7,5) chiralities is more efficient, compared to the RET for (8,4) chirality.

The presence of DOB-719 at the SWNTs' mixture resulted in quenching the PL peaks of the intrinsic E_{11} SWNT emission for all SWNT chiralities (figures 3.6 b-d, for (6,5) at λ_{EX} = 570 nm, for (7,5) λ_{EX} = 650 nm, and for (8,4) at λ_{EX} = 590 nm) and formation of new redshifted PL emission peaks (E_{11}^*) related to SWNTs interacted with dye (figures 3.6 b-d, for (6,5) at λ_{EX} = 580 nm, for (7,5) λ_{EX} = 670 nm, and for (8,4) at λ_{EX} = 605 nm). The admixture of dye at the lowest concentration (0.00025 mg/mL) has severely quenched the PL peaks of the intrinsic SWNT emission and allowed development of the redshifted PL peaks with an average decrease of 85% in PL intensity for all SWNT chiralities, compared to intrinsic PL intensity of the SWNT. However, at the higher concentration of the dye in the mixtures (0.001 mg/mL), the redshifted PL peaks (E_{11}^*) grow, showing efficient formation of the dye-SWNT complexes. The quenching mechanism of the intrinsic SWNT PL peaks and growth of new PL peaks are consistent with the discussion related to the decrease of the E_{11}, and the rise in E_{11}^* absorption peaks evidenced (8,4) SWNTs in figure 3.4 b. Generally, increasing the DOB-719 concentration in the mixtures hinders the intrinsic PL emission for all SWNT chiralities, and improves PL emission from peaks related to SWNTs interacted with dye.

However, in the complexation system of astraphloxin-SWNT, intrinsic PL peaks of the SWNT were practically unchanged [138]. The quenching of intrinsic SWNT emission evidences direct interaction of DOB-719 and the SWNT, which, in the case of the astraphloxin-SWNTs complex, is confined only by the presence of anionic surfactant. Seemingly, SDBS does not affect the interaction of DOB-719 and the SWNT.

The effect of the SDBS surfactant concentrations was studied by measuring the absorption of the mixtures of SWNTs and DOB-719 with SDBS concentration above CMC (0.4 mg/mL) and below CMC (0.065 mg/mL), where CMC of SDBS was reported at 0.15 mg/mL [183]. Absorption spectra were measured for the mixtures of DOB-719 and the SWNT dispersed with SDBS at both premicellar (figure 3.7, curve 3) and micellar (figure 3.7, curve 4)

concentrations. The mixtures with the micellar concentration of SDBS showed no absorption peak at 742 nm corresponding to the dye complexes with the SWNT. Thus, there are no RET from the dye to the SWNT, when micelles of surfactant are entirely covering the nanotubes preventing attachment of the dye. Additionally, the absorption spectrum for the mixture of DOB-719 and SDBS at premicellar concentration was measured (figure 3.7, curve 3), showing superposition of two materials only, with no evidence of interaction between the surfactant and the dye in the absence of nanotubes. Referring to the previous experimental work on the interaction of SDBS and astraphloxin, resulting in aggregation of the dye [138, 184], no such behaviour was observed in the case of DOB-719. This finding shows another dissimilarity of the studied system in comparison with the SWNT-SDBS-astraphloxin, where the RET was the same efficient at the micellar concentrations of SDBS [184].
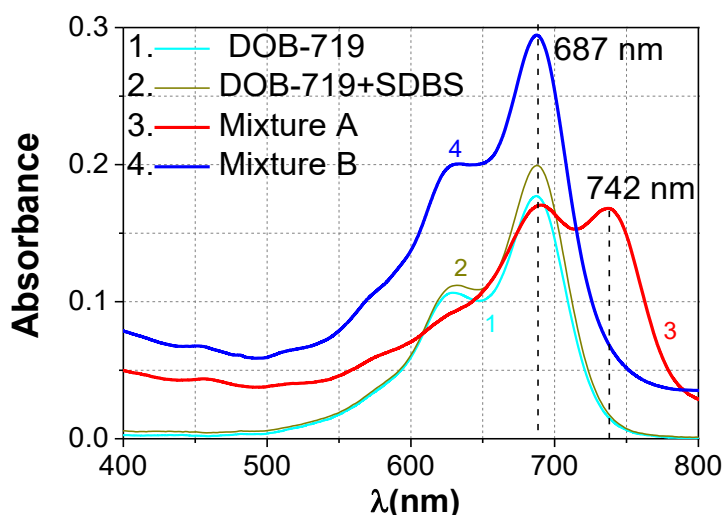
Figure 3.7   *Absorption spectra for as prepared DOB-719 solution (1), as prepared DOB-719 and SDBS solution at premicellar concentration (2), Mixture A is as prepared DOB-719 and SWNT with SDBS at premicellar concentration (0.065 mg/mL) (3), and Mixture B is as prepared DOB-719 and SWNT with SDBS at micellar concentration (0.4 mg/mL) (4). The concentration of DOB-719 is 0.001 mg/mL.*

The energy diagram shown in figure 3.8a represents a two-component system, consisting of the anionic surfactant and the SWNT in water, where the anionic surfactant forms micelles around the nanotubes, having typical exciton energy levels of PL excitation at E_{22} and emission at E_{11}. In figure 3.8b , the three-component system is modelled, where DOB-719 is attached to the SWNT surface via π-π stacking by hydrophobic part (π-conjugated frame) facing the aqueous medium by hydrophilic part (SO_3^- and COO^-). The non-covalent attachment of the DOB-719 to SWNT and anionic surfactant (SDBS) results in the efficient RET at approx. 50 nm redshifted dye excitation wavelength and strong redshift of the E_{11} levels (to E^*_{11}) in the NIR range. The excitation energy of DOB-719 in this range (E_{Dye}) is

transferred to the SWNT levels (E^*_{11}) via the RET. This way, DOB-719 (donor) and SWNT (acceptor) form nanostructure complexes via non-covalent interaction. Therefore, the diagrams represent a model for the emergence of new PL peaks due to the formation of non-covalent complexes of DOB-719 with the SWNT.
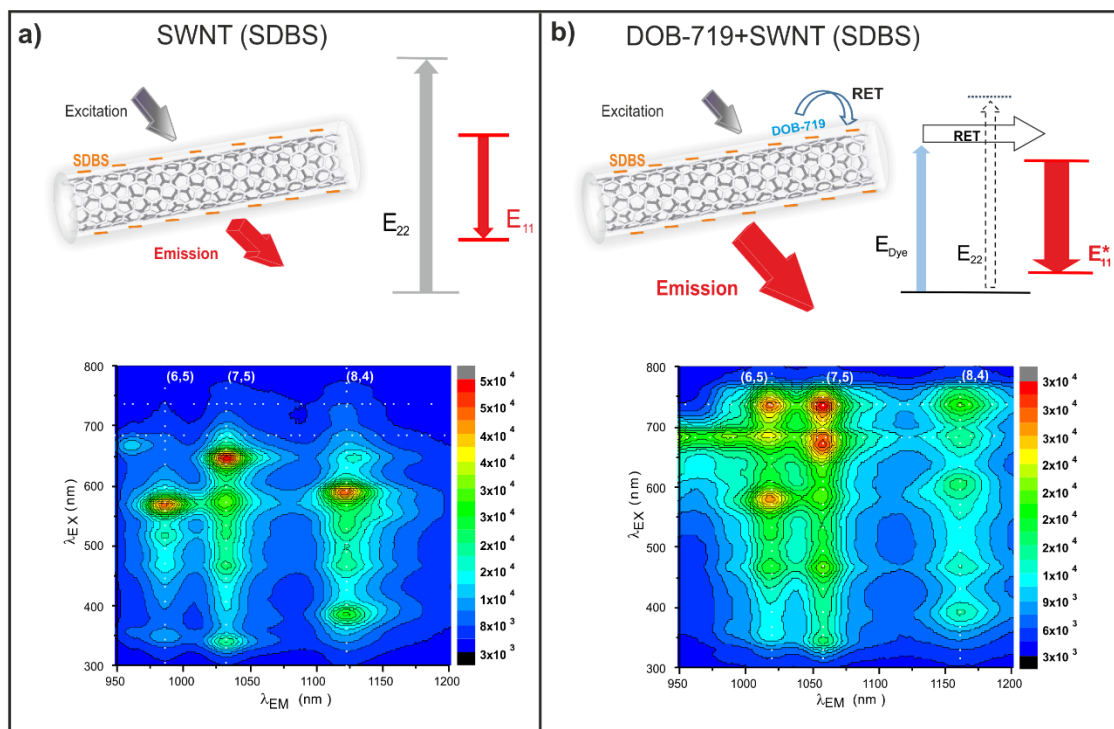
Figure 3.8   Schematic representation of energy transfer in the studied complexes. (a) Dispersions of the neat SWNT and (b) as prepared mixture of DOB-719 with the SWNT in water. In (a) the micelle is formed around SWNT by anionic surfactants (SDBS) and SWNT has characteristic exciton energy levels of PL excitation at E_{22} and emission at E_{11}. In (b) DOB-719 attaches to the SWNT surface via π-π stacking by hydrophobic part (π-conjugated frame) facing the aqueous medium by hydrophilic part (SO_3– and COO–). A non-covalent DOB-719 – SWNT complex emerges with enhanced PL emission from SWNT levels. A visible range excitation of the dye molecules attached to the tubes transfers to SWNT PL levels (E_{11}) emitting in NIR range.

Figure 3.9 shows PL increment at λ_{EX} = 735 nm for (7,5) chirality when varying the SWNTs' concentration and maintaining the dye concentration at 0.001 mg/mL in the mixture of dye with SWNT. This finding supports that the complexes of such dyes have high potential to be used as efficient PL probe for detection of carbon nanotubes, considering that there is an explicit sensing dependence of the RET response on SWNT concentration.

$\lambda_{EX}=735$ nm
chirality (7,5)
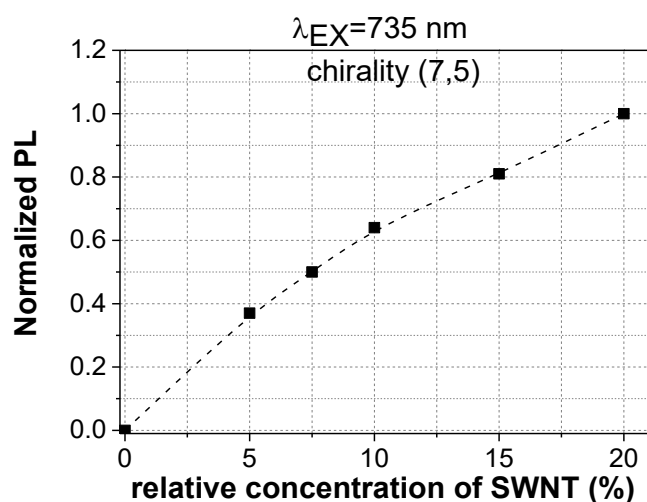
Figure 3.9   SWNT concentration dependence for normalized intensity of the PL at λ_{EX} = 735 nm and λ_{EM} = 1057 nm corresponding to (7,5) chirality emission. 100% of the relative concentration of SWNT corresponds to the initial dispersion of the SWNT (0.0006 mg/mL), where the dilutions were used to prepare the mixtures of DOB-719 with lower concentrations of SWNT. The concentration of DOB-719 is 0.001 mg/mL in all the samples.

The SWNTs' concentration was estimated using the Beer-Lambert law discussed in chapter 2 Equation 2.5. The absorption coefficient for CoMoCAT SWNTs at 652 nm was previously reported to be 11.25 mL/mg.cm [185] Therefore, I estimated the concentration of SWNT in the studied dispersion from the absorption spectrum of SWNTs in figure 3.4 curve 1 as 0.006 mg/mL.

3.3.2   Effect of DOB-719 ageing and visible range PL emission analysis

As discussed in the previous section, the admixture of the dye at the concentration of 0.001 mg/mL to the SWNT dispersed with SDBS has resulted in several new spectroscopic features comparing to the data of the neat SWNT and the neat dye. According to Shandura *et al*., DOB-719 hydrolysis in water, and the ageing of the dye solution result in decreases in the monomeric and dimeric bands and development of a new band at the lower spectral range [177]. Therefore, the effect of dye ageing was studied at the concentration of 0.001 mg/mL using as prepared and aged (measured 24 hours after the mixing) solutions of neat DOB-719 and mixtures of DOB-719 with the SWNT in water.

The absorption spectra of neat DOB-719 in water is shown in figure 3.10. The absorption intensity of the dye decreases in the range of first electronic transition (600-720 nm) and increases in the range below 600 nm. Particularly, new bands start to develop in the ranges of 335-460 nm and 500-600 nm. The decrease of the intensity for the dye monomer and growth of new bands can be related to the degradation of dioxaborine dye, particularly

hydrolysis of the dioxaborine cycle, where the basic mechanism of the hydrolysis is the removal of BF_2 group [174].
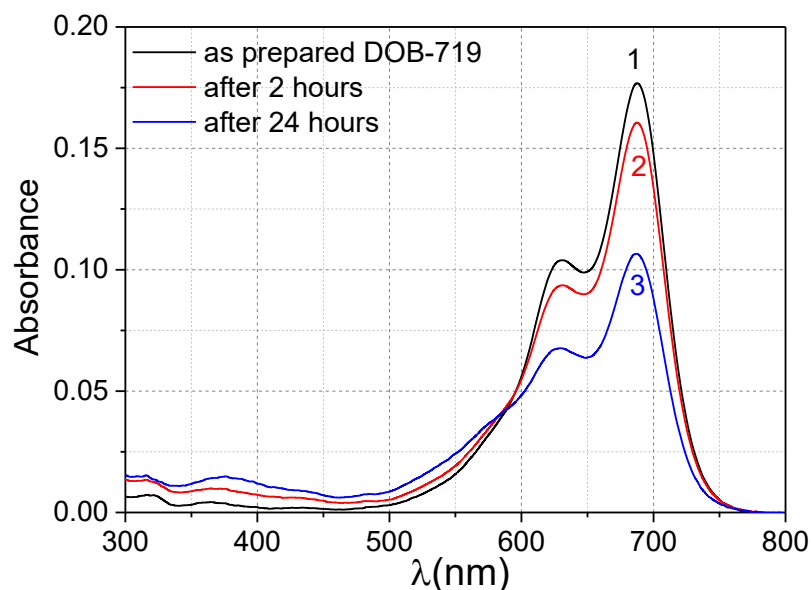
Figure 3.10   Absorption spectra for aqueous solutions of neat DOB-719 as prepared (1), after 2 hours (2) and after 24 hours (refers to the aged samples) (3). The concentration of DOB-719 is 0.001 mg/mL.

To understand the ageing changes in the mixtures, the PLE maps at the visible range (emission range of the dye) were studied for the as prepared and aged mixtures. PLE maps are recorded in the range of intrinsic dye emission for both the as prepared and the aged samples of i) solutions of neat DOB-719 (figures 3.11a,b) and ii) the mixtures of DOB-719 with the SWNT (figures 3.11c,d). The PL peak with λ_{EX} = 685 nm and λ_{EM} = 720 nm (figure 3.11) is related to the monomeric peak in the absorption spectra at 687 nm (figure 3.3a and figure 3.4b). The second band with weak PL in the range of λ_{EX} = 615-640 nm and λ_{EM} = 700-725 nm (in figures 3.11a,c,d) could be related to both the dimeric PL of DOB-719 (λ_{abs} = 600 nm) and/or second vibrational transition of the monomers (λ_{abs} = 629 nm), as discussed for the Gaussian deconvolution of the spectra in figure 3.3b. In figure 3.11b, the PL intensity of the monomeric peak (with λ_{EX} = 685 nm and λ_{EM} = 720 nm) for aged DOB-719 solution is quenched (approx. twice) and a new band with strong PL (the PL intensity is about four times higher than that of the as prepared sample) appears, having maximum at λ_{EX} = 575 nm and λ_{EM} = 680 nm. In this spectral range, the as prepared dye has only a weak and featureless shoulder (figure 3.11a). The above new band (λ_{EX} = 575 nm and λ_{EM} = 680 nm) and low PL intensity band in the range of λ_{EX} = 400-450 nm and λ_{EM} = 660-700 nm (figure 3.11b) match the new bands of absorption developed with time at λ= 335-

600 nm (figure 3.10, curves 2,3). The new features in the aged samples can be justified by the product of the dioxaborine cycle hydrolysis [174].
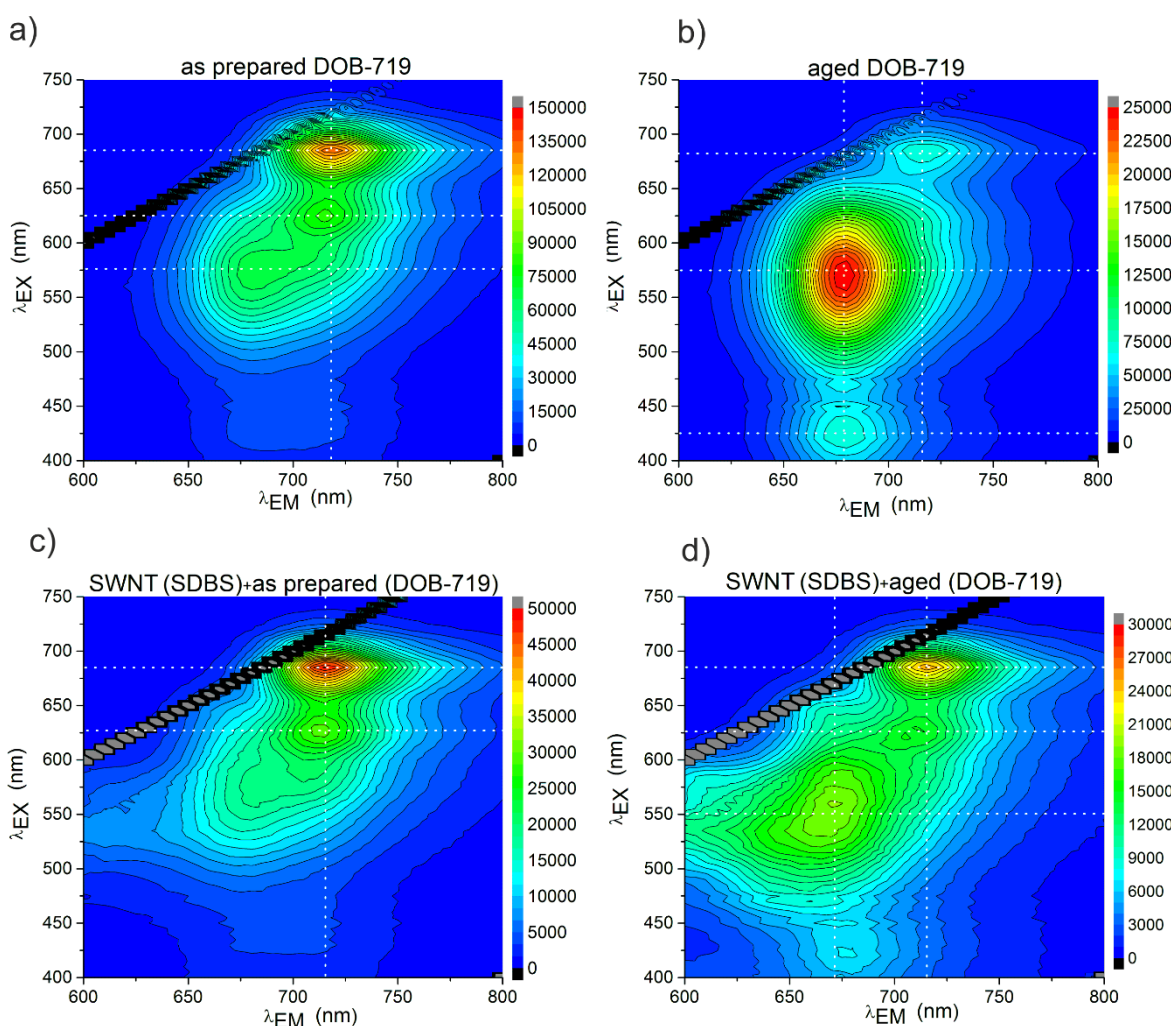
Figure 3.11   PLE maps of aqueous solutions for (a) the as prepared and (b) aged neat DOB-719 as well as (c) the as prepared and (d) aged mixtures of DOB-719 with the SWNT in water. High PL intensities are coded in red colour, whereas low intensities are coded in blue colour. The concentration of DOB-719 is 0.001mg/mL.

The PLE maps in the dye emission range for the mixtures of DOB-719 with the SWNT show that the PL intensity of the monomeric peak (at λ_{EX} = 685 nm and λ_{EM} = 720 nm) is quenched about three times, due to the presence of DOB-719 with the SWNT for both the as prepared (figures 3.11a,c) and the aged (figures 3.11b,d) mixtures. Moreover, the quenching effect on the monomeric peak due to the ageing is practically the same (about twice) for the neat dye solution (figures 3.11a, b) and for the mixtures with the SWNT (figures 3.11c,d). Importantly, in the mixtures with the SWNT, the PL intensity of the band at λ_{EX} = 575 nm and λ_{EM} = 680 nm (due to hydrolysis of dioxaborine cycle) practically does not change because of the ageing of the mixture (figures 3.11c, d). As has been discussed before, in

the neat dye the same band grew up about four times due to the ageing process (figures 3.11a, b). Thus, this result indicates that the molecules of DOB-719 associated with the SWNT are more stable towards the hydrolysis, whereas the free dye molecules (monomers) degrade severely.

Additionally, analysis of visible range PLE maps in figure 3.11 revealed that the mechanism of PL quenching for DOB-719 emission in the mixtures with SWNT is similar to the astraphloxin system [138], as the quenching of both dyes in the mixtures is approximately the same (several times of magnitude). Particularly, comparing DOB-719 and astraphloxin systems (SWNT-surfactant-dye) with SWNT-porphyrin system (SWNT- dye) without the presence of the surfactant, the latter displayed much stronger quenching (ca. 1000 times) [180]. Thus, in the complexes of the SWNT-SDBS-DOB-719, the molecules of surfactant (SDBS) could remain between the dye and the nanotube. However, the direct contact of the dye with the surface of SWNT is also possible. In fact, the distance between the DOB-719 and the SWNT has to be much smaller (or overlap of their π-conjugated systems is stronger) than between the SWNT and astraphloxin system [138]. This is supported by the strong redshift of the E_{11} (22-40 meV), compared to 6 meV reported by [138]), evident quenching of the intrinsic PL emission of the nanotubes, and no interaction between the dye with SDBS in the complexes of SWNT-SDBS-DOB-719, compared to the SWNT-SDBS-astraphloxin system [138, 184].

3.3.3   Effect of surfactant type on the RET

The next logical step is to consider various SWNT dispersions with common surfactants and to compare their PL spectra in the range of λ_{EX} = 735 nm, where the RET is at its maximum for SWNT-SDBS systems. In this section, SWNT dispersions were studied with a range of surfactants such as anionic STDOC and SDOC, cationic CTABr and CPCL, as well as neutral PVP. The choice of these surfactants is motivated by their efficiency in SWNTs' dispersion [72].

3.3.3.1   Anionic surfactants:

The bile salts molecules, such as STDOC and SDOC, are more planar and rigid than linear surfactants like SDS and SDBS. This is why they adsorb on the surface of nanotubes more readily, compared to linear chain surfactants [186]. Moreover, stable and homogeneous micelle structures were reported around the nanotubes, using STDOC and DOC [72].

Figure 3.12 shows a comparison of the absorption spectra of a neat solution of DOB-719 (curve 1), mixtures DOB-719 and dispersions of SWNTs with STDOC (curve 2), and SDOC (curve 3). The presence of the dye in the mixture of SWNTs dispersed with STDOC (curve

2) or SDOC (curve 3) has practically similar absorption features, as discussed previously in figure 3.4a (curves 3-5). Additionally, the two-component system made of STDOC or SDOC and the dye (figure 3.12b, curves 4,5) displayed the same behaviours as the dye and SDBS solution, as discussed previously in figure 3.7, curve 2.

a)

b)
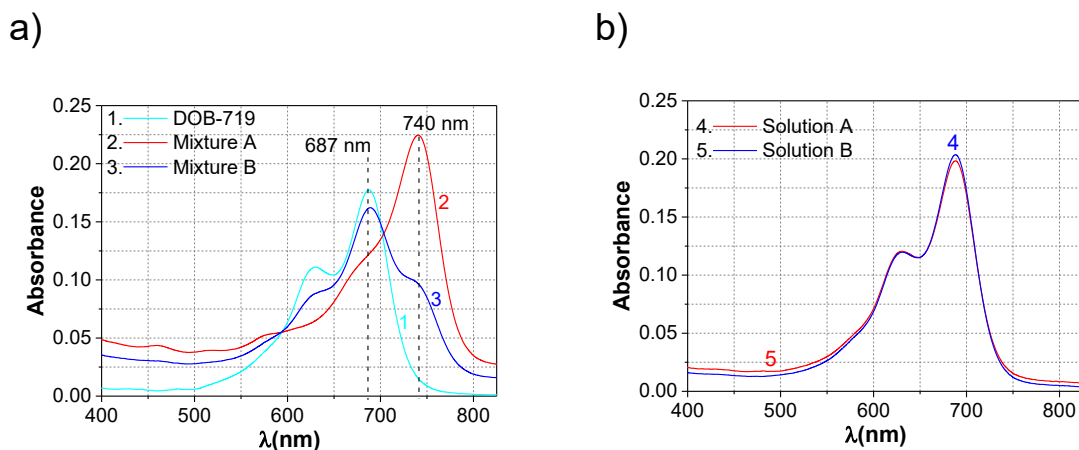
Figure 3.12   a) Absorption spectra for solution of as prepared DOB-719 (1), and mixtures of as prepared DOB-719 with SWNTs dispersed with (2) STDOC (Mixture A), (3) SDOC (Mixture B), and b) Solutions of as prepared DOB-719 with (4) STDOC Solution (A), SDOC Solution (B). Concentrations of STDOC and SDOC in all mixtures are below CMC i.e. STDOC=0.026 mg/mL and SDOC= 0.33 mg/mL. The concentration of DOB-719 is 0.001mg/mL.

The absorption spectrum for the mixture of DOB-719 and SWNT dispersed with STDOC displayed complexation of the dye with the SWNT at absorption peak λ= 740 nm and absorption band at the range of dye monomer (figure 3.12a, curve 2). Whereas, the mixture of the dye and SWNTs dispersed with SDOC (figure 3.12a. curve 3) has the signature of the dye monomers at absorption wavelength 689 nm and exhibits a shoulder at the absorption wavelengths, corresponding to complexation of the dye with the SWNT. The absence of the dye monomeric peak for the mixtures of SWNTs dispersed with STDOC indicates that all dye monomers are complexed with the nanotubes. Furthermore, the presence of the dye monomeric peak for DOB-719-SDOC-SWNTs system indicates that only part of the dye monomers are complexed with the nanotubes. Additionally, the absorption spectrum for the mixture of DOB-719 and STDOC (curve 4) and SDOC (curve 5) at premicellar concentration resulted in superposition of two materials only with no evidence of interaction between the surfactants and the dye in the absence of nanotubes. Figure 3.13 presents PLE maps for SWNTs dispersed with STDOC (figure 3.13a) and SDOC (figure 3.13b) in comparison with mixtures of DOB-719 and SWNTs dispersed with STDOC (figure 3.13c) and SDOC (figure 3.13d), respectively. Figures 3.13 c-d feature similar PLE peaks, as discussed previously in figures 3.5 b-c (DOB-719-SDBS-SWNTs complexes in the range of λ_{EX} = 650–770 nm), due to the RET from the dye to SWNT levels.

Moreover, the mixture of the dye and SWNTs dispersed with SDOC exhibited a high emission at the dye monomeric peak (λ_{EX} = 685 nm). This indicates that the mixture of DOB-719 and SWNTs dispersed with SDOC contains a higher amount of free dye molecules (monomers), compared to mixtures of DOB-719 and SWNTs dispersion with STDOC or SDBS.
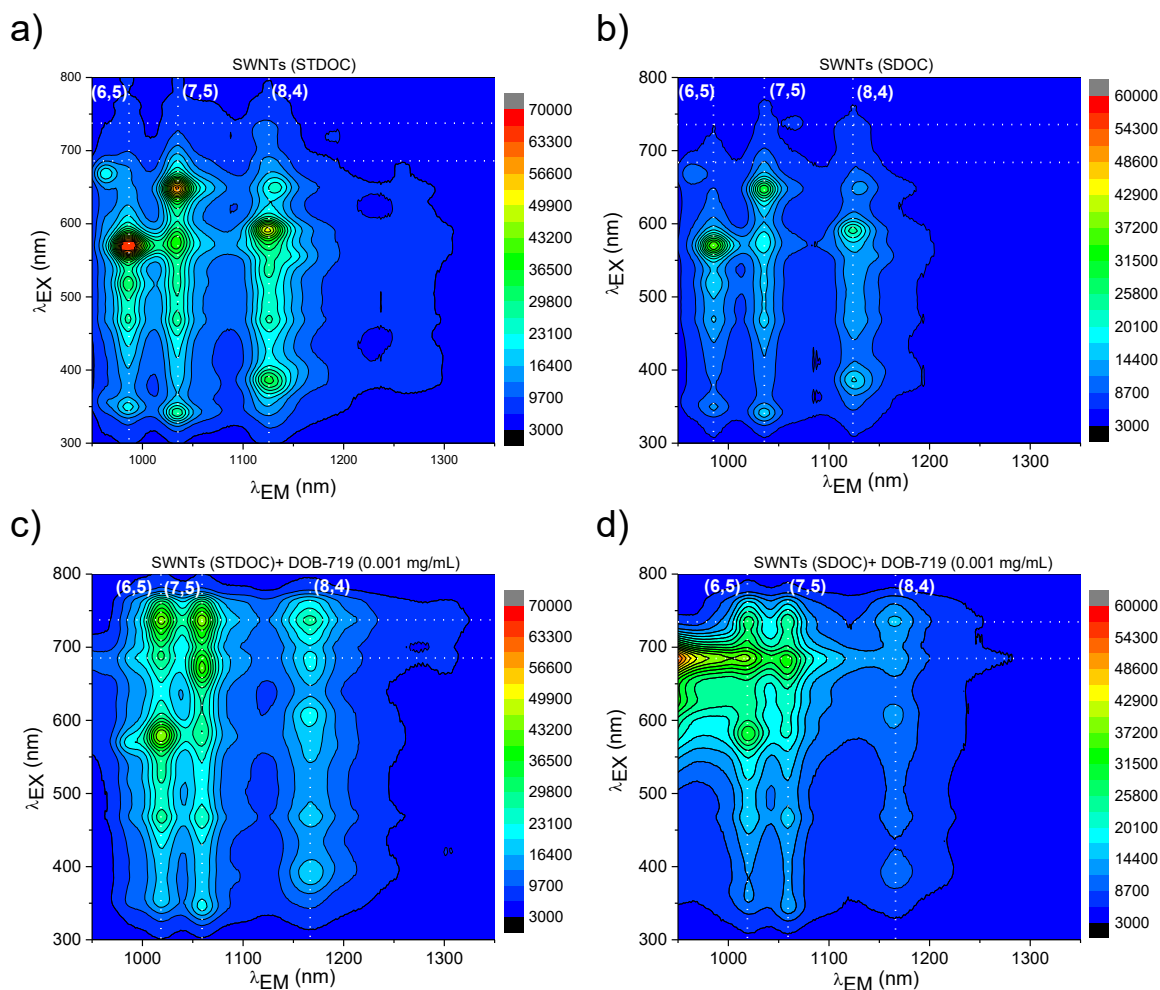
Figure 3.13   PLE maps for mixtures of SWNTs dispersion with STDOC (a), SDOC (b) and mixtures of DOB-719 and SWNTs dispersed with STDOC (c) and SDOC (d). DOB-719 concentrations in mixtures (c-d) is 0.001 mg/mL.

For aqueous dispersions of SWNTs, the surfactant molecular structure plays an important role. Bile salts (STDOC and SDOC in this study) are adsorbed easily on hydrophobic nanotube surfaces [187, 188]. Their hydrophobic part covers a larger contact area with SWNTs [189], compared to linear chain surfactant (SDBS) [190, 191]. Considering this approach, the packing density of STDOC and SDOC on the nanotube surface is smaller, compared to SDBS. In SDOC, the shorter chain connecting the polar group to the π-electronic system of surfactant could allow a lesser amount of dye molecules to complex

with SWNTs covered by SDOC. Whereas, the elongated tauro-chain of STDOC provides good interaction of the dye with SWNTs and efficient RET.

The histogram in figure 3.14 summarizes the PL enhancement resulting from the admixture of DOB-719 to SWNT dispersed with the studied anionic surfactants. The data are obtained by extracting the PL emission at λ_{EX} =735 nm (referring to the complexation of DOB-719 with the SWNT) at dye concentration 0.001 mg/mL in the mixture. For neat SWNTs' dispersions, PL emission spectra were extracted from figure 3.5a, figure 3.13a and figure 3.13b to obtain PL emission spectra for SWNTs dispersed with SDBS, STDOC and SDOC, respectively. Whereas, data for mixtures of DOB-719 and SWNTs dispersed with SDBS, STDOC and SDOC were extracted from (figure 3.5d), (figure 3.13c) and (figure 3.13d), respectively. The PL enhancement factor was calculated by dividing the intensity of PL peaks at λ_{EX} = 735 nm for neat SWNTs' dispersions and mixtures of DOB-719 with SWNTs for each surfactant. The PL enhancement factor is practically the same for all the studied anionic surfactants. The maximum was observed for (6,5) tubes, indicating a similar enhancement effect for the studied anionic surfactants.
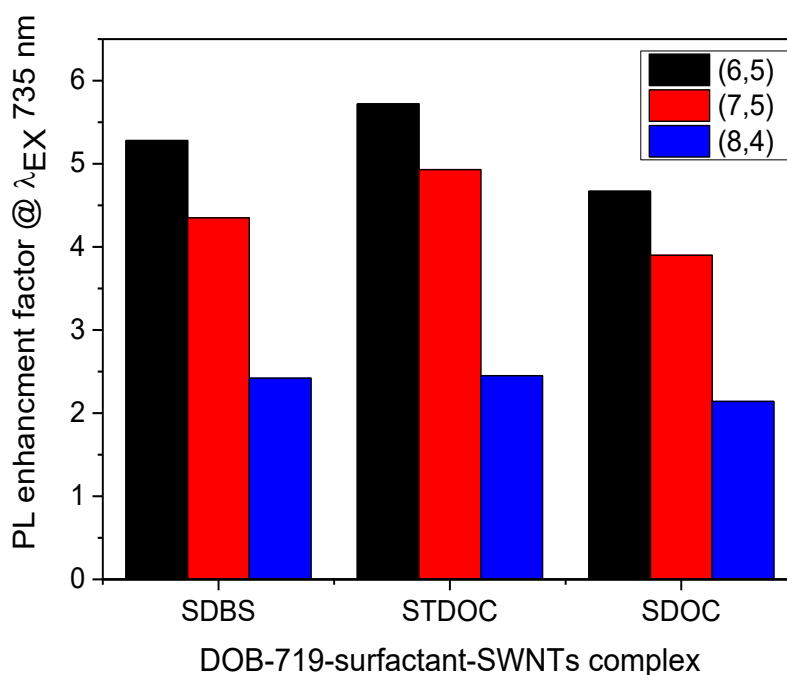
Figure 3.14   Histogram of the PL enhancement for mixtures of DOB-719 and SWNTs at λ_{EX} = 735 nm. SWNTs are dispersed with SDBS, STDOC and SDOC. The DOB-719 concentration is 0.001 mg/mL.

3.3.3.2   Neutral surfactants:

PVP has been reported as an efficient polymer to disperse [60, 192] or stabilize [15] the nanotubes in aqueous media. PVP polymer features a hydrophobic alkyl backbone, and hydrophilic pendant groups, which can wrap the SWNTs' surface, where the polymer backbone is in contact with the nanotube and pyrrolidone groups are facing the water [15, 60] . However, PVP is far less efficient in dispersing the nanotubes in water, compared to anionic surfactants [72]. Moreover, it wraps SWNTs in bundles with different sizes and compositions and the PL yield from the nanotubes wrapped with PVP is 30 times lower, compared to nanotubes dispersed with SDBS [193]. Therefore, a higher amount of PVP in the initial SWNTs mixture (table 3.1) is used to obtain a reasonable PL signal.

Figure 3.15 shows the absorption spectra for the mixture of DOB-719 with the SWNT dispersed with PVP, in comparison with its components. The absorption of SWNT dispersion displayed an increased absorption background in the range of 400-800 nm (figure 3.15, curve 2). The absorption peak for the dye and PVP in the absence of nanotubes (figure 3.14, curve 3) is 11 nm redshifted, comparing to neat DOB-719 peak. Furthermore, the presence of SWNTs in the mixture (figure 3.15, curve 4) resulted in 38 nm redshift, due to the complexation of the dye with the nanotubes.
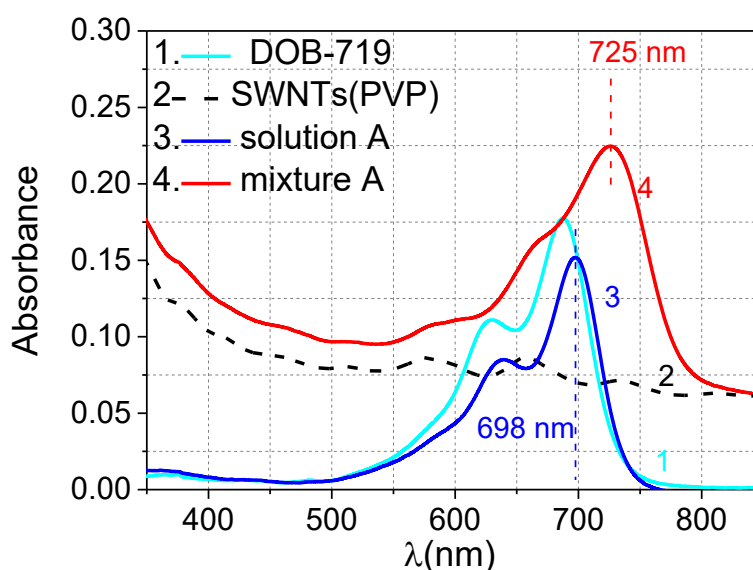
Figure 3.15   Absorption spectra in the visible range for the solution of neat DOB-719 (1), SWNTs dispersed with PVP (2), solution A: solution of dye and PVP (3) and mixture A: a mixture of DOB-719 and SWNTs dispersed with PVP. The concentration of PVP in (2) and (3) is described in table 3.1 and 0.5 mg/mL in (4). The concentration of DOB-719 in (1), (2) and (4) is 0.001 mg/mL.

Additionally, the PLE maps for dispersions of SWNTs with PVP (figure 3.16a) and the mixture of the dye and SWNTs with PVP (figure 3.16b) were analyzed. The low PL intensity of the nanotubes in NIR range (figure 3.16a) indicates a low concentration of individual s-SWNTs and/or the presence of increased m-SWMTs in the wrapped nanotubes bundles. Comparing figure 3.15, curve 2 with figure 3.16a, the increased absorption background for SWNTs' dispersion can be explained by the presence of impurities and/or nanotube bundles, due to the wrapping nature of the polymer during the ultrasonication and ultracentrifugation process (The purity of SWNT powder used in this study was described in section 3.2).

a)   b)
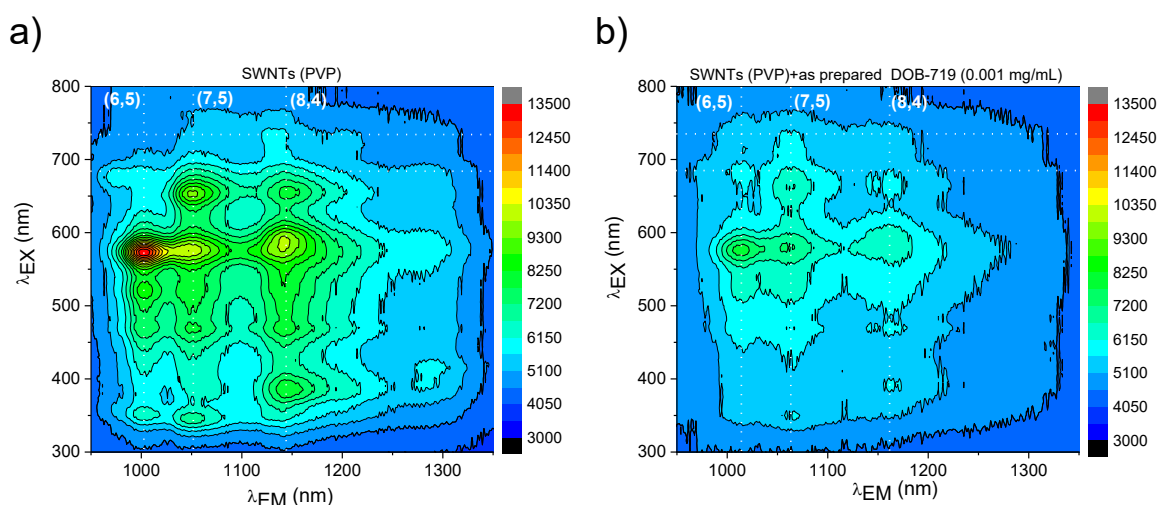
Figure 3.16   PLE maps for SWNTs dispersion with PVP (a) and mixture of DOB-719 and SWNTs dispersed with PVP (b). The concentration of PVP in (2) and (3) is described in table 3.1 and 0.5 mg/mL in (b). Concentrations of DOB-719 in (b) is 0.001 mg/mL.

To have a better understanding on the nature of the interaction, the PL emission spectra from figures 3.16a and b at λ_{EX} = 735 nm were extracted.

Figure 3.17 represents the PL spectra for the SWNT dispersed with PVP (figure 3.17, curve 1) and the mixture of the DOB-719 and SWNT with PVP (figure 3.17, curve 2). The mixture of the DOB-719 and SWNT with PVP exhibited very weak RET from the dye to the SWNT for (6,5) and (7,5) PL peaks. Furthermore, these PL peaks were redshifted, due to the presence of the dye in the mixture.
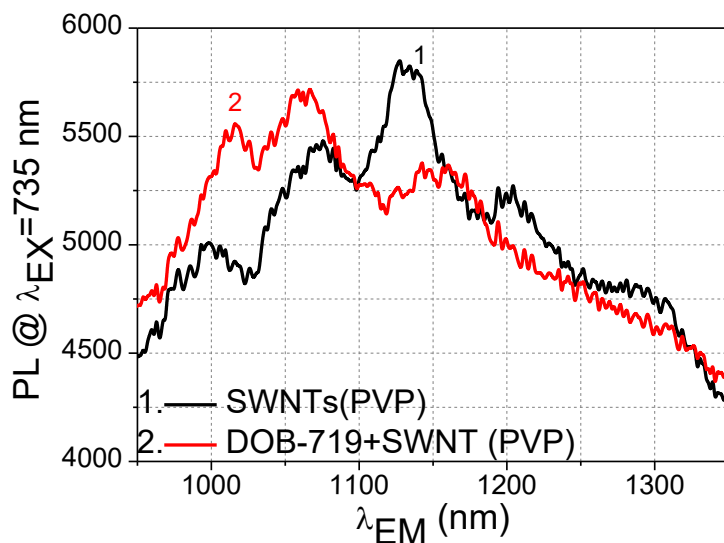
Figure 3.17   PL spectra at λ_{EX} = 735 nm for mixture of neat SWNTs dispersed with PVP (1) and mixture of DOB-719 and SWNT dispersed with PVP (2). The concentration of DOB-719 is 0.001 mg/mL.

Previous studies reported that PVP can bind exceptionally well various substances, such as drugs, toxins, and dyes, etc. [194]. Therefore, the redshift PL and the weak RET can be regarded as part of the physical complex (with no π-π stacking) of the SWNT wrapped by PVP polymer with dye molecules.

The absence of benzene rings in the structure of PVP wrapping polymer leads to a lack of efficient π–π stacking between the dye and SWNTs. Therefore, the PL yield of the complexes (figure 3.17, curve 2) is in the range of a very low percentage, compared to SWNTs (figure 3.17, curve 1).

3.3.3.3   *Cationic surfactants:*

Among the cationic surfactants, CTABr and CPCL are reported to yield high tube concentrations [72]. Due to the presence of the pyridinium ring in the CPCL structure, the dispersion containing CPCL has lower nanotube solubilisation, compared to SWNTs' dispersion with CTABr [72].

Figures 3.18a-b present the absorption spectra for the mixture of DOB-719 with the SWNT, in comparison with its components. The two components system containing CTABr or CPCL surfactant and DOB-719 (figures 3.18a and b, curves 3) resulted in merging of the monomeric, dimeric and the second vibrational peaks (discussed previously in figure 3.3) of the dye spectrum and overall broadening the dye absorption bands, compared to neat dye solution (figures 3.18a and b, curves 1). This spectral change takes place probably due to the strong interaction between the cationic surfactant and anionic parts of the dye

(interaction between the cationic surfactant and anionic parts of the DOB-719 (SO_3^- and COO^- groups)) and formation of the dye–surfactant complexes [195].

However, the presence of SWNTs in the mixture of DOB-719 and CPCL resulted in 15 nm redshift for the maximum for DOB-719 (figure 3.18b, curve 2), compared to the neat dye (figure 3.18b, curve 1) and dye-CPCL peaks (figure 3.18b, curve 3). Moreover, the absorption spectra for the neat dye (figure 3.18a, curve 1) and dye-CTABr solutions (figure 3.18a, curve 3) practically do not change due to the presence of the SWNTs (figure 3.18a, curve 2 with a red redshift of 4 nm).

The observed 15 nm redshift could be related to the π-π stacking of the dye to the nanotubes surface, supported by the presence of the pyridinium ring at the head of the CPCL surfactant (figure 3.2).

a)   b)
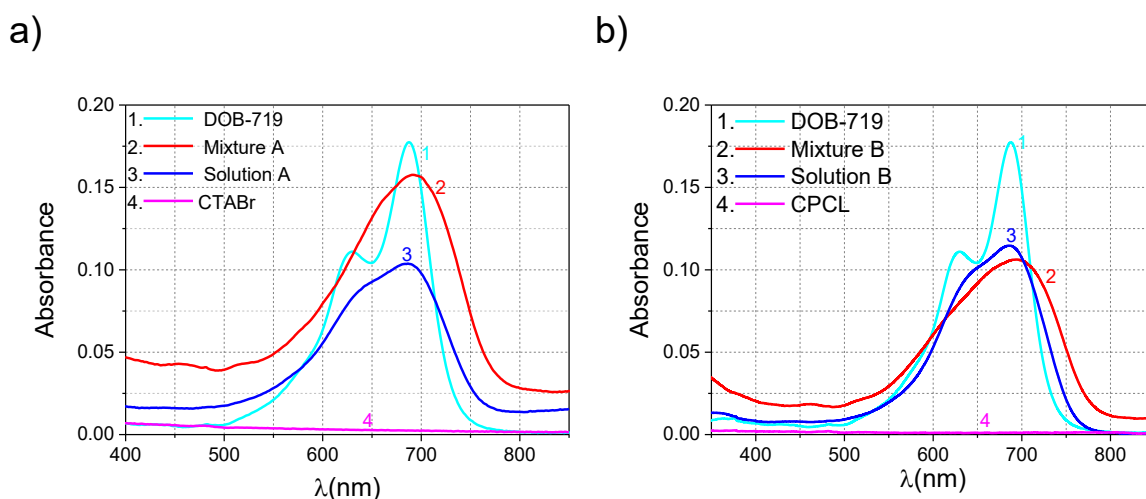
Figure 3.18   Absorption spectra for DOB-719 aqueous solution (curve1 in a & b), a). Mixture A: mixture of DOB-719 and SWNTs dispersed with CTABr (2), Solution A: solution of DOB-719 and CTABr (3), and neat CTABr (4). B) Mixture B: mixture of DOB-719 and SWNTs dispersed with CPCL (2), Solution B: solution of DOB-719 and CPCL (3), and neat CPCL. The concentration of DOB-719 is 0.001 mg/mL.

Dispersions of neat SWNT with CTABr and CPCL cationic surfactants were stable for a few weeks, having practically unchanged PL emission intensity (figure 3.17 a,c). However, the admixture of DOB-719 to the SWNT dispersed by cationic surfactants dramatically speeds up the aggregation of SWNTs from weeks to a couple of hours with a strong effect on the PL emission (figure 3.17). The aggregation most probably takes place due to the compensation of positive charge of the SWNTs-surfactant complex by the negative charge of dye molecules with SO_3- and $COO-$ groups.

The PL emission spectra in figure 3.19e were extracted at λ_{EX} = 735 nm from PLE maps of SWNTs dispersed with CTABr (figure 3.19 a) and mixture of DOB-719 and SWNTs dispersed with CTABr (figure 3.19 b). Similarly, the PL spectra in figure 3.19 f were extracted

at λ_{EX} = 735 nm from PLE maps of SWNTs dispersed with CPCL (figure 3.19 c) and the mixture of DOB-719 and SWNTs dispersed with CPCL (figure 3.19 d). The presence of the DOB-719 in the mixtures of SWNTs dispersed with CTABr resulted in weak RET from the dye to the SWNT. Whereas, no RET was observed when admixing the dye to SWNTs dispersed with CPCL, due to strong aggregation of the nanotubes. For the mixture of DOB-719 and SWNTs dispersed with CTABr, aggregation of the nanotubes was observed within a few days. However, the presence of the dye in SWNTs dispersed with the CPCL mixture resulted in the aggregation of the nanotubes within a couple of hours.
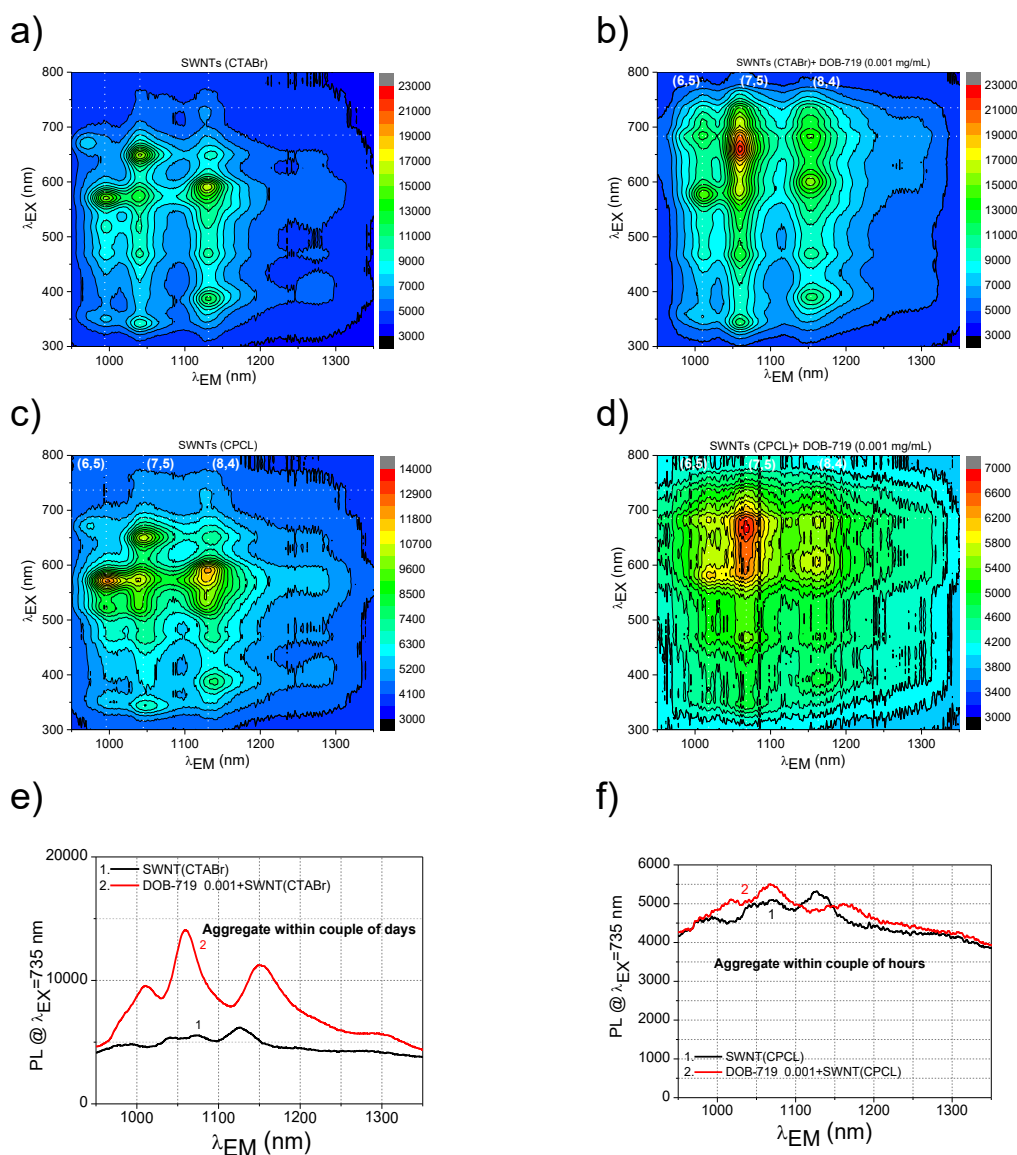
Figure 3.19   PLE maps for a) SWNTs dispersed with CTABr, b) mixture of DOB-719 and SWNT dispersed with CTABr, c) SWNTs dispersed with CPCL and d) mixture of DOB-719 and SWNT dispersed with CPCL. PL spectra at λ_{EX} = 735 nm for e) mixture of SWNTs dispersed with CTABr (1) and mixture of DOB-719 and SWNTs dispersed with CTABr (2). F) mixture of SWNTs dispersed with CPCL (1) and mixture of DOB-719 and SWNT dispersed with CPCL (2). The concentration of DOB-719 is 0.001 mg/mL.

To sum up, comparing the results for all studied surfactants, it can be inferred that Coulombic attraction/repulsion is not affecting much on the RET from DOB-719 to SWNT. It means that π-π stacking of the hydrophobic part of the dye plays the key role in the RET process.

3.4 Chapter conclusion

Indopentamethinedioxaborine dye (DOB-719), having an extended π-conjugated system and absorption in NIR range, resulted in very promising optical properties, due to the formation of non-covalent complexes made of dye-anionic surfactant-SWNTs. The complexes have strongly enhanced the PL intensity from SWNT levels in the NIR range due to RET from the dye and resulted in the new PL bands at excitation wavelength λ_{EX} = 650-780 nm, where the intensity of PL emission of the SWNT is very low. The most efficient RET happens at λ_{EX} = 735 nm. First, the effect of the dye concentration on the energy transfer to the tubes was investigated. The study shows that a mixture of DOB-719 at 0.001 mg/mL with the SWNT dispersed with anionic surfactants in water, allows the formation of a nano-structured complex with strong dielectric screening, and yields the maximum RET from dye to all SWNTs chiralities. However, for lower and higher concentrations of dye, the RET decreased, and was observed only for small diameter nanotubes, such as (6,5) and (7,5) chiralities. Thus, the RET is tubes' chirality and the dye concentration is dependent and can be exploited to selectively sense the SWNT. This finding supports that the complexes of such dyes have high potential to be used as an effective PL probe for detection of carbon nanotubes.

Second, the effect of dye ageing was studied. The spectral properties of neat DOB-719 in water changes within 24 hours, due to hydrolysis of dioxaborine cycle. Whereas, for the mixture of DOB-719 and SWNT, the dye monomeric molecules were complexed with the SWNT micelles and became more stable towards the hydrolysis. The study was then continued by considering various SWNT dispersions, using common surfactants and to compare their PL spectra in the range of λ_{EX} = 735 nm, where the RET is at its maximum for SWNT-SDBS systems. SWNT micelles dispersed with some neutral or cationic surfactants resulted in very weak RET from the dye to the nanotubes at λ_{EX} = 735 nm. It means that molecular structure of the surfactants and pi-stacking of hydrophobic part (π-conjugated frame) of the dye to the nanotubes play the most important part in the RET process. Thus, the interaction between DOB-719 and the SWNT opens a new horizon to design efficient and tailorable optical probes for not only sensitivity but also selectivity of the PL detection towards the nanotube diameters.

Chapter 4: Saturable absorber composite for ultrafast photonics

4.1 Introduction

In this chapter, carbon nanotube SAs have been characterized in terms of their nonlinear optical properties and application in the ultrafast fibre laser. The composites are developed from the water-based dispersion of SWNTs. Fabrication of composites allows them to be integrated into a fibre laser setup and is one of the most generally reported methods for creating SAs from 1d and 2d materials [25, 146, 147, 196-200].

The chapter starts with the introduction of theoretical aspects of nonlinear optical saturable absorption and the relevant influence in the pulsed laser systems. This is followed by systematic characterization of carbon nanotube polyvinyl alcohol (PVA) polymer composite as SA has been carried out.

4.2 Saturable absorbers for mode-locked fibre lasers

Ultrashort pulse lasers having sub-picosecond (ps) pulse duration are of particular interest for various fields, including optical communication, spectroscopy, materials processing, laser surgery and many other applications. Particular attention has been paid to fibre lasers to generate ultrashort pulses, due to their major practical advantages, e.g. higher beam quality, compactness, alignment free and low cost [142, 143]. One of the most widely applied methods to produce a pulsed output from a laser is to employ fast optical switches, such as SAs [26]. SAs are optical elements, which convert the laser continuous wave output into a train of ultrashort optical pulses [26, 201]. They can thus dynamically modulate the gain characteristics of a laser cavity to produce a pulsed output via techniques, such as mode-locking and Q-switching [201]. The first SAs were reported more than five decades ago by H. W. Mocker *et al*. using organic dyes [202]. However, their slow recovery times and poor stability hindered their progress and therefore they were substituted with SESAMs [203]. These devices consist of semiconductor MQW deposited by a molecular beam epitaxy. [26, 204]. However, SESAMs require a complex and costly fabrication process and also need extra free space optics to couple light into the optical fibre.[26]. Several reports indicate that carbon nanotubes [25, 147], and other 2 D materials, such as graphene [205, 206] transition metal dichalcogenides [200] and black phosphorous [199] are promising for future SA technology.

4.2.1 Characteristics of the SA

Generally, a SA device is characterized using four main parameters. They are the recovery time, the modulation depth, the non-saturable absorption and the saturation intensity/fluence. The recovery time is the decay time of photon-generated carriers after the absorber being excited by a high optical intensity [26, 154, 207, 208].

For ultrashort pulse generation, the recovery time should be much less than the pulse duration (a few picoseconds or less is required). This is dependent on the carrier dynamics of the SA material, and usually defined using a pump-probe measurement [209, 210], where a "probing" laser pulse is applied to record the absorbance at set time intervals after a higher intensity "pumping" pulse. The recovery time influences both the maximum output frequency and the minimum pulse duration [26, 154, 207, 208]. If the round-trip time for the pulse within the cavity is less than the recovery time, instability can arise as the SA will not have returned to its unsaturated state before the subsequent pulse arrives [26, 208]. Meanwhile, the pulse profile is shaped by the response time of the SA, due to the dynamics of gain and loss modulation in the cavity [26, 208, 211].

The modulation depth (α_0) is usually defined as the maximum possible change of saturable absorption ($\Delta\alpha$) over the linear absorption of the absorber (α_{lin}). Additionally, the larger α_0 can allow a shorter pulse duration but can also result in pulse train instability [26, 203, 212]. Non-saturable absorption (α_{ns}) is the part of the absorber loss that is present even if the SA device is fully saturated (typically unwanted), which cannot be saturated at the relatively high intensity. Therefore, the α_{ns} should be maintained at the minimum because a large α_{ns} will reduce the modulation depth of the SA device since the linear absorption α_{lin} is defined by the total of $\Delta\alpha$ and α_{ns}. The saturation intensity (I_{sat}) is defined to be the optical intensity (power per unit area) it takes to reduce the absorption of the SA by half its saturable absorption. It is related to the saturation fluence (F_{sat}) by the recovery time of the absorber.

$$F_{sat} = I_{sat} \times \tau_p$$

Equation (4.1)

Furthermore, the insertion loss is defined as the total loss for the SA device at low intensities (saturable to non-saturable ratio). It is also a useful figure of merit, commonly employed by the community that reveals key features of these devices, and together with the saturation power allows direct comparison with other devices in the literature.

A nonlinear absorption experiment (also called power-dependent transmission experiment) is a measurement where the absorption or transmission of a SA device is registered at different input power levels. In most cases, the instantaneous saturable absorber model expressed in equation 4.2 is implemented to estimate the SA parameters [213].

$$\alpha(I) = \frac{\alpha_o}{1 + I/I_{sat}} + \alpha_{ns}$$
Equation (4.2)

In general, the saturable absorber parameters should be decided in the context of a comprehensive laser design process, which takes into account the limitation of the SA device to high intensities or pulse energies.

The next subsections (4.2.3 and 4.2.4) discuss how the gain modulating characteristics of SAs can be employed to generate pulsed output from a continuous wave laser.

4.2.2 SWNTs' saturable absorbers

The most successful demonstration of SWNT-based SAs reported so far is as mode-lockers for ultrashort pulse lasers and noise suppression filters [25]. The use of SAs as mode-lockers to generate ultrashort pulses require low loss at a higher intensity to support the optical pulse formation from noise in the laser cavity [214].

Figure 4.1 presents the working principle of pulse formation [214]. In the laser cavity, the total gain remains constant while the SA modulates the total loss. At low intensity, the gain is always less than the loss. When the loss becomes smaller than the gain in a very short time window, the net gain becomes positive, resulting in pulse formation with a duration similar to that of the window.
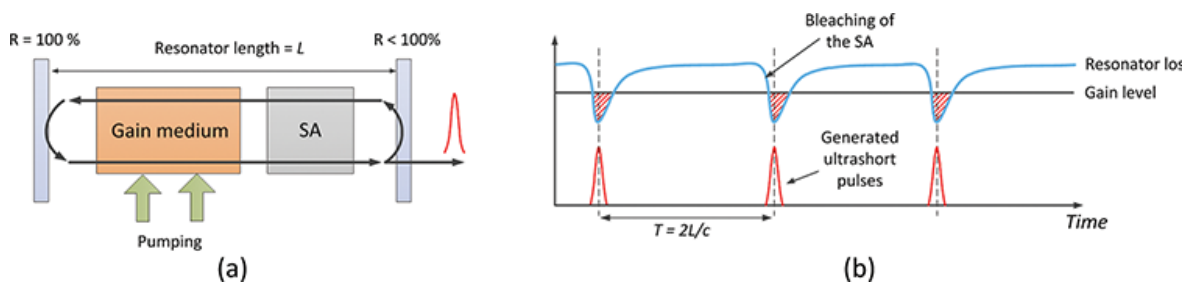
Figure 4.1   Schematic representation for mode-locked laser using saturable absorber. Adapted from [214].

Before the discovery of SWNTs, SESAMs were the main devices used in most commercial SA applications. However, they allow a narrow operating bandwidth and require an

expensive fabrication and packing process. Moreover, their relaxation time is restricted to picosecond range [26].

Another type is the fibre based SAs, such as nonlinear polarization (NPR), nonlinear loop mirror (NOLM), and nonlinear amplifying loop mirror (NALM) [215, 216]. The ultrafast recovery time for NPR and NOLM is in the order of 10 femtoseconds (fs) because they are based on the instantaneous third order nonlinearity in silica glass. In general, fibre based SAs are not ideal, due to higher saturation intensity than SESAMs, and are polarization dependent.

These disadvantages have opened up the race to find other novel materials for SA applications. The field of nanomaterial-based SAs gained the attention of the researchers [25, 146, 147, 196, 200, 214]. Mainly, single-wall carbon nanotube (1D) and graphene (2D) emerged as promising materials allowing several key advantages over existing mode-locking devices, particularly an intrinsic sub-picosecond recovery time, broadband operation, compatibility with fibre, cost efficiency and ease of preparation.

Considering fibre lasers, there is still room for the improvement of the SWNT-SA. This can be achieved by better control of the tube diameter distribution, length and bundling during the fabrication process and utilizing the interaction between the nanomaterials and the evanescent field of the propagating wave during the integration process. Moreover, the insertion losses for SWNT-SAs are typically less than 1 [217]. In contrast, SESAMs have been reported with non-saturable losses as low as 0.1% and insertion losses more than 40 [218]. The high non-saturable loss of SWNT-SAs is the main issue for their application in ultrafast solid-state lasers, but not in fibre lasers, which can tolerate high losses, due to the high single-pass cavity gain of fibres.

Yamashita *et al*. have compared the saturation characteristic of SWNT thin film made by the spray method with atypical SESAM reported by reference [214] at the wavelength of 1.55 µm. They reported that saturation intensities of SWNTs is ~12.5 MW/cm^2 as compared to ~10 MW/cm^2 for typical SESAMs, which is practically equal saturation intensity. Additionally, they showed that the saturation intensity of pristine single layer graphene-based SA device is much higher (~ 250 MW/cm^2), compared to SWNTs and SESAM for the same operation wavelength.

The choice of carbon nanotubes for SA application is usually defined by the available s-SWNTs with an energy band resonantly matching the operation wavelength of the specific fibre laser, i.e. 1.0–1.1 µm (Ytterbium), 1.5–1.6 (Erbium-doped fibre laser), and 1.7–2.1 µm (Thulium-doped fibre laser). For instance, HiPco SWNTs features a broad absorption band at ~1550 nm as shown in figure 4.2 which qualified them for the telecommunication C band (1530–1565 nm) applications [219].
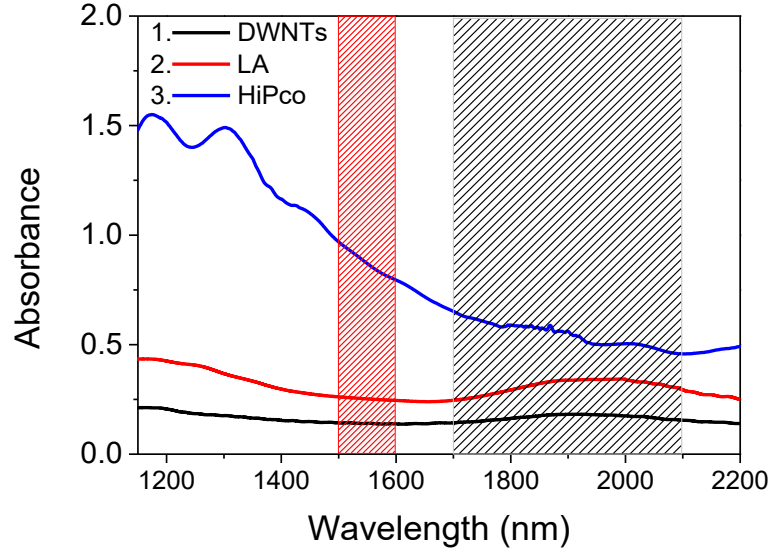
Figure 4.2   Absorption spectra for DWNTs-PVA (1) , LA SWNTs-PVA (2) and HiPco-PVA composite films The grey colour bar indicates the Thulium-doped fibre laser emission window, i.e., 1.7–2.1 µm and the red bar indicates Erbium-doped fibre laser emission window, i.e. 1.5–1.6 µm. PVA background subtracted

The absorption optical density of the nanotubes based SA device at a required wavelength of operation is commonly used as an indicator of the device performance [25]. For example, the HiPco film shown in figure 4.2 displays an optical density of 0.85 at 1550 nm. DWNTs and LA films exhibit a maximum optical density of 0.2 at 1920 nm and 0.3 at 1925 nm, respectively. Importantly, the minimum optical density at the device operation wavelength need not be less than 0.2 for acceptable SA performance.[25].

Recently, we demonstrated that the modulation depth (α_0,=64%) and saturation intensity (I_{sat} =15.62 MW/cm^2) for DWNTs [220] are much higher compared to LA SWNT (α_0,= 40% and I_{sat} =2.25 MW/cm^2) [221] operating around ~ 2 µm. Moreover, we compared the time-resolved spectroscopy of the LA SWNTs with DWNTs [220] and the obtained results show that the relaxation times for DWNT/PVA are twice as fast when compared to LA SWNT-SA. This underlines the promise of DWNTs as a fast SA in high-intensity laser optical cavities, operating close to the 2µm wavelength range.

4.3 SWNTs-PVA composite fabrication and characterization

Various approaches have been suggested in the literature for the integration of SWNTs in the fibre system. These approaches are presented in figure 4.3 and can be classified based on the means of interaction between the nanotubes and the propagating wave into direct and lateral interactions. For example, nanotubes can interact directly with the propagating wave when sandwiched between two fibre connectors using polymer composites (figure 4.3a) or injected into fibre microchannels (figure 4.3b). Otherwise, nanotubes can interact laterally with the evanescence field of the propagating wave when coated on the surfaces of D-shaped figure 4.3c or tapered fibres figure 4.3d.
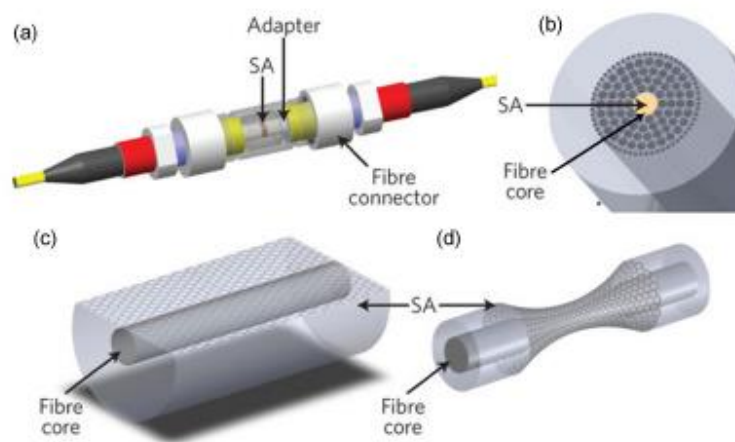
Figure 4.3   Summary of common integration approaches for SWNTs in fibre devices. a, sandwiched device, b, photonic-crystal fibres, c, D-shaped and d, tapered fibres. Adapted from [196].

The polymer composites method is widely used to fabricate a flexible and freestanding SA device, which can be sandwiched between two fibre connectors. Several polymers have been reported in the literature as a host matrix for the nanomaterials used in fibre lasers SA applications, such as polyvinyl acetate (PVAc) [206], polyvinyl alcohol (PVA) [222], polymethylmethacrylate (PMMA) [223], carboxymetylcellulose (CMC) [25], polyaniline (PANi) [182] and polystyrene (PS) [224]…..etc.

Thus far, PVA polymer has been commonly used as a hosting matrix for the nanotubes for SA applications due to its low losses and solubility in water [25]. However, all the reports in the literature have commonly agreed that SWNT-SAs' thin film, sandwiched between two fibre connectors suffer from thermal damage, such that the device is burned out with the optical power of a few tens of mW, which can limit their use in high power lasers [25, 147, 214]. Practically, this type of integration allows single point interaction between the propagated

pulse and SWNTs' film. Therefore, the resultant peak power will be concentrated on an area equal to the fibre mode-field diameter (for single mode fibre (SMF-28) =10.4±0.8 μm), which can burn the SA composite at a high power regime and, therefore, alter its elemental composition. Moreover, SA properties, such as saturable losses and non-saturable losses are expected to change due to contentious high energy pulses radiation in the laser cavity. To date, no systematic study has been reported on the thermal damage of the SWNT composite sandwiched between two fibre connectors.

4.3.1 Experimental procedure

4.3.1.1   Materials

HiPco single-walled carbon nanotubes were purchased from Unidym (Lot # P0261). The purity of SWNT powder is defined in the specification sheet by Unidym; the purified HiPco powder contains at least 85% of SWNT with less than 15% of impurities, such as catalyst particles, amorphous carbon, and multiwall nanotubes. HiPco SWNTs have a tube diameter distribution from 0.8 to 1.3 nm. The choice of HiPco SWNTs is justified by their appreciable optical density at Erbium-doped fibre lasers emission window 1500–1600 nm. This is due to the presence of tube diameters ~1.2 nm, which corresponds to a peak wavelength of about 1560 nm [225-227].

Dispersions of SWNT were prepared in the presence of using SDBS. In this study, polyvinyl alcohol (PVA) purchased from Wako pure chemical industries, Ltd, Japan (Catalogue number 160-08295) is used as a matrix for the fabrication of SWNTs -based SA. The structure of PVA polymer can be defined as a linear chain, consisted of alternating methylene ($-CH_2-$) and hydroxymethylene ($-CH(OH)-$) units. Some of the hydroxyls are acetylated due to the preparation method of the PVA (polymerization of the vinylacetate followed by hydrolysis), Figure 4.4.

(Vinyl acetate)   (Polyvinyl acetate)   (Polyvinyl alcohol)
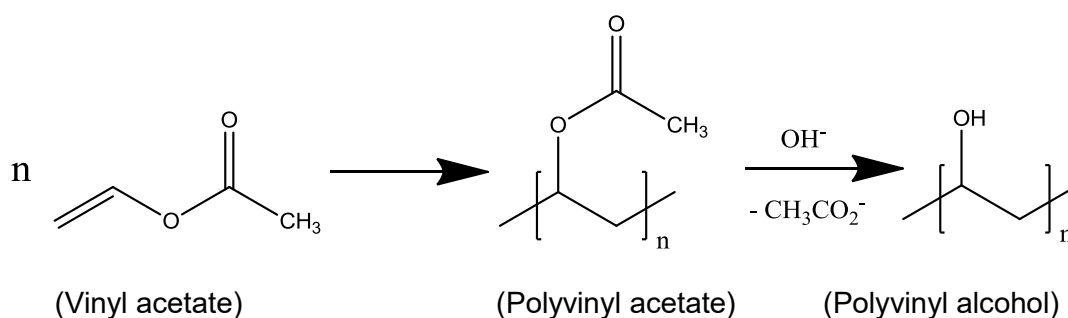
Figure 4.4:   Synthesis scheme and molecular structure of polyvinyl alcohol (PVA) used in this study.

4.3.1.2   Sample preparation:

SWNTs (2 mg) were placed in deionized water (DI) in the presence of (1 mg/mL) SDBS. Next, the mixtures of SWNTs and surfactant were subjected to ultrasonication, using NanoRuptor (Diagenode) processor for one hour at 21 kHz and 200 W. Then, the mixture was ultracentrifuged using Beckman Coulter Optima Max-XP for one hour at 17 °C, using (MLS 50 rotor) at 25000 RPM. The top 70% of the final dispersion was used as an initial SWNTs dispersion to carry out this study.

A PVA solution was prepared by adding 2 grams of PVA powder to 20 mL of DI water and left in the oven at 60 °C overnight. To prepare SWNTs-PVA composites, the initial SWNTs' dispersion was mixed with 2 mL of PVA solution and placed in the Petri dish. A freestanding film was then obtained by drying the SWNTs-PVA mixture in the desiccator for two weeks. In addition, SDBS-PVA composites (in the absence of SWNTs) were prepared by mixing 1mg/mL of SDBS solution with 2 mL of PVA and placed in the Petri dish. A freestanding film with 50µm thickness was then obtained by drying the SDBS-PVA mixture in the desiccator for two weeks.

4.4   Results and discussion

This section presents experimental studies on the characterization of the as prepared SWNTs-PVA composite before and after high power laser radiation, using a high precision optical microscope, micro Raman and scanning electron microscopy (SEM).

4.4.1   Characterization of SWNTs-PVA composite

Figure 4.5a shows the optical absorption of the nanotubes-polymer composite. Three main absorption bands are presented in the spectrum, due to SWNT interband transitions. The spectral features from 1600 to 1100 nm and from 900 to 700 nm correlate to the E_{11} and E_{22} excitonic transitions of semiconductor SWNTs (s-SWNTs), respectively [15, 107]. The spectral feature below 550 nm matches the M_{11} transition of metallic tubes (m-SWNTs) [107]. The obtained optical spectrum displays strong optical density (0.85) at absorption wavelength ~ 1560 nm, which matches the mode-locking operation of Erbium-doped fibre lasers.
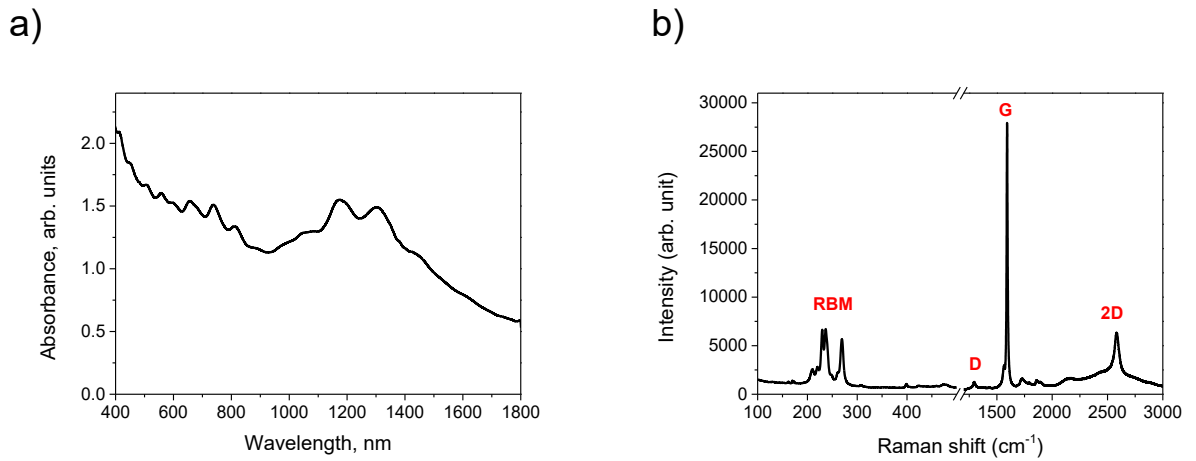
Figure 4.5:   a) UV-visible-NIR absorbance spectra: SWNT-PVA composite. The contribution from the PVA matrix has been subtracted. b) Raman spectrum of the SWNT-PVA composite measured at excitation wavelength 785 nm.

Figure 4.5b shows the Raman spectrum of the SWNT-PVA composite measured using a 785 nm laser. The key features in the Raman spectra of SWNTs are the RBMs, 150-300 cm^{-1}) and the D (disorder ~1350 cm^{-1}) and G (graphite ~1590 cm^{-1}) modes. The RBMs correspond to low-frequency vibrations of carbon atoms in the radial direction and are highly sensitive to the diameter and chirality of SWNTs. The measured spectrum for SWNT-PVA composite displays three strong peaks at 230.7, 237.4 and 270.0 cm^{-1}. The relationship between the frequency of the ω_{RBM} and the nanotube diameter was discussed previously in equation 2.6, and thus the three peaks are related to s-SWNTs with diameters of 0.97, 0.95 and 0.84 nm, respectively. Lower intensity RBM at 211 cm^{-1} corresponds to SWNT diameters of 1.17 nm, which are essential for mode-lock initiation at 1560 nm. Furthermore, Raman spectrum exhibited strong G peak and an insignificant increase in the D peak. This indicates that SWNTs' preparation does not alter the electronic properties of the source materials.

4.4.1.1   Mode-locked fibre laser based on SWNT-PVA composite

Figure 4.6a presents the experimental setup of the ring cavity erbium-doped fibre laser. The laser is pumped via a fibre Bragg grating stabilized laser diode operating at 976 nm with the maximum pump power 600 mW, using a wavelength division multiplexer (WDM). The laser cavity consists of 2 m of Erbium-doped silica fibre Liekki Er30/4-125 (EDF). The fibre-pigtailed isolator was used to ensure unidirectional operation in the ring cavity. The polarization controller (PC) provides adjustment of laser operation regimes by controlling the state of polarization in the laser cavity. The output power was extracted from the ring cavity, using a 3-dB (50:50) fused optical coupler. To create the SA, the SWNT-PVA

composite is sandwiched between two fibre connectors, as shown in figure 4.6b, and placed in the cavity between the PC and the WDM. The fibre has a core diameter of 9 µm and is embedded in 125 µm cladding of pure silica. All the optical elements are pigtailed with standard single mode SMF-28 fibre.

The mode-locking laser regime was obtained at a threshold pump power of 80mW. The total length of the laser ring cavity is ~10.8 m, resulting in fundamental repetition rate (f_{rep})= 18.5 MHz. The f_{rep} is calculated from the length of the laser cavity, using f_{rep} = C/(nL), where C is the speed of light in space measured in metre per second (m/s), n is the average refractive index of the cavity ($n \approx 1.5$ for single mode-fibre), and L is the cavity length in metres (m).
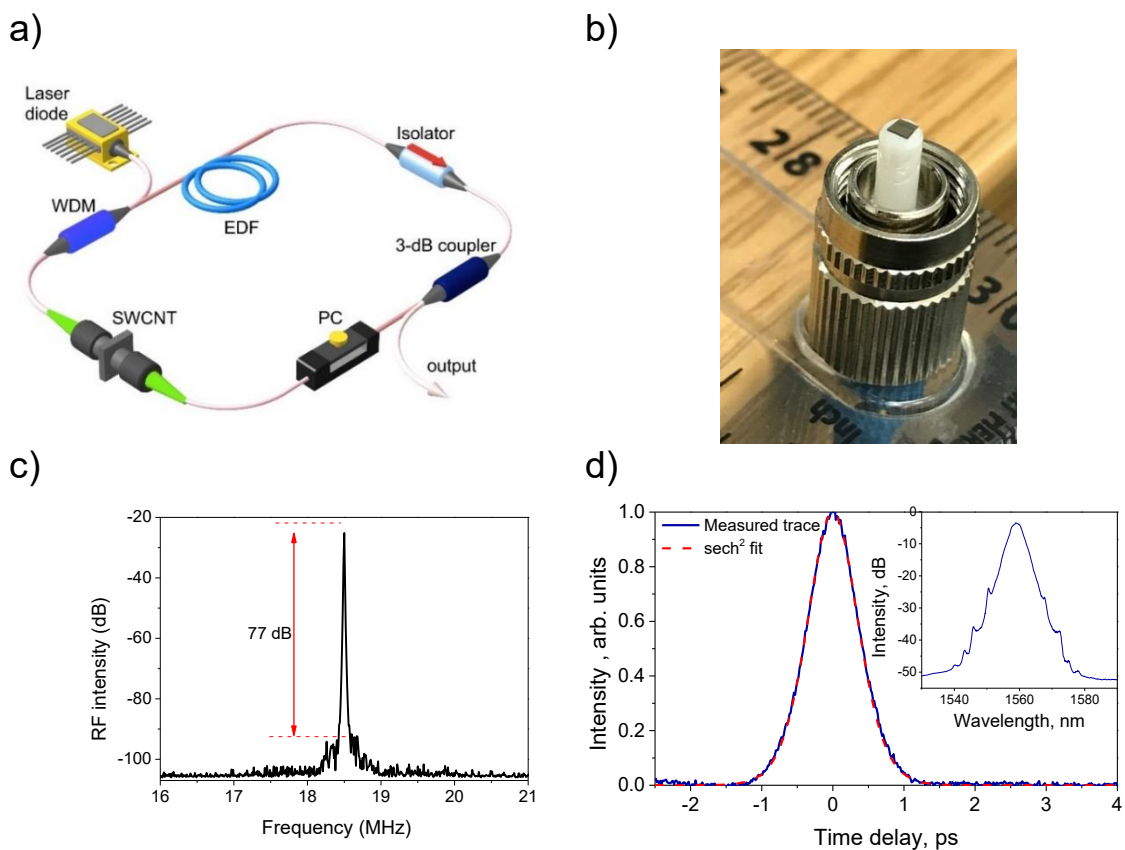
Figure 4.6 a) Experimental setup for the Erbium-doped fibre laser. b) Integration of SWNTs-PVA composite on fibre connector. C) Measured radio frequency (RF) spectrum of the laser d) Pulse autocorrelation traces and optical spectrum (inset) for fibre laser using SWNTs-PVA composite.

At the maximum pump power of 600 mW, the measured average output power reached 48.7 mW, which corresponds to the output pulse energy 2.63 nJ. This pulse energy is obtained by dividing the measured average output power (48.7 mW) by the fundamental frequency (18.5 MHz). The measured radio frequency (RF) spectrum in figure 4.6c presents

a signal-to-noise ratio (SNR) of 77dB, which confirms the stable mode-locked operation regime. Figure 4.6d shows the measured autocorrelation trace (AC) fitted to hyperbolic secant squared pulse (sech^2) profile, which allows estimating the pulse duration as 550 fs. The corresponding AC measurements of the pulse duration (τ_p) for the SA device is estimated from figure 4.6d. The τ_p is commonly deduced from the obtained AC pulse duration ($\tau_{A.c}$), which is approximately the Full width at half maximum (FWHM) of the $\tau_{A.c}$ divided by constant (1.543) [228]. Furthermore, the laser has been set to run for 24 hours continuously under the standard laboratory conditions.

During the contentious 24 hours' operation, the laser output power decreased almost linearly from 49.3 mW to 45.6 mW, and no spectral change was recorded in the optical spectrum. A stable self-starting mode-locking regime was obtained with the use of PC tuning.

4.4.1.2 Nonlinear saturable absorption properties under high power laser radiation

The SWNT-PVA composite was exposed to high power radiation for 24h, using the ring cavity illustrated in figure 4.6a. Then, the nonlinear power-dependent measurement was carried out, as shown in figure 4.7a. The output of the laser was connected to a variable attenuator and then separated into two arms using a standard 50/50 fibre fused coupler. One arm of the light source is used as a reference and the other arm containing the SA sandwiched between two fibre connectors is connected to a power meter to record the nonlinear optical measurement.

a)   b)
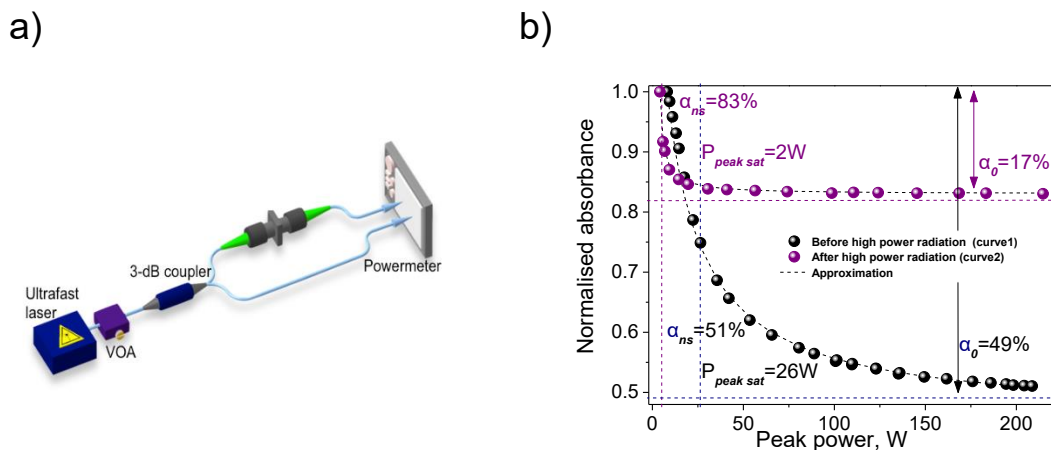
Figure 4.7: a) Laser setup to characterise power-dependent for SA device. b) Power-dependent measurements of the as prepared SWNT-PVA composite (black) and after laser operation (purple) at the maximum available pump power Ppump = 600 mW. The circles are the experimental data, and the dashed curves represent an analytical fit of the data.

Figure 4.7b compares the nonlinear properties of the sample before and after high pump power radiation. The measured α_0, α_{ns} and P_{sat} are presented in table 4.1. The change in α_0, α_{ns} and P_{sat} indicates an alteration in the materials properties of the SWNT-PVA, due to 24 hours' high power laser radiation. This conclusion is based on the observed significant decreases in the α_0 and P_{sat} with increased α_{ns} (~1.6 times) for the SWNT-PVA after high power laser radiation, compared to the as prepared one.

Table 4.1: Summary of the obtained nonlinear parameters of the SAs for SWNT-PVA composite.

Sample	Saturation Peak power (P_{sat}) (W)	Non-saturable losses (α_{ns}) (%)	Modulation depth (α_0) (%)
Before high power radiation	26	51	49
After high power radiation	2	83	17

To understand the nature of the changes, an advanced digital microscope (VHX5000, from Keyence) was used to characterize the surface morphology of the SWNT-PVA film before and after high power laser irradiation. The microscope is equipped with the VH-Z600T lens (500–5000x) magnification and the numerical aperture NA = 0.82. The average magnification used is 2000x, which provided better resolution. A resolution of 0.1 μm was employed to record the depth profile at z-axis. Figure 4.8a presents a 3D optical image of the top surface for the SWNT-PVA composite after a 40 hours' laser operation, using the maximum output power.
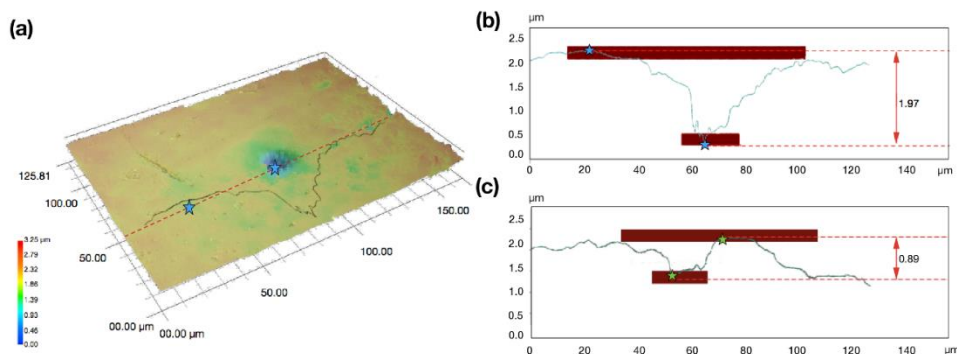
Figure 4.8   a) Optical micrographs and b) cross-sectional profile of the laser exposed areas of the SWNT-PVA composite after 40 hours of continuous laser radiation at the maximum pump power of 600 mW (average output power = 50 mW). ; c) Cross-section profile of SWNT-PVA composite film after 10 min laser (average output power = 15 mW). Adapted from [229].

Figure 4.8 reveals that the continuous laser radiation on the sample resulted in physical depression at the film surface, corresponding to the area of laser exposure. Therefore, a single crater in the SWNT-PVA film has been formed at the surface of the sample with a maximum laser penetration depth of ~1.97 μm, as shown in figures 4.8b-c. The results clearly show the damage takes place only within the first ~2μm of the area of laser exposure. Interestingly, the base of the crater (affected area) has a diameter of 9.5 μm, which corresponds to the SMF-28 mode-field diameter at 1550 nm (10.4±0.8 μm). Furthermore, when reducing the power to 15 mW for a very short time (10 minutes), the crater width at the bottom practically remained unchanged. This observation implies that the crater formation at the sample surface takes place at the very beginning of the laser operation. The stability of crater depth with laser power and duration indicates that the main reason for crater formation is the depression of the film thickness, perhaps due to the evaporation of the residual water from the SWNT-PVA film.

Additionally, the physical structure for pure PVA and the PVA-SDBS films was studied under the same laser conditions. The films in the absence of SWNTs displayed high stability against laser radiation. Meanwhile, the presence of the tubes in the composite structure resulted in significant physical changes.

Figure 4.9 presents Raman spectra for identical samples discussed in figures 4.8b-c. The samples exposed to the laser for short periods of time (up to 10 minutes) displayed no practical changes between the exposed area (bottom of the crater) and non-exposed areas (top surface). There are no changes in the energy or the shape of the G band (which can provide evidence of charge doping, strain effects, etc.). There are also no changes in the intensity of the D band (relative to the G band). Therefore, pulsed laser irradiation does not induce structural changes (damage, functionalization, etc.) to the nanotubes.
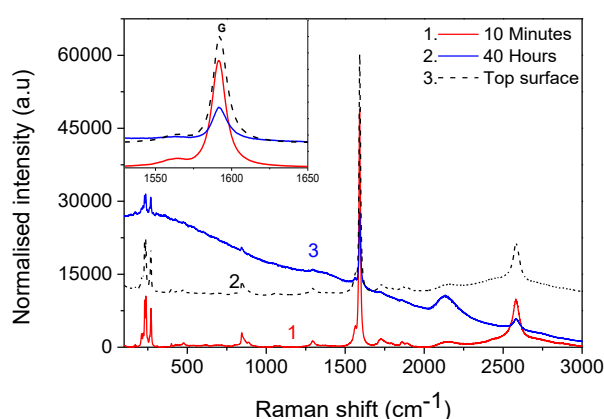
Figure 4.9   Raman spectra, measured at exposed (bottom of the crater) and unaffected areas (surface) of SWNT-PVA film after 10 min laser (average output power = 15 mW), and 40 hours of continuous laser radiation at the maximum pump power of 600 mW (average output power = 50 mW). Inset is magnified G band.

Analyzing the difference in the intensity of the G band in spectra obtained from the top surface and the bottom of the crater (ΔI_G) there is an interesting correlation with the laser conditions. In all cases, the intensity of the G band is lower at the bottom of the crater than on the top surface. For example, after 10 minutes of laser irradiation, the intensity of the G band at the bottom of the crater is 81.6% of the intensity measured on the top unaffected surface. With the increasing of laser exposure time and power, the intensity of the G band decreases further: Moreover, under the most extreme laser condition (after 40 hours of continuous irradiation, 50 mW average power) weak photoluminescence features at 1400 cm^{-1} appeared (associated with the glass slide upon which the samples were mounted) providing further evidence of decreasing the sample thickness. It is important to note that this is broadband photoluminescence, inconsistent with that expected from glass and thus suggests that this condition resulted in the largest changes in the structure and composition of the film. Although the substantial impact of photoluminescence complicates analysis, the retention of a low ratio of D and G bands intensities (I_D: I_G) and no changes in the positions of other vibrational modes imply that the nanotubes are not affected by this extreme laser condition. This observation agrees with reports concerning the very high thermal conductivity of carbon nanotubes, comparable to diamond crystal and in-plane graphite sheets [230, 231]. Moreover, it is not possible to directly assess changes in the Raman spectra of the host polymer, due to the resonance effect, which enhances the bands associated with SWNTs. However, the presence of broadband fluorescence covering a wide range of energies would suggest that the intensive ultrashort pulsed radiation has resulted in a change to the structure of the polymer. This can be attributed to the localized decomposition of PVA polymer, following removal of water during the laser radiation process, due to the dissipated heat from the tubes. According to Thomas *et al*., the PVA irreversibly decomposes in air at temperatures higher than ~190 °C, forming miscellaneous volatile products, such as acetic acid (CH_3CO_2H), formaldehyde (CH_2O) as well as CO and CO_2 gases [232]. Thermal transformations of the PVA may result in the formation of unsaturated bonds and aromatic rings in polymer structure, demonstrating the broadband fluorescence.

Figure 4.10 shows the SEM images for the SWNT-PVA film after laser irradiation. Figures 4.10a and 4.10b display the areas with (bottom of the crater) and without (top surface) the laser irradiation, respectively. Apparently, the top surface of the sample is smooth and compact and the bottom of the crater is uneven, which might contribute to scattering and results in increased non-saturable losses. This observation matches the increased non-saturable losses in table 4.1 where the non-saturable losses of the SA increased to 83% after high power radiation compared to 50% before radiation. Moreover, there is no colour difference between the bottom of the crater and the top surface, indicating no thermal

damage has resulted, due to high laser power irradiation. This finding also converges with the discussed observation related to the presence of broadband fluorescence in figure 4.9 curve 3.
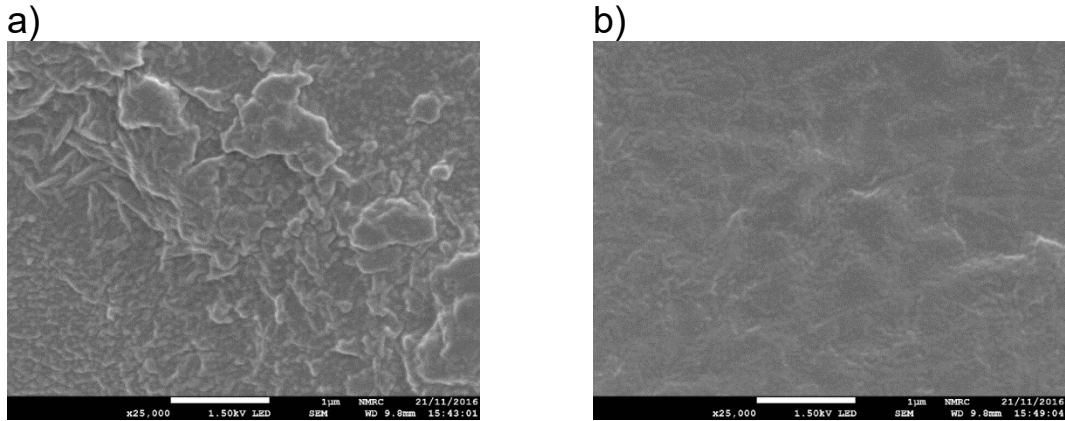
Figure 4.10   Scanning electron microscopy (SEM) image for SWNT-SA: a); bottom of the crater (b) the top surface of the sample (unexposed). All images are collected using ×25000 magnification

4.5   Chapter conclusion

In this chapter, I have reviewed the concept of generating ultrafast laser pulses using passive optical switches termed SAs and discussed the limitations with the state of the art technology. Additionally, I have then justified the motivation for using SWNTs for SA devices. Following this, I presented the fabrication and characterization of SAs made of the aqueous dispersion of SWNTs and PVA polymer. The SWNTs-PVA composite was then characterized before and after high power laser radiation, using a high precision optical microscope, micro Raman and SEM.

During the laser radiation, SWNTs conduct the major role to absorb the heat power and dissipate it to the surrounding environment, causing the removal of residual water from SWNT-PVA composite. This process results in physical depression at the film surface and formation of a crater corresponding to the area of laser exposure, presumably due to residual water desorption from the PVA composite. Good physical contact and, hence, interfacial thermal resistance, between the tube and PVA allows relatively high efficiency in thermal energy transfer. The obtained Raman measurements suggest no physical changes to the nanotubes under extreme laser conditions. Only some extent of PVA polymer

decomposition, accompanied by the appearance of broadband fluorescence and SA nonlinear parameters change, were observed.

The SA modification does not affect the laser operational performance. The main issue in this scenario is the observed laser output power degradation (from 49.3 mW to 45.6 mW). In principle, such power losses can hinder the progress of SWNTs' composite to satisfy the high average power requirement for various industrial applications. Therefore, the next chapters propose a method to integrate SWNTs into a fibre ferrule, using inkjet printing and tapered fibres.

Chapter 5: Inkjet printing of single-walled carbon nanotubes based saturable absorber

5.1 Introduction

In this chapter, the possibility of the formation of water-based SWNTs' nano ink for SAs application as an alternative to the composite approach is investigated. The motivation behind this approach is to avoid using the polymer matrix to host the nanotubes, due to the following:

1- Saturable absorption properties of the SWNTs' based polymer composites can be affected by the presence of the polymer (polymer surface reflection, absorption of the polymer matrix).

2- Results on surface modification of SWNT-PVA composite samples upon high power laser radiation have been discussed in Chapter 4, which demonstrated that this can hinder the SWNTs from satisfying the requirement of high average power for various industrial application requirements.

The inkjet printing of nanomaterials has been reported widely in the literature for various applications, including in photonic and optoelectronic [233, 234], gas sensing [235, 236], thin film transistor (TFT) [237-241] and field emission devices [242]. However, the integration of nanomaterials into the current printing technology requires tailoring of the properties of the ink to achieve effective printing conditions for specific device applications. Very recently, inkjet printing was demonstrated as a new method that offers a promising route for low cost, mass production of SAs [234]. It involves a limited number of fabrication steps and provides fully controllable and uniform deposition of ink at high resolution [243].

Additionally, the preparation of functional nanomaterials in a liquid phase offers the flexibility to choose the required materials, such as nanomaterials, dispersant and solvent and dispersion parameters, such as sonication and centrifugation to produce dispersions with the desired properties for the targeted application. For example, small diameter s-SWNTs (large band gap) are ideal ballistic conductors for applications in FET. However, the presence of m-SWNTs or even the large diameter of s-SWNTs (small band gap) can short the device [93]. The final dispersion can be then formulated as a printable ink by controlling its physical parameters, such as the density, viscosity and surface tension [244].

N-methyl-2-pyrrolidone (NMP) is known as one of the most effective organic solvents for dispersing SWNTs [78, 79]. Pure NMP is capable of dispersing SWNTs with the highest fraction (~70%) of individual nanotubes at an extremely low concentration (~0.004 mg/mL),

with a growing average bundle size as the SWNT concentration increases [78]. Moreover, individual tubes remain stable in NMP for at least three weeks [79].

However, NMP is not ideally suited for inkjet printing as well as for SWNTs' ink formation. Firstly, NMP has long drying times arising from the high boiling point ($\sim$200 $^{\circ}$C) [243, 245, 246] Moreover, NMP has relatively high surface tensions ($\sim$40 mN/m), which are comparable to those of common substrates, such as glass and silicon, and can lead to poor wetting of substrates [247, 248]. Despite these difficulties, many groups have managed to print carbon nanotubes, using NMP [249] and N,N-dimethylformamide (DMF) due to their effectiveness in dispersing SWNTs. [235-238, 242, 250].

For ease of device processability, it would, therefore, be advantageous to develop SWNTs' inks from low boiling-point solvents, such as water and alcohol. Water-based inks are environmentally friendly, easy to store, and safer to handle. However, water-based inks are not stable in the solvent alone, and are more challenging, due to the hydrophobic nature of the carbon nanotubes. This issue can be overcome using a dispersant, such as high dispersion efficiency polymers and surfactants, as discussed previously in chapters 2 and 3.

In this chapter, water-based SWNT nano ink was formulated in the presence of SDBS surfactant to print a SA device onto the core of an optical fibre edge and explore its utilization as a saturable absorber for a mode-locked Erbium-doped fibre laser (MLEDFL).

5.2   Experiment

5.2.1   Preparation of SWNT nano ink

SWNT powder (HiPco, lot no. PO279; Carbon Nanotechnologies Inc.) has been used to prepare the nanotube dispersions. 0.4 mg/mL of HiPco SWNTs was mixed in deionized water (DI) in the presence of 1 mg/mL of sodium dodecylbenzene sulfonate (SDBS) surfactant. SDBS has been selected among other ionic surfactants due to its high efficiency in dispersing SWNTs [54, 57]. Additionally, SDBS has been used here as a wetting agent to reduce the surface tension of water [251] and prevent clogging the inkjet nozzle. The above mixture was ultrasonicated using a NanoRuptor (Diagenode) processor for 1 hour at 21 kHz and 200 W. Next, the resultant mixture was subjected to ultracentrifugation for 1 hour at 17°C at 30 KRPM using Beckman Coulter Optima Max-XP, MLS 50 rotor to separate the aggregates and obtain a debundled supernatant-stabilised dispersion of SWNT. The top 50 % of the dispersion was then decanted and used as the nano ink in this study.

5.2.2 Inkjet printing of SWNT on fibre ferrule for mode-locked laser

For inkjet printing, the SWNT nano ink was loaded into the printer cartridge without dilution. The inkjet printing of SWNTs was carried out using the Autodrop micro dispersing system (Microdrop Technologies GmbH, Norderstedt, Germany), as depicted in figure 5.1a.
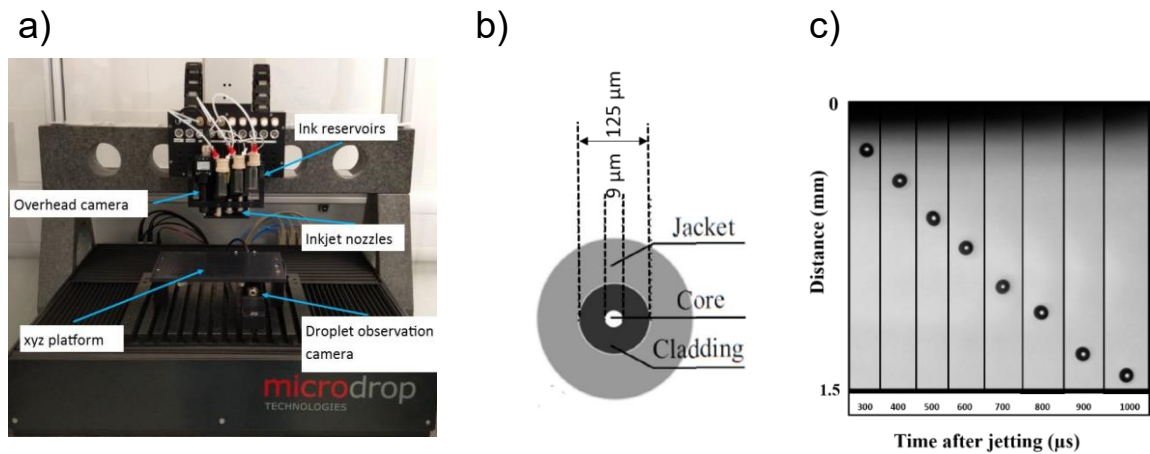
Figure 5.1   a) Inkjet printing head. b) cross section of single mode fibres (SMF-28) structure c) Photograph for the ink jetting sequence recorded by printer camera .

The system is supplied with a printing head MD-K-130 with 50 µm diameter nozzle that can move in three directions (X, Y and Z) with a working space of 200x200x80 mm and accuracy of ±5µm. The inkjet nozzle is piezo-driven and, as such, drops are controlled by the voltage pulse.

For the experimental work, the frequency of drops was set at 1 Hz to ensure the surface of the fibre core is completely dried before depositing the next drop. To control the flow of drops from the nozzle, the voltage level and pulse duration were set at 85V and 42µm, respectively.

The printing process was performed using single mode fibres (SMF-28). The cross section of SMF-28 is shown in figure 5.1b consisting of a central doped core (diameter: 9 µm), a silica cladding (diameter: 125 µm) and an outer polymer jacket (diameter: 245 µm). Typically, the core region is made of germanium doped silica $SiO_2:GeO_2$ to increase the refractive index, and the cladding is made of pure silica. This gives a higher refractive index of the core, compared to the cladding region.

The ink-substrate interactions also play a significant role in determining the quality of inkjet printing. One of the significant effects that must be avoided is the coffee ring effect, where the SWNTs are deposited at the edge of droplets, due to contact line pinning [243, 252]. When a droplet of ink is drying, the higher surface area to volume ratio at the edge of the drop leads to quicker solvent evaporation than in the centre. This causes the solvent (water in this case) to flow outwards from the centre of the drop, carrying dispersed SWNTs

outwards. These can "pin" the edge of the droplet, preventing it from receding. While pinned, the droplet covers a constant area of the substrate as the contact angle decreases to the receding contact angle. Once this is reached, the system becomes unstable and the contact area rapidly decreases, creating "rings" of deposited material rather than a uniform film.

In order to avoid the coffee ring effect, the printer head was placed around 1.5 mm above the optical fibre to allow the dispensed ink from the printer head to dry in 10 μm diameter droplets, and thus maximize the concentration of SWNTs on the optical fibre core. Once the SWNT dispersion is deposited on the fibre edge, it dries in less than one second. Therefore, the frequency of drops was set at 1 Hz to in order to print a set of SWNT-SAs with different numbers of layers (from 100 to 25,000 layers) on the flat fibre connector by carefully focusing on the fibre core.

Figure 5.1c shows the droplet jetting for the SWNT ink produced by printer head from 300 to 1000μs. Finally, a set of SWNT-SAs were printed with different layers (from 100 to 25,000 layers) by carefully focusing on the fibre core area.

5.3 Results and discussion

Absorption spectra for SWNT nano ink is presented in figure 5.2(a). Note that the recorded range of absorption is limited with the high absorption of water at wavelengths more than ~1350 nm. Deionized water (DI) was used as a reference in the measurement of the absorption spectrum to subtract the background of the water. The optical absorption spectrum was measured using the same Lambda 1050 UV-NIR spectrometer (Perkin Elmer) discussed in chapter 3. HiPco SWNTs have tube diameter distribution from~ 0.8 to 1.3 nm that give a strong optical absorption at the 1000-1600 nm band. Figure 5.2a confirms a broad resonant absorption of the E_{11} transition for the SWNT nano ink. Moreover, their intense and narrow peaks indicate the presence of isolated tubes [253]. Practically, it is not possible to measure the absorption of the printed tubes on the fibre. Therefore, the SWNT nano ink was printed on a quartz substrate and its optical absorption was recorded, as shown in figure 5.2b. Absorption peaks for inkjet-printed SWNTs on the quartz substrate are quenched and broadened compared to SWNT nano ink. This can be explained by SWNTs bundling and change in the dielectric constant [114, 119, 126]. Furthermore, the obtained spectra in figure 5.2b displayed increased absorption intensity for 3,000 layers, compared to 2,000 layers with no changes in any band positions for the absorption spectra obtained on quartz substrate. This finding indicates controllable and uniform SWNTs' layer deposition, which can allow defined optical properties for the SA device.
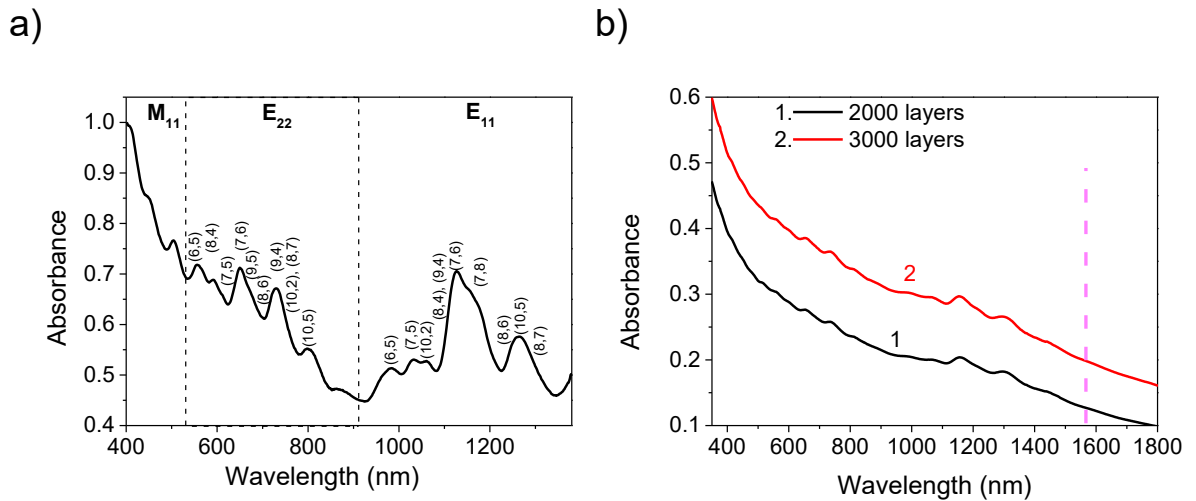
Figure 5.2   a) Optical absorbance spectra a) SWNT nano ink *b) Inkjet-printed* SWNT nano ink *on a quartz substrate (1) 2000 and (2) 3000 layers. The vertical line indicates the telecommunications C band (1550 nm).*

Additionally, the concentration of the SWNT nano ink was estimated using the Beer-Lambert law discussed in chapter 2 (equation 2.5). The absorption coefficient for HiPco SWNTs dispersed with SDBS at 600 nm was previously reported to be 215 mL.mg^{-1}.m^{-1} [56]. Therefore, the concentration of SWNT nano ink is estimated to be 0.05 mg/mL.

Raman spectra in figure 5.3 were obtained using the Horiba Jobin Yvon LabRAM HR Raman spectrometer system. Spectra were acquired using a 532 nm (2.33 eV) laser using 0.3 mW power to avoid localized heating of the sample, a 100x objective lens and a 300 μm confocal pinhole The spectral resolution in this configuration is better than 1.8 cm^{-1}.

Figure 5.3a presents Raman spectrum for germanium doped silica structure in the fibre core consistent with that expected from reference [254]. For example, the maximum peak at ~444 cm^{-1} band characterizes germanium doped silica glass. Moreover, the peaks D$_1$ (490 cm^{-1}) and D$_2$ (602 cm^{-1}) are known as defect peaks of glass. These peaks are associated with the symmetric breathing vibrations of oxygen atoms in four and three silica network structure [255]. Additionally, the band positioned at 800 cm^{-1} is assigned to antisymmetric Si-O stretching mode [256]. Furthermore, the fibre core structure is stable to 100% laser (unlike SWNT, only stable to 1% laser power).

If spectra of SWNTs (powder) and the fibre core are compared under identical conditions of laser power (0.3 mW) and acquisition time (5s), then the signal from SWNT is much higher than that from the fibre core (figure 5.3b). This can be justified by the effects of resonance from SWNT, and therefore it is not possible to resolve the fibre core in spectra collected from SWNT films printed onto the top of the fibre. The Raman spectrum for HiPco nanotubes powder shown in figure 5.3b features typical RBM with maximum intensity at 274.32 cm^{-1}, D = 1329.5 cm^{-1}, G = 1591.1 cm^{-1} and 2D = 2633.3 cm^{-1} bands. According to

the Kataura plot [107], λ_{ex}=532 nm matches the M_{11} transition of m-SWNTs. This is supported by the resulting Breit-Wigner-Fano (BWF) line shape of the G band.
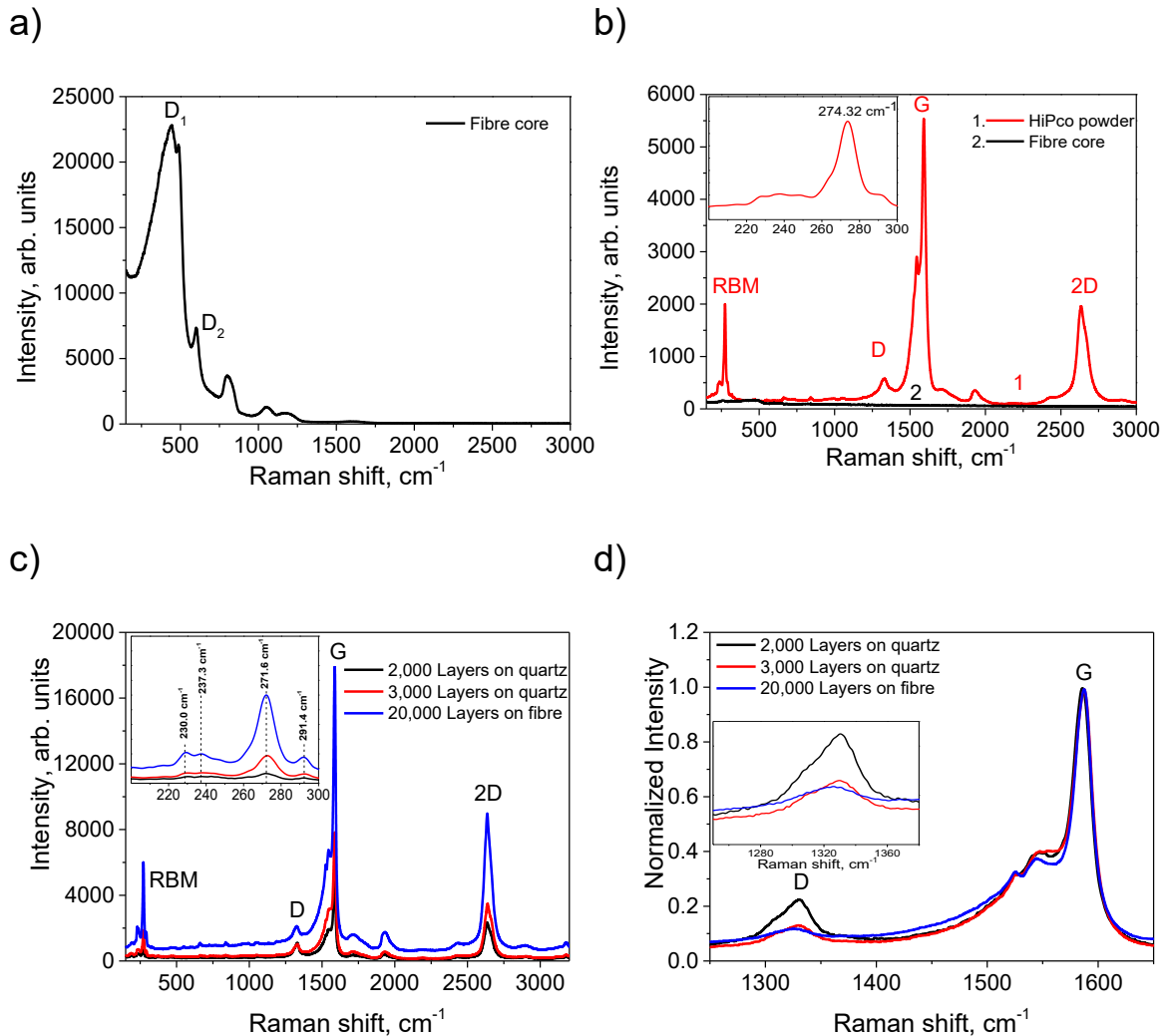
Figure 5.3   Raman measurements for a) fibre core, b) SWNTs (powder) curve 1 and the fibre core (curve 2) under identical conditions of laser power, c) SWNTs printed layers 2000 (black), 3000 (red) on quartz substrate and 20,000 on the fibre, d) figure c zoomed to D and G bands and normalized to the intensity of the G band.

Raman spectra in figure 5.3c displayed increased intensity for all bands with increased number of deposited SWNTs layers. Apparently, the 20,000 layers on the fibre core displayed higher intensity compared to 2000 and 3000 layers on quartz substrates. Moreover, no significant changes in any band positions for the Raman spectra obtained on quartz (relative to those on the fibre core). This observation is consistent with the obtained spectra in the optical absorption discussed in figure 5.2b.

The figure 5.3 c (inset) shows four prominent peaks at the RBMs mode; one dominated peak at 271.6 cm^{-1} and the other three peaks having lower intensities at 291.4 cm^{-1}, 237.3 cm^{-1} and 230 cm^{-1}. The relationship between the frequency of the RBMs and the diameter

of the nanotube (d_t) can be obtained using equation 2.6 (discussed in chapter 2). Therefore, the dominant peak at RBM matches with s-SWNTs with diameters of 0.89 nm. The lower intensity RBM at 237.3 cm^{-1} and 230 cm^{-1} correlates with SWNT diameters of 1.03 nm and 1.06, which are essential for mode-lock initiation at ~1550 nm.

Raman spectra in figure 5.3c were normalized to the intensity of the G band, as shown in figure 5.3d in order to understand the relation between SWNTs' film thickness and the intensity ratio of D and G bands ($I_D:I_G$). Raman spectra presented in figure 5.3d show that I_D decreases with increased film thickness, indicating a uniform distribution of SWNT reflecting differences in homogeneity with the number of printed layers, i.e. 20,000 on fibre core resulted in a more homogeneous distributionods nanotubes, compared to 3000 on quartz. This finding provides further evidence for the uniformity of SWNT films produced by the inkjet printing process, irrespective of the substrate. Moreover, the $I_D:I_G$ shown in figure 5.3d confirms that the dispersion and printing of SWNTs do not impact the structural, and thus optical, electrical and mechanical, properties of SWNTs, with no significant change in the $I_D:I_G$ observed (0.04).

5.3.1 Nonlinear saturable absorption of the inkjet SWNT layers

The nonlinear power-dependent measurement is carried out using a similar setup as discussed in chapter 4 (section 4.2.1) using a home-made Er-doped mode-locked laser generating a 560-fs pulse at 18.5 MHz repetition rate with 7.16 mW average output power. The instantaneous saturable absorber model expressed in equation 5.1 is implemented to estimate the SA parameters[257].

$$\alpha\left(P\right) = \frac{\alpha_o}{1 + P/P_{sat}} + \alpha_{ns} \qquad \text{Equation (5.1)}$$

where P is the incident optical power, P_{sat} is the saturation power, α_0 is the modulation depth for the SAs, and α_{ns} denotes the non-saturable loss.
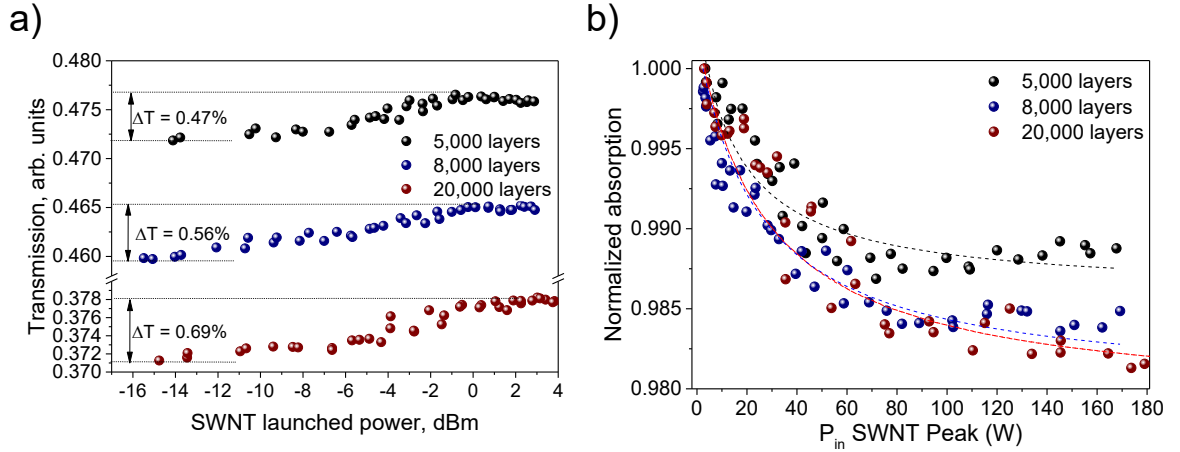
Figure 5.4: (a) Power-dependent transmission and (b) normalized absorption for the printed SWNT layers on the fibre connector, including 5,000 (black), 8,000 (blue) and 20,000 (red) layers. The circles are the experimental data, and the dashed curves represent the fitting of the data.

During the experiments, power-dependent parameters were studied for a range of samples with a maximum of 25,000 layers. The samples demonstrate saturable absorption behaviour when the number of layers exceeds 5,000. Figure 5.4 shows the power-dependent transmission figure 5.4a and normalized absorption figure 5.4b for samples comprising 5,000, 8,000 and 20,000 layers. With the increased number of printed layers, the overall transmission decreases from 48% to 37%. The saturable growth of transmission increases with the increased number of layers from 0.47% to 0.69% (figure 5.3a). Figure 5.4b demonstrates the rise in modulation depth (α_0) and saturation peak power (P_{sat}) with an increasing number of layers. For example, for the sample with 20,000 layers, the α_0 is 2.1%, while the non-saturable losses (α_{ns}) and P_{sat} are 97.9% and 30 W, respectively. The measured α_0, α_{ns} and P_{sat}, together with the values used for the best possible fitting, are summarized in table 5.1.

Table 5.1: Summary of the obtained nonlinear parameters of the inkjet SWNTs SAs

SWNT layers	P_{sat} (W)	α_{ns} (%)	α_0 (%)
5,000	19.4	98.8	1.2
8,000	22.3	98.3	1.7
20,000	30	97.9	2.1

5.3.2 Mode-locked fibre laser based on inkjet SWNT layers

Figure 5.5 presents the experimental setup of the Erbium-doped ring fibre laser pumped using laser diode operating at 980 nm wavelength with the maximum power of 600 mW, through a WDM. The laser cavity is based on a 1.5 m-long section of erbium-doped fibre (Liekki Er30/4-125 EDF). The fibre-pigtailed isolator (ISO) ensures unidirectional generation in the ring. The PC provides adjustment of the laser operation regime. The laser has 50% output through the fibre coupler. The ultrashort pulse generation is achieved by using inkjet-printed SWNT-SAs on a ferrule of an optical connector.
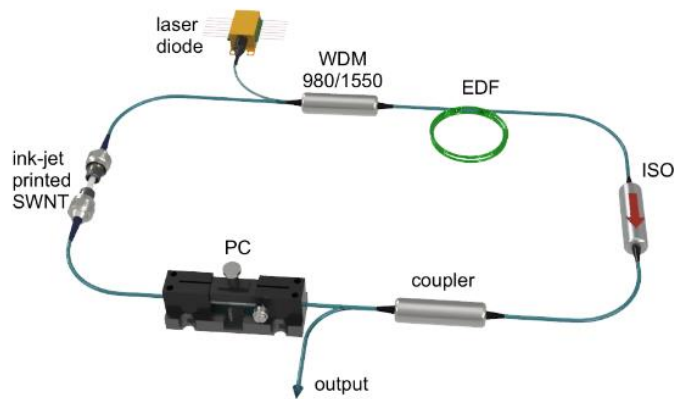
Figure 5.5   Experimental setup for the ring cavity Erbium-doped laser used in this experiment for the Inkjet-printed SWNT SA.

A range of samples with a maximum of 25,000 layers printed on top of fibre core were used to study the effect of SWNTs' layers on mode-locked pulse formation. Importantly, samples were less than 5,000 layers, i.e. those not found to exhibit SA behaviour in power-dependent measurements, were inefficient in ensuring the mode-locking regime. This can be explained by the insufficient concentration of resonant tubes to absorb the optical power at the device operation wavelength. Figure 5.6 shows the measured 3 dB optical spectra for SWNT-SAs, using 5,000, 8,000 and 20,000 layers (figure 5.6a) and the corresponding autocorrelation traces (figure 5.6b) with a well-fitted to a sech^2 temporal profile.

For SAs having 5,000 SWNTs layers, the measured optical spectrum becomes broader, and the pulse width becomes longer when the pump power increases from 15 mW to 30 mW. However, this pulse trace (for 5,000 layers) is not stable and demonstrates the onset of the MLEDFL regime.

Similarly, the measured optical spectrum and the pulse width for the SA device with 8,000 layers demonstrate practically similar performances to the SA device with 5,000 layers. Moreover, the SA device with 8,000 layers exhibited as more stable in the MLEDFL operation, compared with the SA device with 5,000 layers.
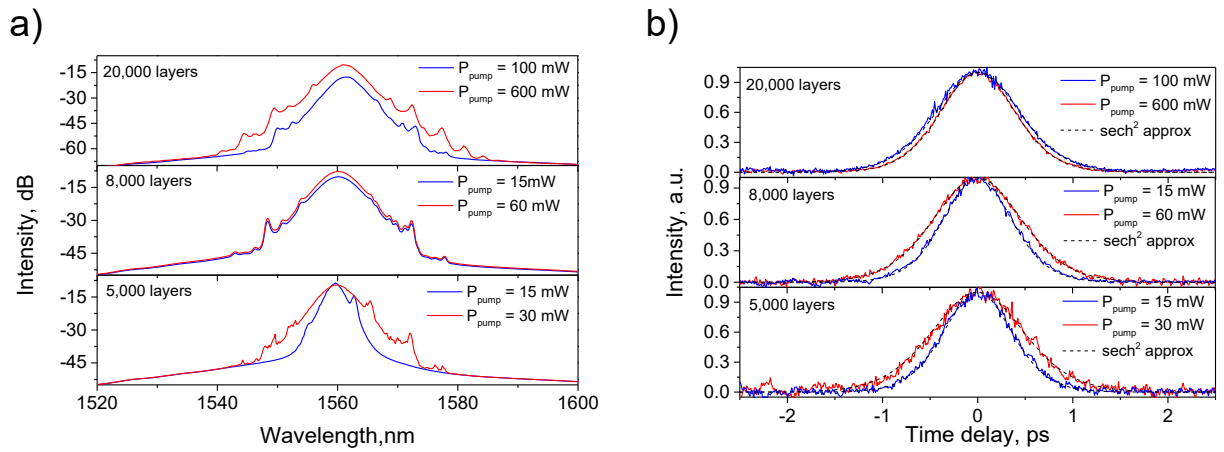
Figure 5.6   Measured optical spectra (**a**) and pulse autocorrelation traces (**b**) for different SWNT layers of the SA.

The most significant results are obtained when the number of printed layers of SWNTs' SA increases to 20,000. When the pump power increases from 100 mW to 600 mW, the measured optical spectrum becomes broader, and the pulse width becomes shorter concurrently. Importantly, the SA device was capable of operating at pump power of 600 mW and to achieve 86.2 mW average power at 1560 nm central wavelength. This is higher than all earlier reported results on SA for MLEDFL using sandwiched SWNTs [229]. Additionally, when the number of layers exceed 20,000, the ultrashort pulse generation becomes unstable and tends to switch into other regimes, i.e. Q-switching or continuous wave (CW). This can be justified with a high concentration of SWNTs, which results in large nanotube bundles formation, and hence an increase of scattering losses [258] .

The measured RF spectra with a resolution of 100 Hz for the different layers are shown in figure 5.7(a-c). The spectra are centred at the fundamental pulse repetition frequency. The small difference of the central repetition rate is due to the slightly different length of SMF-28 fibres, which are pigtailed sandwiched between two optical connectors printed SWNT-SA. It is seen that with the increase of the thickness of the SA (an increase of the number of printed layers), the signal-to-noise (SNR) is improved from 32 to 60 dB. Figure 5.7d illustrates a wide scan of RF spectrum for 20,000-layered SWNT-SA, using 300 Hz resolution.

The spectrum shows a clean frequency comb without any unwanted modulation or harmonics.
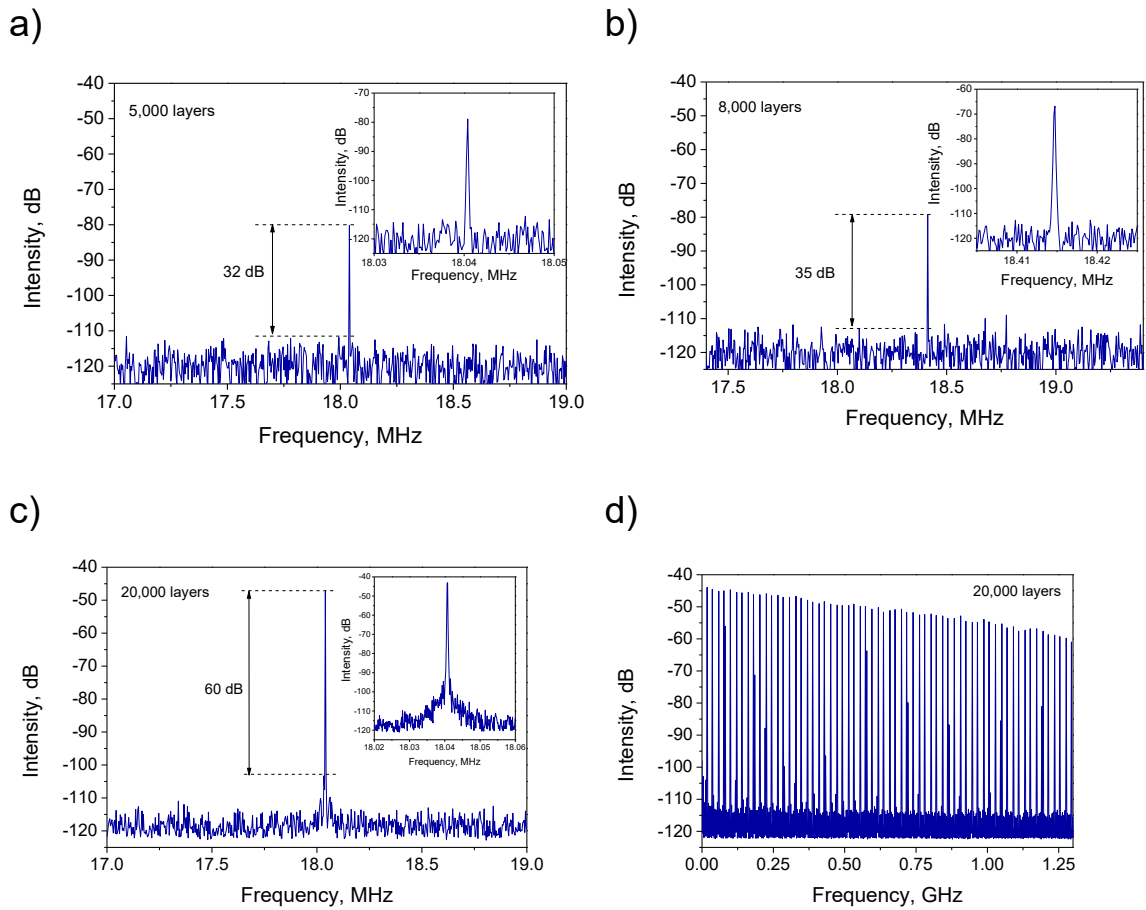
Figure 5.7   Measured RF spectra of the lasers with different SWNT printed layer on the fibre connector: 5,000 layers (a), 8,000 layers (b), 20,000 layers (c), exemplary RF spectrum measured with 1.25 GHz span using 20,000 SWNT layers (d).

Table 5.2 summarizes the output parameters of the mode-locked laser operation, including spectral bandwidth ($\Delta\lambda$), pulse duration (τ_p), repetition frequency (f_{rep}), SNR, maximum pump power (P_{max}), the threshold pump power ($P_{p.th}$), and, the average output power (P_{avg}). Here, the parameters are given at the maximum pump power, which could ensure stable mode-locking for single pulse regime. Remarkably, the 20,000-layered sample allowed the achievement of 86.2 mW average power and 4.7 nJ pulse energy directly from the oscillator at the maximum available pump power, and was limited only by the pump source used.

Table 5.2: Summary of the obtained mode-locking parameters.

N layers	$\Delta\lambda$, (nm) @ P_{max}	@ $P_{p.th}$	τ_p, (fs) @ P_{max}	@ P_{avg}	f_{rep}, (MHz)	SNR, (dB)	P_{max} (mW)	$P_{p.th}$ (mW)	P_{avg} (mW)
5,000	2.2	4	730	540	18.04	32	30	15	2.9
8,000	4.6	5	720	540	18.41	35	60	15	18.4
20,000	3.6	3.6	590	660	18.04	60	600	50	86.2

To check the stability of the presented laser, the laser has been set for free-running for ~24hours under the laboratory conditions at a pump power of ~ 300mW. The pulse average power and energy reached 47.8 mW and 2.67 nJ, respectively, with the peak power of 4.45 kW. Figure 5.8 presents the output spectrum evolution recorded with a 5-min interval. During continuous operation, there is no noticeable change in both spectral and laser output power. After several on-off cycles, the same printed sample initiates a stable self-starting mode-locking regime with the help of a PC tuning.
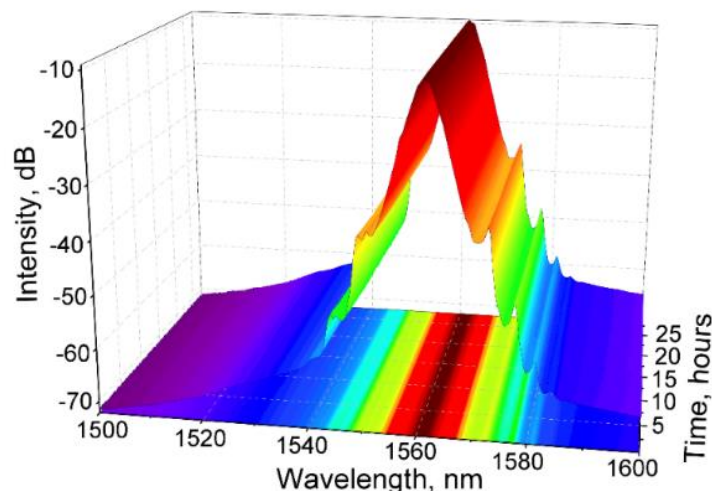
Figure 5.8   Output spectrum evolution during ~24-hour continuous operation.

5.4   Chapter conclusion

In this chapter, I presented a simple and efficient technique for the integration of SWNTs into fibre ferrule. I developed SWNTs based nano-inks for simple and effective integration with optical devices. Then, the SWNTs nano ink was directly printed on the top of the fibre connector to produce SAs with defined optical properties.

I have printed a set of SWNT-SAs with different layers (from 100 to 25,000 layers) on the edge of the fibre and deposited them onto fibre connectors, forming saturable absorbers for the fibre laser. All samples were characterized in terms of nonlinear optical properties and tested using Erbium-doped fibre laser. The experimental results have shown that the best performance in terms of pulse duration is obtained with 5000 layers of SWNTs in the SA. Further increasing of the SWNTs layers improve the laser performance in terms of power, SNR and overall generation stability. In this regard, the best performance has been obtained with the 20,000-layered sample. The sample displayed improved SNR and allowed 86.2 mW average power to be achieved directly

from the oscillator at the maximum available pump power and was limited only by the pump source used. However, the present study revealed the measured optical spectrum, and the pulse width for the SA device with 5,000 and 8,000 layers behaved differently compared to the SA device with 20,000 layers. Changing the printed layers of SWNTs for the SA mainly influences the input and output powers of the laser, spectral bandwidth and the pulse duration. Moreover, the central wavelength remained unchanged at a wavelength of 1560 nm.

Thus, the integration of SWNTs directly into a fibre ferrule using the inkjet printing technique allows us to design controllable SA parameters according to its application. These results show the feasibility of inkjet printing of nanostructured materials, particularly for controllable and reliable-SA manufacture, introducing new frontiers for various potential applications of ultrafast lasers.

Chapter 6: Tapered fibres embedded in carbon nanotube/polymer composites for ultrafast photonics

6.1 Introduction

SWNTs coated on the surfaces of D-shape fibres are reported as efficient SAs devices [259]. However, they have a strong polarization dependence, which is not desirable for some laser systems. On the other hand, SWNTs coated on the surfaces of tapered fibres are polarization insensitive, and the design of the SA can be enhanced by controlling the taper's waist and length. This approach can control the interaction length and the percentage of power and power density that leaks into the evanescent field.

SWNT-based tapered fibre devices have been demonstrated in the literature using optical depositing [260] or spray-coating [261]. However, the SAs devices fabricated using these approaches suffer from substantial scattering losses, limiting the evanescent field interaction. Moreover, these tapered fibres are directly exposed to the environment, and their performance degrades with time, making them unsuitable for real-time applications.

An alternative approach is to coat the tapered fibre with a low refractive index SWNT-polymer composite [262, 263]. The main advantages of this approach over optical deposition and spray-coating are the following:

   1- The polymer composite shields the tapered fibre from the environment ensuring long-term reliability,

   2- Dispersion of the SWNTs can be controlled in the polymer matrix, minimizing bundling and aggregation of the nanotubes. In turn, this can reduce device losses and allow for the fabrication of controllable interaction between the nanotubes and the propagating pulse.

   3- Since the SWNTs are not in direct contact with the surface of the tapered fibre, scattering losses can be considerably minimized.

Although tapered fibres coated with a low refractive index SWNTs' polymer composite offer excellent flexibility to adjust the dimensions and nonlinearity of nanotube based fibre devices, they still suffer from relatively high losses (typically exceeding 50%) and a relatively limited saturable to non-saturable loss ratio (e.g. approximately 1:8 reported by B. Xu, M *et al*. in referance [262]).

In this chapter, I demonstrate the fabrication of SWNT SAs with low losses and high saturable to non-saturable loss ratios. This is achieved by optimization of the following fabrication parameters:

1- The mixing and concentration of SWNTs in the polymer matrix to minimize excessive scattering losses.

2- The dimensions and fabrication of the tapered fibres.

3- The final deposition and thermal treatment of the SWNT-polymer mixture in the tapered fibre.

Additionally, this study highlights a trade-off between non-saturable losses and saturation power, providing guidelines for the design of SAs, according to the requirements of each specific application.

6.2   Materials and methods

In this section, I describe the fabrication of SWNT-polymer embedded tapered fibres. First, low refractive index SWNT-polymer composites are prepared following the approach proposed by reference [262]. However, N-methyl-2-pyrrolidone (NMP) is used in this study as a solvent instead of Di-methyl-formamide (DMF). The choice of NMP is justified with its efficiency in dispersing SWNTs at concentrations below 0.02 g. L^{-1} [25, 74, 75, 78, 79].

6.2.1   Materials

Low refractive index polymer (n=1.42) poly 2,2,2-trifluoroethyl methacrylate (PTFEMA) is purchased from Scientific Polymer Product, Inc (catalogue number 1014). Single-walled carbon nanotubes, fabricated by the high pressure CO (HiPco) process, were purchased from Unidym (Lot # P0261). The purity of SWNT powder is defined in the specification sheet by Unidym; the purified HiPco powder contains at least 85% of SWNT with less than 15% of impurities, such as catalyst particles, amorphous carbon, and multiwall nanotubes. HiPco SWNTs have tube diameter distribution from 0.8 to 1.3 nm. The choice of HiPco SWNTs is justified by their appreciable optical density at Erbium-doped fibre lasers emission window. This is due to the presence of tube diameters ~1.2 nm, which corresponds to a peak wavelength of about 1560 nm [225-227].

6.2.2   Preparation of SWNT-polymer film:

The SWNTs' dispersion was prepared by placing 0.1 mg/mL of HiPco SWNTs in NMP. The mixture is then sonicated, using a commercial ultrasonic processor for one hour at 200W and 20 kHz. After that, the sonicated mixture is immediately ultracentrifuged for two hours

and 30 minutes under 17°C, using (MLS 50 rotor) for 45000 revolutions per minute (RPM) to phase out impurities and residual bundles. After centrifugation, the top 60% of the resultant mixture is used as initial SWNTs' dispersion.

Poly 2,2,2-trifluoroethyl methacrylate (PTFEMA) polymer is used in this study to prepare SWNT composite, due to its low refractive index (n=1.42), compared to the cladding of silica fibre (1.44). The initial SWNTs' dispersion was diluted to 1:1 using NMP. The mixture of SWNT-NMP-PTFEMA was prepared by mixing 1mL from the diluted SWNTs' dispersion with 1gram of PTFEMA polymer. Additionally, 1 gram of PTFEMA was mixed with 1 mL of neat NMP to produce the polymer composite only (without SWNTs) as a reference sample. Moreover, I understand that the use of PVP supports the isolation and stabilization of single-walled nanotubes SWNTs in NMP [79]. However, the presence of PVP polymer in the mixture of SWNT-NMP-PTFEMA resulted in the aggregation of nanotubes. Therefore, the SWNTs-NMP dispersion was prepared without the addition of any polymer, i.e. PVP.

6.2.3   Fabrication of the SA device

In this section, I describe the fabrication of the tapered fibre coated with SWNT- PTFEMA composite. During the fabrication, a part of the fibre (L_0=3 mm long) was stretched using indirect CO_2 laser heating and pulling technique (figure 6.1a) so that the length of the taper increases by (x) after each 'pulling cycle'. By ensuring the fibre is stretched uniformly and its total volume is conserved during tapering, the waist diameter length is approximately $3/4$ compared to the previous cycle. The diameter of the tapered fibres can be calculated from $125 \times (3/4)^n$. Therefore, the tapered fibres were fabricated with waist diameters of 5.3 μm (11 cycles), 3.0 μm (13 cycles) and 2.2 μm (14 cycles), using standard single mode silica fibre (SMF 28) with an initial diameter of 125 μm [264]. The fibre is positioned along the central axis inside a sapphire tube (microfurnace) with outer and inner diameters of 1.6 mm and 0.9 mm, respectively. The fibre ends are fixed at linear translation stages A and B. Unfocused CW radiations of the carbon dioxide (CO_2) laser beam is directed, using a plane mirror to heat the sapphire tube to silica softening temperature. The optical fibre is stretched gradually in cycles while moving through the sapphire tube between stages A and B.
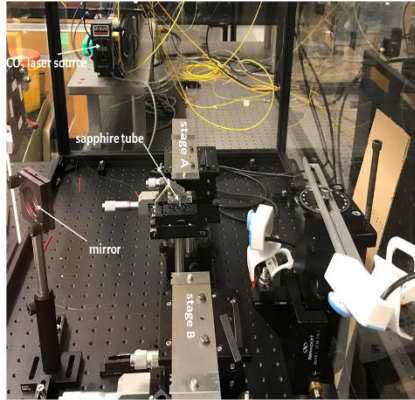
a)   b)
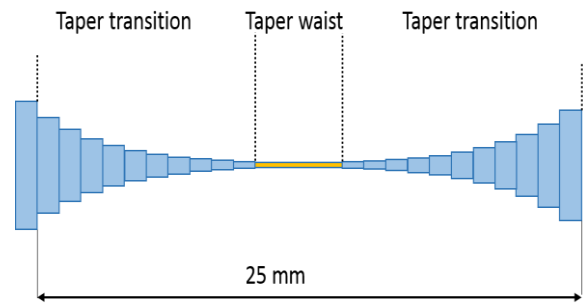
Figure 6.1:   a) Photograph of the setup for fabrication of tapered fibres using a sapphire tube heated with a CO₂ laser. b) Schematic representation for tapered single mode fibre with 11 cycles.

Typical propagation losses for the freestanding tapered fibres is from 4% to 7%. Figure 6.1b presents an example for tapered fibre using 11 cycles. The full length of the affected region (taper waist and taper transition) of a ready taper can be estimated using the following relation $L_0 + 2 \times n$, where n is the number of cycles. Therefore, a ready taper is roughly 25mm (11 cycles) to 31mm (14 cycles) in length. Importantly, all the fabricated samples have a waist length of approximately 3 mm.

After the tapering process, the fabricated samples are fixed to a glass substrate, and the waist is carefully coated with the SWNT-NMP-PTFEMA mixture. Then, the coated samples are left overnight in the oven at 60ºC to evaporate the NMP. This thermal treatment ensures homogenous and transparent SWNT-PTFEMA film on the surface of the tapered fibres.

An optical microscope is usually used to assess the quality of the SA device. It is a commonly used technique to ensure the prepared samples are homogenous and transparent. Furthermore, no large aggregates can be seen to avoid non-saturable scattering losses [265]. Figure 6.2 presents optical microscopy pictures for the SWNT-PTFEMA film deposited on the surface of the tapered fibres without (figure 6.2a) and with (figure 6.2b) thermal treatment. The sample without thermal treatment displayed poor optical properties, and, therefore, can lead to increased scattering losses [258].
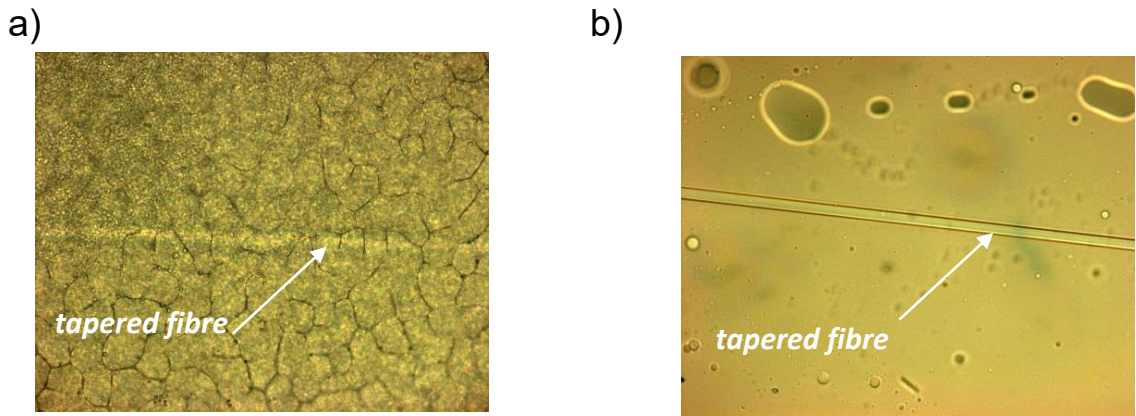
Figure 6.2: Optical microscope images for SWNT-PTFEMA film on the surface of the tapered fibres before (a) and after (b) thermal treatment. Adapted from [263].

6.2.4 Experimental setup

The optical absorption spectra were recorded using commercially available Lambda1050 Perkin Elmer UV-NIR spectrometer with 1.5 nm increment. Micro Raman spectroscopy was performed using a Horiba Jobin Yvon LabRAM HR Raman spectrometer. Spectra were acquired using a 532 nm laser (at 0.3-3.0 mW power), a 100x objective lens and a 300 µm confocal pinhole. To simultaneously scan a range of Raman shifts, a 600 lines mm^{-1} rotatable diffraction grating along a path length of 800 mm was employed. Spectra were acquired using a Synapse Charge Coupled Device (CCD detector, 1024 pixels), thermoelectrically cooled to −60 °C. Before spectra collection, the instrument was calibrated using the zero-order line and a standard Si (100) reference band at 520.7 cm^{-1}. For single point measurements, spectra were acquired over the range 100-4000 cm^{-1} with an acquisition time of 30 seconds and four accumulations to automatically remove the spikes due to cosmic rays and improve the SNR. The spectral resolution in this configuration is better than 1.8 cm^{-1}.

6.3   Results and discussion

In this section, I will discuss the preparation, characterization and the performance of the proposed SWNTs' SAs, using an erbium-doped fibre laser. First, subsection 5.2.2 describes the preparation of SWNTs' polymer composite. Next, materials' characterization using absorption, optical microscopy and Raman spectroscopy are presented in subsection 5.2.3. The nonlinear optical properties for the fabricated devices are discussed in subsection 5.3.2. The performance of the fabricated SAs devices is then characterized in subsection 5.3.3 as a SA device using erbium-doped fibre ring cavity laser. Finally, Section 5.4 concludes this chapter.

6.3.1 Materials' characterizations

Figure 6.3a represents absorption spectrum for SWNTs' dispersion in NMP. The spectral features from 1400 to 950 nm correspond to the E_{11} excitonic transitions of the s-SWNTs' chiralities, while the features below 950 to 750 nm correspond to the E_{22} excitonic transitions [15, 107]. The spectral feature below 550 nm is related to the M_{11} transition of m-SWNTs [107]. The peak in the spectral range 1000 - 1300 nm corresponds to s-SWNTs with diameters ranging from 0.8 to 1.3 nm. Although the most intense bands are centred at 1300 nm, the spectrum also shows acceptable absorption at approximately 1550 nm, due to the presence of SWNTs with diameters around 1.2 nm, which is responsible for the mode-locking of the fibre laser. Additionally, the concentration of the initial SWNTs' dispersion was estimated using the Beer-Lambert law, as discussed in chapter 2 (equation 2.5). The absorption coefficient for HiPco SWNTs in NMP at $\lambda = 660$ nm (α_{660}) was previously reported to be 4200 L g^{-1} m^{-1} [79]. Therefore, the concentration of initial SWNTs' dispersion is estimated to be 0.02 mg/mL. This means the diluted sample will make 0.01 mg/mL of SWNTs in the dispersion. Practically, it is not possible to measure the absorption of the deposited SWNTs' polymer composite on fibre. Therefore, the mixture was deposited on a quartz substrate and then left overnight in the oven at 60°C. The absorption of the SWNTs-PTFEMA film shown in figure 6.3b is strongly dominated by the polymer, due to the two orders of magnitude concentration of the polymer compared to the tubes in the composite. Furthermore, the absorption spectra in figure 6.3b displayed higher absorption intensity in curve 2 compared to curve 1, confirming higher SWNTs' concentration.

a)   b)
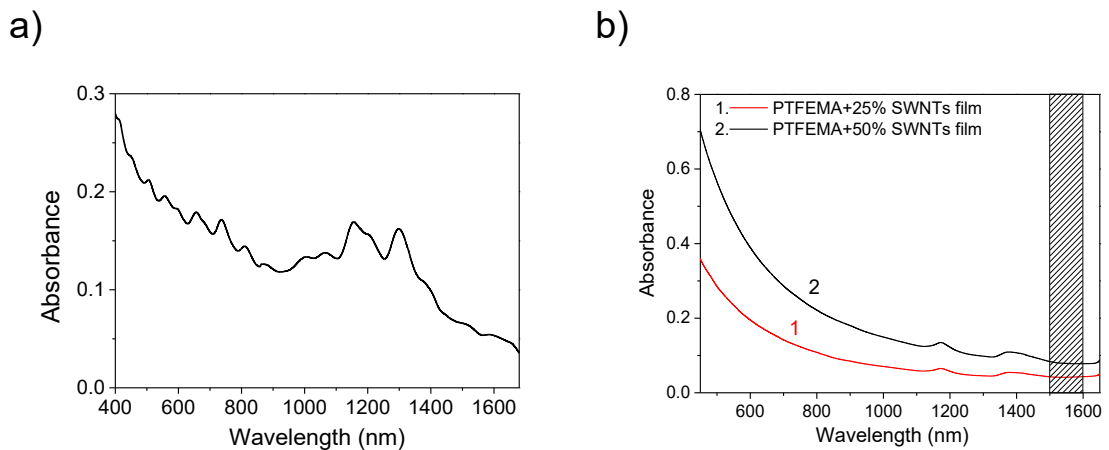
Figure 6.3   Absorption spectrum for a) SWNTs/NMP dispersion, b) SWNTs - PTFEMA thin film with 25% SWNTs' concentration (1) and 50% SWNTs' concentration (2). The bar in (b) indicates Erbium-doped fibre laser emission window i.e. 1.5–1.6 µm.

In addition, Micro Raman spectroscopy was performed to confirm the presence of the nanotubes in the film. Raman spectra in figure 6.4 investigate the structure of the SWNTs' polymer film in comparison with its components. Figure 6.4a shows Raman spectra for PTFEMA polymer in powder and film. There is practically no difference between the powder and the film, with the exception that bands associated with NMP are present in the film, indicating its integration in the composite structure.

a)   b)
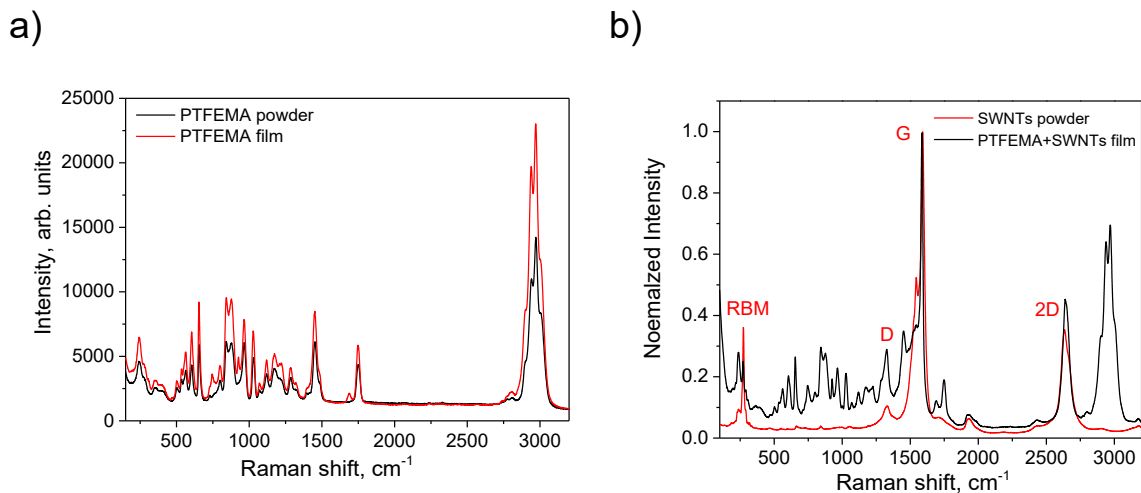
Figure 6.4   Raman spectra for a) PTFEMA powder (black) and film (red), b) normalized Raman spectra for SWNTs powder (red) and SWNTs' polymer film (black). Raman spectra were collected using laser excitation wavelength 532 nm.

Figure 6.4b displays Raman spectra for SWNTs' powder and SWNTs' polymer film. The Raman spectrum for HiPco nanotubes powder features typical RBM with maximum intensity at 273.6 cm^{-1}, D = 1329.5 cm^{-1}, G = 1591.1 cm^{-1} and 2D = 2633.3 cm^{-1}. According to the Kataura plot [107], λ_{EX}=532 nm matches the M_{11} transition of m-SWNTs. This is supported by the resulted BWF line shape of the G band. Moreover, features of HiPco at the RBM are calculated using equation 2.6 (discussed in chapter 2), and found the average tube diameter is ~0.88 nm.

The Raman spectrum for SWNT-polymer film represents a superposition of two structures (both SWNT powder and PTFEMA films). There are three observable RBMs in the spectrum of the SWNT-polymer film, with three dominant modes at 239.0, 271.5 and 291.4 cm^{-1} corresponding to tubes with diameters of 1.02, 0.89 and 0.83 nm, respectively. Lower intensity RBM at 217.3 cm^{-1} corresponds to tubes diameters of 1.13 nm, which are essential for mode-lock initiation at ~1560 nm.

Additionally, the blue shift in G band position(~5.6 cm^{-1}) in figure 6.4b suggests charge transfer from the PTFEMA to the m-SWNTs [266].

6.3.2 Nonlinear properties of SWNTs-PTFEMA coated tapered fibre devices

In this section, a power-dependent setup shown in figure 6.5 was used to measure the nonlinear properties for the SWNTs-PTFEMA SA devices, including the non-saturable losses (α_{ns}), modulation depth (α_0), and the saturation power (P_{sat}). The laser used to carry out power-dependent losses was a mode-locked fibre laser, emitting 600 fs pulses with a 25 MHz repetition rate. The input power to the devices was varied from 0.1 μm to 1500 μm, using a variable optical attenuator (VOA). The output of the VOA was divided into two arms, using standard 50/50 coupler. One arm was used to measure the reference signal and the other arm was connected to the tapered fibre. In addition, the saturable absorption properties for SA device were measured in the absence of SWNTs (as a reference sample), using a tapered fibre with a waist diameter of 5.3μm. The instantaneous saturable absorber model expressed in equation 5.1 is implemented to estimate the SA parameters [257].

$$\alpha(P) = \frac{\alpha_o}{1 + P/P_{sat}} + \alpha_{ns}$$

here, P is the incident optical power, P_{sat} is the saturation power, α_0 is the modulation depth, and α_{ns} is the non-saturable loss.
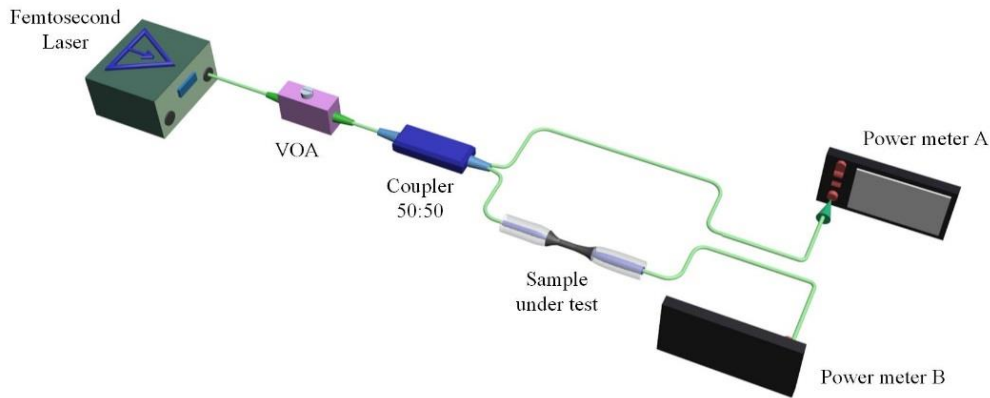
Figure 6.5   *Laser setup to characterize power-dependent for SA devices.*

The use of power in the equation 5.1 instead of the intensity as discussed previously in equation 4.2 is for more accurate representation of the device's operation. The length of the SA is significantly longer than the spatial width of a pulse, and during its propagation, the pulse will propagate through a varying mode-field diameter, power level and level of saturation.

Figure 6.6a shows the power-dependent measurement for the tapered fibre with a waist diameter of 5.3 μm coated with PTFEMA only. The obtained results show the absorption losses remain unchanged with the increased input powers, evidencing that absorption has been dominated by the PTFEMA polymer only. Moreover, the insertion losses for the tapered fibre coated with PTFEMA polymer only is approximately 9% compared to 4% - 7% insertion losses in tapered fibre suspended in air.
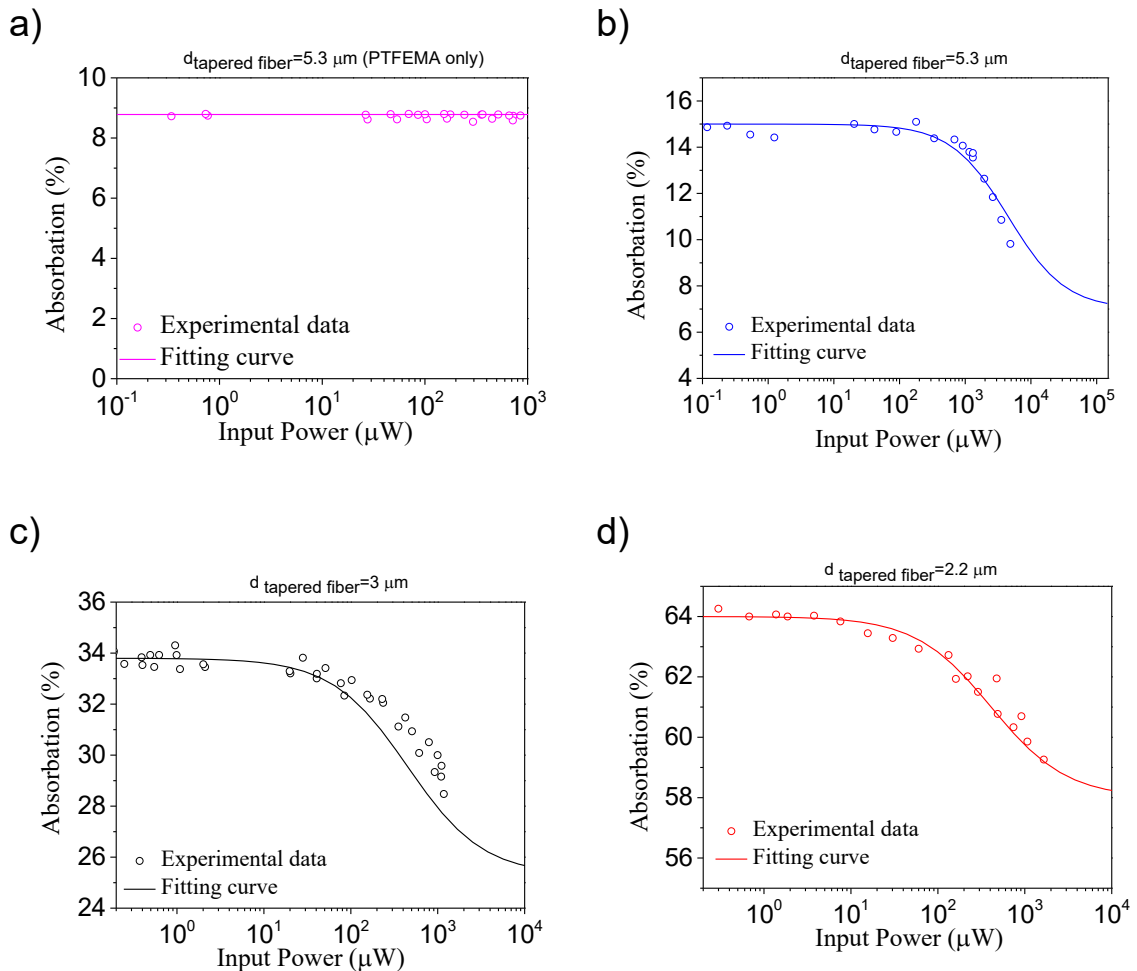
Figure 6.6   a) Losses of PTFEMA-coated taper fibre with 5.3 μm waist diameter (PTFEMA only). (b)-(d) Power-dependent losses of SWNT-PTFEMA coated taper fibres with 50% SWNT concentration and waist diameters of 5.3 μm (b), 3.0 μm (c) and 2.2 μ (d).

Figures 6.6b-c show the power-dependent absorption for three tapered fibres with waist diameters of 2.2, 3 and 5.3μm, respectively. The waist of these fibres is coated with SWNT-PTFEMA composites. The obtained nonlinear properties for the SWNTs-PTFEMA SA devices are summarized in table 6.1.

Table 6.1: Summary of the obtained nonlinear parameters of the fabricated taper fibre.

Tapered diameter (μm)	Modulation depth (α_o) (%)	Non-saturable losses (α_{ns}) (%)	Saturation power (P_{sat}) (mW)
5.3	8	7	5
3.0	8.5	25.3	0.45
2.2	6	58	0.41

Power-dependent measurements of these devices displayed interesting saturable absorption properties. First, the SA devices exhibit significantly lower insertion losses, compared to similar nanomaterial coated devices in the literature, with values of 15% and 34% for tapers of waist diameters 5.3 μm and 3.0 μm respectively. Remarkably, the studied devices displayed a saturable to non-saturable ratio of 0.35 and 0.1 for the tapers with waist diameters, 3.0 μm and 2.2 μm respectively, compared to ratios in the literature, typically lower than 0.1. Interestingly, the taper with 5.3 μm waist diameter and 15% linear losses displayed an extremely high saturable to non-saturable ratio for this type of device at approximately 1.2 (Table 6.1). On the other hand, the saturation power of the studied devices has decreased significantly by more than one order of magnitude when the taper waist diameter has decreased: from 5 mW (5.3 μm) to 0.41 mW (2.2 μm). This is expected, since smaller waist diameters lead to lower saturation powers, due to the higher power density at surface and ratio of power in the evanescent field in thinner tapers [267].

6.3.3 Mode-locked lasers using SWNT-PTFEMA coated tapered fibres

Figure 6.7 presents the experimental setup of the Erbium-doped ring fibre laser used to study the performance of the tapered fibre devices coated with SWNT-PTFEMA. The laser is pumped by a 975 nm laser diode through a 980/1550 WDM. The gain section of the laser consists of 1.1 m of erbium-doped fibre (EDF) with 80 dB/m at 1530 nm nominal absorption and group velocity dispersion of +59 ps^2/km. A single fibre isolator (ISO) was used to ensure the unidirectional regime was in the ring cavity. A PC provided adjustment of laser operation. The laser output was taken from 30% of the 70:30 standard coupler, while the remaining 70% was fed back into the cavity. The rest of the laser cavity includes 1.22 m of OFS980 fibre and approximately 5 m of standard single mode fibre SMF 28 that includes the tapered fibre devices coated with SWNT-PTFEMA that is spliced into the cavity between the PC and the ISO.
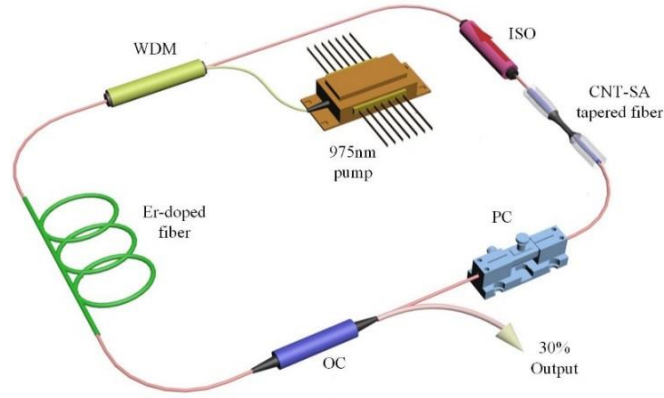
Figure 6.7   The experimental setup of the Ring cavity Er doped fibre laser used to test the performance of the SWNT-PTFEMA coated tapered fibre SAs as mode-locking devices. WDM- Wavelength division multiplexer, EDF-Erbium-doped fibre, OC 70:30 Output coupler delivering 70% of the light back in the laser cavity and 30% as output, PC-Polarization controller, ISO- Isolator.

During this study, CW lasing starts at a pump power of 13 mW for the tapered fibres with waist diameters of 5.3 μm and 3 μm and 15 mW for the tapered fibre with waist diameters of 2.2 μm. The mode-locked laser operation self-starts at pump powers of 14 mW for the 5.3 μm and 3 μm waist tapers and 16 mW for the 2.2 μm waist taper fibre. At these powers, the laser operates in its fundamental CW mode-locked regime for all three SA devices (i.e. emitting one single pulse per cavity round trip). The single-pulse laser operation remains stable regardless of the orientation of the PC in the cavity. Figure 6.8 shows the optical spectra (figure 6.8a) and its corresponding autocorrelation traces (figure 6.8b) of the fibre laser mode-locked by these three samples. Central wavelength (λ_c), spectral bandwidth ($\Delta\lambda$), and pulse duration (τ_p) are summarized in table 6.2.

Table 6.2: Summary of laser performance for the saturable devices

Tapered diameter (μm)	Central wavelength (λ_c) (nm)	Spectral bandwidth ($\Delta\lambda$) (nm)	Pulse duration (τ_p) (fs)
5.3	1569.8	2.27	1482
3.0	1566.6	5.61	430
2.2	1561.9	7.9	226

One can note that the central wavelengths are blue shifted and become wider accompanied with shorting in the pulse duration when decreasing the waist of the fibre taper. This means the thinner tapered waist enhances the interaction between the light passing in the fibre core and the SWNTs at the thinner tapered waist, compared to larger ones.
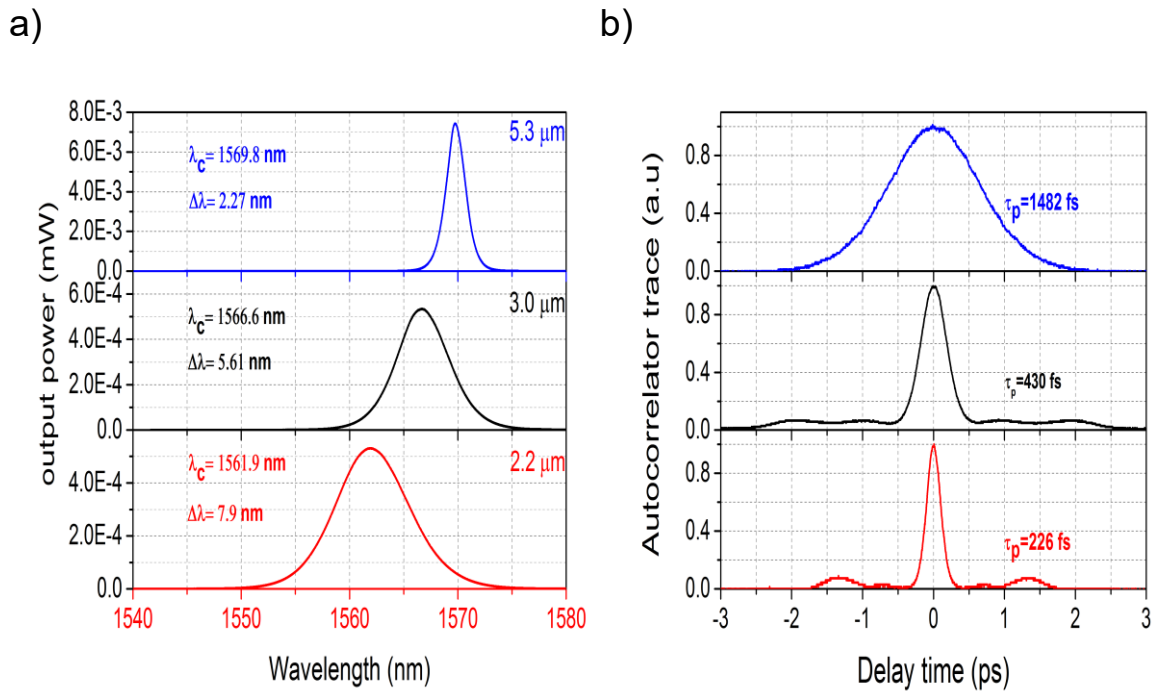
Figure 6.8 *Measured optical spectra (**a**) and pulse autocorrelation traces (**b**) for fibre laser using SWNT-PTFEMA coated tapers with waist diameters of 5.3 µm, 3.0 µm and 2.2 µm.*

The spectral bandwidth ($\Delta\lambda$) was extracted from the measured optical spectra for each SA devices. The lowest $\Delta\lambda$ (2.27 nm) was recorded for the waist diameter (5.3 µm), whereas tapered fibres with waist diameters 3 µm and 2.3 µm resulted in $\Delta\lambda$ of 5.6 nm and 7.9 nm, respectively. The corresponding autocorrelation measurements of the pulse duration (τ_p) for each SA devices was obtained form figure 6.8b. The pulse duration is commonly deduced from the obtained AC pulse duration ($\tau_{A.c}$), which is approximately the FWHM of the AC pulse duration divided by constant (1.543) [228]. The large waist diameter (5.3 µm) showed longer pulse width (1482 fs), compared to 3.0 µm (430 fs) and 2.2 µm (226 fs).

Figure 6.9 shows the measured RF spectra with a 3Hz resolution for the studied SA devices. The RF spectra show a more than 65 dB SNR for all the SA devices than confirmed stable mode-locked laser regimes.
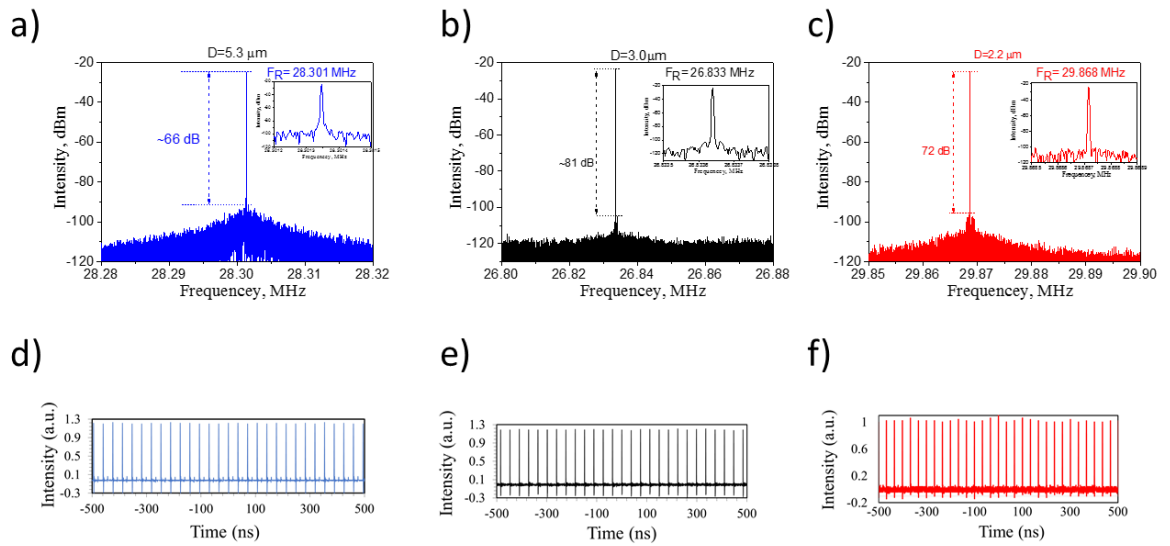
Figure 6.9   Comparison of spectral bandwidth (a) and pulse duration (b) for the fibre lasers operating at their threshold pump powers (14mW - 16mW) with three taper-based SA devices with 5.3 µm (blue), 3.0 µm (black) and 2.2 µm (red) waist diameters.

To sum up, figure 6.10 compares the performance of the studied SAs. The spectral bandwidth and pulse duration were used to evaluate the performance of the device. Figures 6.10 a-b summarize the results presented in figure 6.8, confirming that thinner tapers support the generation of shorter pulses.
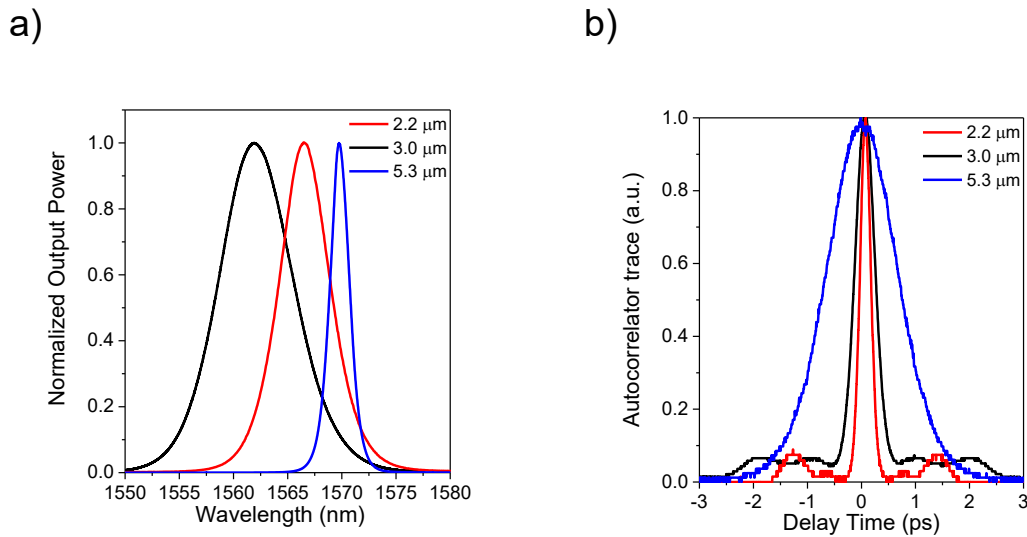
Figure 6.10   Comparison of spectral bandwidth (a) and pulse duration (b) for the fibre lasers operating at their threshold pump powers (14mW - 16mW) with three taper-based SA devices with 5.3 µm (blue), 3.0 µm (black) and 2.2 µm (red) waist diameters.

The pulse shortening effect has been discussed for other SAs (such as SESAMs) [208, 268]) and it is known to depend on the modulation depth and level of saturation of the absorber. In the studied SA devices, pulse shortening results from the attenuation of the temporal wings of the pulse by the absorber. The pulse shortening effect is not in itself unexpected. It is, however, interesting to consider a fundamental difference in terms of the dynamics of operation between SAs based on evanescent field interaction and direct interaction. Thin film absorbers can be viewed as single point absorbers with an interaction length significantly smaller than the spatial width of a pulse. Despite the high velocity of light, ultrashort pulses can also be very short in the spatial domain. In our case, they will likely be around 100s of microns. The active region of a taper should be a few mm, longer than the pulse. But thin film absorbers are sub-micron in length. This is actually an interesting and widely unexplored area of the taper-based SAs.

6.4 Chapter conclusion

In this chapter, fabrication of SWNTs-SA was demonstrated. The SAs were fabricated by exploiting the evanescent field interaction of tapered fibres with a surrounding media consisting of SWNTs hosted in a low refractive index polymer (PTFEMA). Low linear losses were obtained by improving the method of mixing the SWNTs in the polymer matrix and depositing the mixture in the tapered fibres.

A crucial benefit of reducing the losses is that it opens up the possibility of using significantly thinner and longer taper fibres, allowing us to significantly reduce the saturation power of the SA device. For example, in this chapter, I have shown a SA device with a waist diameter of 3μm and linear losses of only 25%. This SA presents a saturation power (0.45mW) 10 times lower than an identical device with a waist diameter of 5.3μm (5mW).

The trade-off between non-saturable losses and saturation power must be taken into consideration while fabricating tapered fibre based SA devices. Importantly, this study provides a guideline for the design of taper fibre based SAs not only for carbon nanotubes, but also for all other two-dimensional materials. Moreover, the method in this study allows for the fabrication of devices with controlled lateral interactions; they also open the door for studying the third order nonlinearity of SWNTs, where the nonlinearity of the device can be enhanced by the extended length of interaction between the propagating wave and the deposited tubes on the fibre core.

Chapter 7: Conclusions

This thesis aims to develop photonic systems based on carbon nanotubes with enhanced optical properties. The aim has been achieved through a systematic investigation in the following areas:

- Photoluminescence (PL) enhancement of the carbon nanotubes, due to the interaction with an organic dye;
- The stability and limitation of a widely used SWNT-PVA SA under high laser power;
- The fabrication of carbon nanotube based SAs, using inkjet printing techniques and tapered fibres, coated with carbon nanotube/polymer composites.

The main achievements can be summarized as a systematic study and realization in three main areas:

1. The development of new SWNTs' organic dye complexes with intense photoluminescence, due to the resonant energy transfer from the dyes to the SWNTs.
2. Revealing the nature of the modification of a SWNT-PVA composite based SA under the influence of high power laser radiation.
3. Design, development and characterization of advanced SA devices with controlled properties by direct printing of SWNTs' nano-inks on a standard fibre and through the formation of an effective SWNT-low refractive index composite on the surface of a fibre taper.

The main results in chapter 3 have been achieved by testing a range of newly synthesized organic dyes, supplied by the Institute of Organic Chemistry (NASU, Ukraine).

Polymethine dyes with dioxaborine terminal groups own an intense photoluminescent (PL) signal, efficient two-photon absorption, high hyperpolarizability [174], and features of effective PL probes for amines and ammonia [175-177]. Optical properties for the mixtures of a new dioxaborine dye - DOB-719 and single-wall carbon nanotubes (SWNTs) were reported in [177], showing that there is a weak interaction of the SWNT with DOB-719.

Chapter 3 demonstrates a strong interaction of the dye and the SWNTs, revealing new optical features in the spectral range of the intrinsic excitation of the dye due to resonance energy transfer (RET) from DOB-719 to SWNTs [178]. Additionally, the interaction between the dye and SWNTs resulted in an emergence of new PL peaks at the excitation wavelength

(λ_{EX}) = 735 nm and strong redshift of the intrinsic PL peaks of SWNT emission in the near infra-red range.

The study was then continued by considering various SWNT dispersions with common surfactants to compare their PL spectra in the range of λ_{EX} = 735 nm, where the RET has its maximum. The mixtures of the dye with SWNTs dispersed with anionic surfactants resulted in an even PL enhancement factor due to the RET. For all the mixtures, the maximum PL enhancement has been obtained for (6,5) SWNTs' chiralities, whereas minimum PL enhancement was observed for the (8,4) chiralities. For all the mixtures with SWNTs dispersed with the neutral and cationic surfactants, very weak RET were revealed. Furthermore, an admixture of DOB-719 to SWNTs, dispersed by cationic surfactants dramatically speeded up the bundling of SWNTs from weeks down to a couple of hours.

This kind of complex may be of interest for long-term applications such as light harvesting and bio labelling. The former is related to photovoltaic applications; carbon nanotubes are known to be good electron acceptors and allow the photo-generated electron-hole pairs to be separated when associated with various organic materials and polymers [269-274]. In this case, the use of non-covalent functionalization allows the electronic mobility of the nanotubes to be preserved, and therefore enables the losses in the device to be reduced. In the latter case, for example, the NIR emission of SWNTs could be beneficial since it covers the biological tissue window [23]. Therefore, the preservation of the PL properties of SWNTs is necessary. Whereas the molecules could be used to bind the complex with specific targets allowing functional imaging of biological tissues.

Numerous demonstrations of the stable ultrashort pulse generation in lasers mode-locked via nanotubes-polymer composite SAs have strongly stimulated the development of advanced ultrafast fibre lasers. These lasers usually present an influential platform for numerous scientific experiments to demonstrate the beauty of underlying nonlinear ultrafast optics. Meanwhile, the industrial application of carbon nanotube SAs is dubitable, since by commonly held opinion, they feature low thermal degradation thresholds and can be easily destroyed by high energy laser irradiation. To the best of the author's knowledge, no works have yet been devoted to the analysis of the nature of SWNT degradation, due to the thermal effects. Chapter 4 corrects the common understanding of the thermal degradation and damage threshold of a conventional ferrule-type SAs, sandwiching a thin polymeric film containing homogeneously dispersed SWNTs in a high power passively MLEDFL (EDFL). The findings reveal the use of SWNT-PVA film (sandwiched between optical connectors), as a SA device could endure the laser radiation exposure with the maximum optical power. Such advanced laser performance demonstrates a remarkable accord between properly designed laser cavity configurations and the hidden capability of a SWNT/polymer sample,

i.e. its high thermal damage threshold. The obtained results present a clear signature of crater formation and its geometrical stabilization after a particular time of high power laser irradiation, changing in morphology in SWNT/polymer films, particularly at the film surface. Though such modifications appeared at the early stages of the laser operation, the SWNT-SA is capable of supporting ultrashort pulse generation for several days without further deterioration of the regime. Therefore, full exploitation of the reliability and thermal tolerance of carbon nanotubes may introduce a new frontier of ultrafast real-world industrial lasers applications. The obtained results on thermal stability of SWNT-PVA composite based saturable absorbers stimulated the design of advanced saturable absorber devices with two different types of packaging of SWNTs on to optical fibres. In this work, these can be classified into those that depend on direct interaction (where the nanotubes are sandwiched between two fibre connectors), and those that rely on lateral interaction with the evanescence field of the propagating light.

In the first approach, nano-inks using functionalized SWNTs with controllable bundle sizes, having advanced optical properties, were formulated. Then, SWNTs were directly integrated on the core of a fibre edge, using the inkjet printing technique. The optical properties of the SA for different number of layers of SWNTs were investigated and compared. Mode-locked lasing has been confirmed for samples of 5,000-20,000 layers, using a femtosecond Erbium-doped fibre laser. Additionally, the study defines a direct correlation between the number of printed layers and properties of SA, showing that the SA with 20,000 layers gives the best parameters and allowed 86.2 mW average power and 4.7 nJ pulse energy to be achieved directly from the laser, generating ~600 fs pulses at an 18 MHz repetition rate. The obtained output power and pulse energy are higher than all earlier reported results on SA for erbium-doped fibre laser using sandwiched SWNT- polymer saturable absorbers. These results show the feasibility of inkjet printing of nanostructured materials, particularly for controllable and reliable-SA manufacture, introducing new frontiers for various potential applications of ultrafast lasers.

The second approach depends on the lateral interaction with the evanescence field of the propagating light. Therefore, the SA devices were fabricated by exploiting the evanescent field interaction of tapered fibres with a surrounding environment, which is made of SWNTs hosted in poly 2,2,2-trifluoroethyl methacrylate (PTFEMA) low refractive index polymer (*n=1.42*). The use of evanescence field interaction was motivated to alleviate induced thermal damage and to enhance the overall device's nonlinearity. Tapered fibres offer excellent flexibility to adjust the nonlinearity of SA devices based on nanotubes, but suffer from high losses (typically exceeding 50%) and poor saturable to non-saturable absorption ratios (typically more than 1:5). The study reveals that the tapered fibre coated with

SWNT/polymer provided long-term reliability for the SA devices, reducing device losses and allowing for the fabrication of devices with controllable lengths and waist diameters. The fabrication of low-loss SWNTs-SA devices with controllable saturation power, low losses (as low 15%) and large saturable to non-saturable loss ratios approaching 1:1, was demonstrated. This was achieved by optimizing the procedure of coating the tapered fibres in a low refractive index polymer. Additionally, this study provides guidelines for the design of SAs according to its application.

Summarizing, it is worth noting that despite almost a quarter of century of active research on carbon nanotubes, they remain a very promising material for photonics. To date, a large volume of information on optical properties has been gathered in connection with the physico-chemical state of the SWNT in solutions or composites. However, this thesis shows that it is possible to achieve essential amplification of optical properties or appearance of new optical features by means of the molecular design of complexes with SWNTs. Moreover, innovation in the packaging of SWNTs on optical platforms will lead to entirely controllable optical properties, which are urgently needed by industrial applications. It is foreseen that due to the rapid development of micro/nano fabrication, as well as printing technologies, SWNT photonics will evolve towards advanced photonic integration, offering new optical switching applications in telecoms, lasers and in various sensors and bio-medical diagnostic tools.

References:

[1] H.-E. Schaefer, *Nanoscience: the science of the small in physics, engineering, chemistry, biology and medicine*: Springer Science & Business Media, 2010.

[2] P. Avouris, Z. Chen, and V. Perebeinos, "Carbon-based electronics," *Nat Nanotechnol,* vol. 2, pp. 605-15, Oct 2007.

[3] M. F. De Volder, S. H. Tawfick, R. H. Baughman, and A. J. Hart, "Carbon nanotubes: present and future commercial applications," *Science,* vol. 339, pp. 535-9, Feb 1 2013.

[4] J. R. Lakowicz, *Principles of Fluorescence Spectroscopy*: Springer US, 2007.

[5] A. M. Gilmore, "Luminescence : the instrumental key to the future of nanotechnology," 2013.

[6] A. P. Demchenko, *Introduction to Fluorescence Sensing*, 2015.

[7] S. Chowdhury, Z. Wu, A. Jaquins-Gerstl, S. Liu, A. Dembska, B. A. Armitage*, et al.*, "Wavelength Dependence of the Fluorescence Quenching Efficiency of Nearby Dyes by Gold Nanoclusters and Nanoparticles: The Roles of Spectral Overlap and Particle Size," *J Phys Chem C Nanomater Interfaces,* vol. 115, pp. 20105-20112, 2011/10/20 2011.

[8] Y. Xu, Z. Li, A. Malkovskiy, S. Sun, and Y. Pang, "Aggregation control of squaraines and their use as near-infrared fluorescent sensors for protein," *J Phys Chem B,* vol. 114, pp. 8574-80, Jul 1 2010.

[9] D. Movia, E. Del Canto, and S. Giordani, "Purified and Oxidized Single-Walled Carbon Nanotubes as Robust Near-IR Fluorescent Probes for Molecular Imaging," *Journal of Physical Chemistry C,* vol. 114, pp. 18407-18413, Nov 4 2010.

[10] J. Lee, J. Kim, S. R. Ahmed, H. Zhou, J. M. Kim, and J. Lee, "Plasmon-induced photoluminescence immunoassay for tuberculosis monitoring using gold-nanoparticle-decorated graphene," *ACS Appl Mater Interfaces,* vol. 6, pp. 21380-8, Dec 10 2014.

[11] J. Lefebvre, Y. Homma, and P. Finnie, "Bright band gap photoluminescence from unprocessed single-walled carbon nanotubes," *Phys Rev Lett,* vol. 90, p. 217401, May 30 2003.

[12] S. Berger, F. Iglesias, P. Bonnet, C. Voisin, G. Cassabois, J. S. Lauret*, et al.*, "Optical properties of carbon nanotubes in a composite material: The role of dielectric screening and thermal expansion," *Journal of Applied Physics,* vol. 105, p. 094323, May 1 2009.

[13] L. Yu-Ming, C. T. James, F. Marcus, and A. Phaedon, "Impact of oxide substrate on electrical and optical properties of carbon nanotube devices," *Nanotechnology,* vol. 18, p. 295202, 2007.

[14] B. Chandra, V. Perebeinos, S. Berciaud, J. Katoch, M. Ishigami, P. Kim, *et al.*, "Low bias electron scattering in structure-identified single wall carbon nanotubes: role of substrate polar phonons," *Phys Rev Lett,* vol. 107, p. 146601, Sep 30 2011.

[15] M. J. Connell, S. M. Bachilo, C. B. Huffman, V. C. Moore, M. S. Strano, E. H. Haroz, *et al.*, "Band Gap Fluorescence from Individual Single-Walled Carbon Nanotubes," *Science,* vol. 297, p. 593, 2002.

[16] J. S. Lauret, C. Voisin, G. Cassabois, P. Roussignol, C. Delalande, A. Filoramo, *et al.*, "Bandgap photoluminescence of semiconducting single-wall carbon nanotubes," *Physica E-Low-Dimensional Systems & Nanostructures,* vol. 21, pp. 1057-1060, Mar 2004.

[17] W. Walden-Newman, I. Sarpkaya, and S. Strauf, "Quantum light signatures and nanosecond spectral diffusion from cavity-embedded carbon nanotubes," *Nano Lett,* vol. 12, pp. 1934-41, Apr 11 2012.

[18] S. Moritsubo, T. Murai, T. Shimada, Y. Murakami, S. Chiashi, S. Maruyama, *et al.*, "Exciton diffusion in air-suspended single-walled carbon nanotubes," *Phys Rev Lett,* vol. 104, p. 247402, Jun 18 2010.

[19] P. H. Tan, A. G. Rozhin, T. Hasan, P. Hu, V. Scardaci, W. I. Milne, *et al.*, "Photoluminescence spectroscopy of carbon nanotube bundles: evidence for exciton energy transfer," *Phys Rev Lett,* vol. 99, p. 137402, Sep 28 2007.

[20] L. J. Carlson, S. E. Maccagnano, M. Zheng, J. Silcox, and T. D. Krauss, "Fluorescence efficiency of individual carbon nanotubes," *Nano Lett,* vol. 7, pp. 3698-703, Dec 2007.

[21] P. Cherukuri, S. M. Bachilo, S. H. Litovsky, and R. B. Weisman, "Near-infrared fluorescence microscopy of single-walled carbon nanotubes in phagocytic cells," *J Am Chem Soc,* vol. 126, pp. 15638-9, Dec 8 2004.

[22] K. Welsher, Z. Liu, D. Daranciang, and H. Dai, "Selective probing and imaging of cells with single walled carbon nanotubes as near-infrared fluorescent molecules," *Nano Lett,* vol. 8, pp. 586-90, Feb 2008.

[23] Z. Liu, S. Tabakman, K. Welsher, and H. Dai, "Carbon Nanotubes in Biology and Medicine: In vitro and in vivo Detection, Imaging and Drug Delivery," *Nano Res,* vol. 2, pp. 85-120, Feb 1 2009.

[24] A. A. Boghossian, J. Zhang, P. W. Barone, N. F. Reuel, J. H. Kim, D. A. Heller, *et al.*, "Near-infrared fluorescent sensors based on single-walled carbon nanotubes for life sciences applications," *ChemSusChem,* vol. 4, pp. 848-63, Jul 18 2011.

[25] T. Hasan, Z. P. Sun, F. Q. Wang, F. Bonaccorso, P. H. Tan, A. G. Rozhin, *et al.*, "Nanotube-Polymer Composites for Ultrafast Photonics," *Advanced Materials,* vol. 21, pp. 3874-3899, Oct 19 2009.

[26] U. Keller, "Recent developments in compact ultrafast lasers," *Nature,* vol. 424, pp. 831-8, Aug 14 2003.

[27] M. Monthioux and V. L. Kuznetsov, "Who should be given the credit for the discovery of carbon nanotubes?," ed: Pergamon, 2006.

[28] S. Iijima, "Helical Microtubules of Graphitic Carbon," *Nature,* vol. 354, pp. 56-58, Nov 7 1991.

[29] C. H. Olk and J. P. Heremans, "Scanning Tunneling Spectroscopy of Carbon Nanotubes," *Journal of Materials Research,* vol. 9, pp. 259-262, Feb 1994.

[30] E. T. Thostenson, Z. F. Ren, and T. W. Chou, "Advances in the science and technology of carbon nanotubes and their composites: a review," *Composites Science and Technology,* vol. 61, pp. 1899-1912, 2001.

[31] A. Jorio, G. Dresselhaus, and M. S. Dresselhaus, *Carbon nanotubes: advanced topics in the synthesis, structure, properties and applications* vol. 111: Springer Science & Business Media, 2007.

[32] C. Shen, A. H. Brozena, and Y. Wang, "Double-walled carbon nanotubes: challenges and opportunities," *Nanoscale,* vol. 3, pp. 503-18, Feb 2011.

[33] Y. M. Piao, C. F. Chen, A. A. Green, H. Kwon, M. C. Hersam, C. S. Lee*, et al.*, "Optical and Electrical Properties of Inner Tubes in Outer Wall-Selectively Functionalized Double-Wall Carbon Nanotubes," *Journal of Physical Chemistry Letters,* vol. 2, pp. 1577-1582, Jul 7 2011.

[34] M. Dresselhaus, G. Dresselhas, and A. Jorio, "Advanced Topics in the Synthesis, Structure, Properties and Applications," ed: Springer-Verlag: Berlin Heidelberg, 2008.

[35] M. Kundrapu, J. Li, A. Shashurin, and M. Keidar, "A model of carbon nanotube synthesis in arc discharge plasmas," *Journal of Physics D-Applied Physics,* vol. 45, p. 315305, Aug 8 2012.

[36] Y. Yu, L. Gu, C. Zhu, P. A. van Aken, and J. Maier, "Tin nanoparticles encapsulated in porous multichannel carbon microtubes: preparation by single-nozzle electrospinning and application as anode material for high-performance Li-based batteries," *J Am Chem Soc,* vol. 131, pp. 15984-5, Nov 11 2009.

[37] M. José-Yacamán, M. Miki-Yoshida, L. Rendón, and J. G. Santiesteban, "Catalytic growth of carbon microtubules with fullerene structure," *Applied Physics Letters,* vol. 62, pp. 657-659, 1993.

[38] J. P. Gore and A. Sane, "Flame Synthesis of Carbon Nanotubes," in *Carbon Nanotubes - Synthesis, Characterization, Applications*, S. Yellampalli, Ed., ed Rijeka: InTech, 2011, p. Ch. 07.

[39]   D. A. Britz and A. N. Khlobystov, "Noncovalent interactions of molecules with single walled carbon nanotubes," *Chem Soc Rev,* vol. 35, pp. 637-59, Jul 2006.

[40]   P. Atkins and J. De Paula, "Physical Chemistry: Thermodynamics, structure, and change 8th ed," ed: Oxford: Oxford University Press, 2006.

[41]   L. Vaisman, H. D. Wagner, and G. Marom, "The role of surfactants in dispersion of carbon nanotubes," *Adv Colloid Interface Sci,* vol. 128-130, pp. 37-46, Dec 21 2006.

[42]   C. Backes and A. Hirsch, "Noncovalent Functionalization of carbon nanotubes," ed: John Wiley & Sons: Chichester, UK, 2010, pp. 1-48.

[43]   C. J. Shih, S. C. Lin, M. S. Strano, and D. Blankschtein, "Understanding the Stabilization of Single-Walled Carbon Nanotubes and Graphene in Ionic Surfactant Aqueous Solutions: Large-Scale Coarse-Grained Molecular Dynamics Simulation-Assisted DLVO Theory," *Journal of Physical Chemistry C,* vol. 119, pp. 1047-1060, Jan 15 2015.

[44]   S. Niyogi, M. A. Hamon, H. Hu, B. Zhao, P. Bhowmik, R. Sen*, et al.*, "Chemistry of single-walled carbon nanotubes," *Acc Chem Res,* vol. 35, pp. 1105-13, Dec 2002.

[45]   M. S. Strano, C. A. Dyke, M. L. Usrey, P. W. Barone, M. J. Allen, H. Shan*, et al.*, "Electronic structure control of single-walled carbon nanotube functionalization," *Science,* vol. 301, pp. 1519-22, Sep 12 2003.

[46]   W. Zhu, N. Minami, S. Kazaoui, and Y. Kim, "π-Chromophore-functionalized SWNTs by covalent bonding: substantial change in the optical spectra proving strong electronic interaction," *Journal of Materials Chemistry,* vol. 14, pp. 1924-1926, 2004.

[47]   A. Calzolari, N. Marzari, I. Souza, and M. B. Nardelli, "Ab initio transport properties of nanostructures from maximally localized Wannier functions," *Physical Review B,* vol. 69, p. 035108, Jan 2004.

[48]   Y. S. Lee, M. B. Nardelli, and N. Marzari, "Band structure and quantum conductance of nanostructures from maximally localized Wannier functions: the case of functionalized carbon nanotubes," *Phys Rev Lett,* vol. 95, p. 076804, Aug 12 2005.

[49]   J. L. Bahr and J. M. Tour, "Covalent chemistry of single-wall carbon nanotubes," *Journal of Materials Chemistry,* vol. 12, pp. 1952-1958, 2002.

[50]   L. J. Meng, C. L. Fu, and Q. H. Lu, "Advanced technology for functionalization of carbon nanotubes," *Progress in Natural Science,* vol. 19, pp. 801-810, Jul 10 2009.

[51]   Y. Lee and K. E. Geckeler, "Carbon Nanotubes in the Biological Interphase: The Relevance of Noncovalence," *Advanced Materials,* vol. 22, pp. 4076-4083, 2010.

[52]   T. Premkumar, R. Mezzenga, and K. E. Geckeler, "Carbon nanotubes in the liquid phase: addressing the issue of dispersion," *Small,* vol. 8, pp. 1299-313, May 7 2012.

[53] C. A. Dyke and J. M. Tour, "Overcoming the insolubility of carbon nanotubes through high degrees of sidewall functionalization," *Chemistry,* vol. 10, pp. 812-7, Feb 20 2004.

[54] M. F. Islam, E. Rojas, D. M. Bergey, A. T. Johnson, and A. G. Yodh, "High weight fraction surfactant solubilization of single-wall carbon nanotubes in water," *Nano Letters,* vol. 3, pp. 269-273, Feb 2003.

[55] V. C. Moore, M. S. Strano, E. H. Haroz, R. H. Hauge, R. E. Smalley, J. Schmidt, *et al.*, "Individually suspended single-walled carbon nanotubes in various surfactants," *Nano Letters,* vol. 3, pp. 1379-1382, Oct 2003.

[56] B. R. Priya and H. J. Byrne, "Investigation of sodium dodecyl benzene sulfonate assisted dispersion and debundling of single-wall carbon nanotubes," *Journal of Physical Chemistry C,* vol. 112, pp. 332-337, Jan 17 2008.

[57] Y. Tan and D. E. Resasco, "Dispersion of single-walled carbon nanotubes of narrow diameter distribution," *J Phys Chem B,* vol. 109, pp. 14454-60, Aug 4 2005.

[58] B. White, S. Banerjee, S. O'Brien, N. J. Turro, and I. P. Herman, "Zeta-potential measurements of surfactant-wrapped individual single-walled carbon nanotubes," *Journal of Physical Chemistry C,* vol. 111, pp. 13684-13690, Sep 20 2007.

[59] R. Bandyopadhyaya, E. Nativ-Roth, O. Regev, and R. Yerushalmi-Rozen, "Stabilization of individual carbon nanotubes in aqueous solutions," *Nano Letters,* vol. 2, pp. 25-28, Jan 2002.

[60] M. J. O'Connell, P. Boul, L. M. Ericson, C. Huffman, Y. H. Wang, E. Haroz, *et al.*, "Reversible water-solubilization of single-walled carbon nanotubes by polymer wrapping," *Chemical Physics Letters,* vol. 342, pp. 265-271, Jul 13 2001.

[61] X. Zhang, T. Liu, T. Sreekumar, S. Kumar, V. C. Moore, R. H. Hauge, *et al.*, "Poly (vinyl alcohol)/SWNT composite film," *Nano letters,* vol. 3, pp. 1285-1288, 2003.

[62] Y. Noguchi, T. Fujigaya, Y. Niidome, and N. Nakashima, "Single-walled carbon nanotubes/DNA hybrids in water are highly stable," *Chemical Physics Letters,* vol. 455, pp. 249-251, Apr 10 2008.

[63] M. S. Arnold, S. I. Stupp, and M. C. Hersam, "Enrichment of single-walled carbon nanotubes by diameter in density gradients," *Nano Lett,* vol. 5, pp. 713-8, Apr 2005.

[64] H. Cathcart, S. Quinn, V. Nicolosi, J. M. Kelly, W. J. Blau, and J. N. Coleman, "Spontaneous debundling of single-walled carbon nanotubes in DNA-based dispersions," *Journal of Physical Chemistry C,* vol. 111, pp. 66-74, Jan 11 2007.

[65] M. Zheng, A. Jagota, E. D. Semke, B. A. Diner, R. S. McLean, S. R. Lustig, *et al.*, "DNA-assisted dispersion and separation of carbon nanotubes," *Nat Mater,* vol. 2, pp. 338-42, May 2003.

[66] G. R. Dieckmann, A. B. Dalton, P. A. Johnson, J. Razal, J. Chen, G. M. Giordano*, et al.*, "Controlled assembly of carbon nanotubes by designed amphiphilic Peptide helices," *J Am Chem Soc,* vol. 125, pp. 1770-7, Feb 19 2003.

[67] H. Xie, A. Ortiz-Acevedo, V. Zorbas, R. H. Baughman, R. K. Draper, I. H. Musselman*, et al.*, "Peptide cross-linking modulated stability and assembly of peptide-wrapped single-walled carbon nanotubes," *Journal of Materials Chemistry,* vol. 15, pp. 1734-1741, 2005.

[68] V. Zorbas, A. Ortiz-Acevedo, A. B. Dalton, M. M. Yoshida, G. R. Dieckmann, R. K. Draper*, et al.*, "Preparation and characterization of individual peptide-wrapped single-walled carbon nanotubes," *J Am Chem Soc,* vol. 126, pp. 7222-7, Jun 16 2004.

[69] N. Minami, Y. Kim, K. Miyashita, S. Kazaoui, and B. Nalini, "Cellulose derivatives as excellent dispersants for single-wall carbon nanotubes as demonstrated by absorption and photoluminescence spectroscopy," *Applied Physics Letters,* vol. 88, p. 093123, 2006.

[70] T. Takahashi, K. Tsunoda, H. Yajima, and T. Ishii, "Dispersion and purification of single-wall carbon nanotubes using carboxymethylcellulose," *Japanese Journal of Applied Physics Part 1-Regular Papers Brief Communications & Review Papers,* vol. 43, pp. 3636-3639, Jun 2004.

[71] M. S. Arnold, A. A. Green, J. F. Hulvat, S. I. Stupp, and M. C. Hersam, "Sorting carbon nanotubes by electronic structure using density differentiation," *Nat Nanotechnol,* vol. 1, pp. 60-5, Oct 2006.

[72] W. Wenseleers, I. I. Vlasov, E. Goovaerts, E. D. Obraztsova, A. S. Lobach, and A. Bouwen, "Efficient isolation and solubilization of pristine single-walled nanotubes in bile salt micelles," *Advanced Functional Materials,* vol. 14, pp. 1105-1112, Nov 2004.

[73] N. Minami, Y. J. Kim, K. Miyashita, S. Kazaoui, and B. Nalini, "Cellulose derivatives as excellent dispersants for single-wall carbon nanotubes as demonstrated by absorption and photoluminescence spectroscopy," *Applied Physics Letters,* vol. 88, p. 093123, Feb 27 2006.

[74] K. D. Ausman, R. Piner, O. Lourie, R. S. Ruoff, and M. Korobov, "Organic Solvent Dispersions of Single-Walled Carbon Nanotubes: Toward Solutions of Pristine Nanotubes," *The Journal of Physical Chemistry B,* vol. 104, pp. 8911-8915, 2000/09/01 2000.

[75] J. L. Bahr, E. T. Mickelson, M. J. Bronikowski, R. E. Smalley, and J. M. Tour, "Dissolution of small diameter single-wall carbon nanotubes in organic solvents?," *Chemical Communications,* pp. 193-194, 2001.

[76] S. D. Bergin, V. Nicolosi, P. V. Streich, S. Giordani, Z. Y. Sun, A. H. Windle, *et al.*, "Towards solutions of single-walled carbon nanotubes in common solvents," *Advanced Materials,* vol. 20, pp. 1876-+, May 19 2008.

[77] S. D. Bergin, Z. Sun, P. Streich, J. Hamilton, and J. N. Coleman, "New solvents for nanotubes: approaching the dispersibility of surfactants," *The Journal of Physical Chemistry C,* vol. 114, pp. 231-237, 2009.

[78] S. Giordani, S. D. Bergin, V. Nicolosi, S. Lebedkin, M. M. Kappes, W. J. Blau, *et al.*, "Debundling of single-walled nanotubes by dilution: observation of large populations of individual nanotubes in amide solvent dispersions," *J Phys Chem B,* vol. 110, pp. 15708-18, Aug 17 2006.

[79] T. Hasan, V. Scardaci, P. H. Tan, A. G. Rozhin, W. I. Milne, and A. C. Ferrari, "Stabilization and "Debundling" of single-wall carbon nanotube dispersions in N-Methyl-2-pyrrolidone (NMP) by polyvinylpyrrolidone (PVP)," *Journal of Physical Chemistry C,* vol. 111, pp. 12594-12602, Aug 30 2007.

[80] T. Hasan, P. H. Tan, F. Bonaccorso, A. G. Rozhin, V. Scardaci, W. I. Milne, *et al.*, "Polymer-Assisted Isolation of Single Wall Carbon Nanotubes in Organic Solvents for Optical-Quality Nanotube-Polymer Composites," *Journal of Physical Chemistry C,* vol. 112, pp. 20227-20232, Dec 25 2008.

[81] D. S. Kim, D. Nepal, and K. E. Geckeler, "Individualization of Single-Walled Carbon Nanotubes: Is the Solvent Important?," *Small,* vol. 1, pp. 1117-1124, 2005.

[82] R. Krupke, F. Hennrich, O. Hampe, and M. M. Kappes, "Near-infrared absorbance of single-walled carbon nanotubes dispersed in dimethylformamide," *Journal of Physical Chemistry B,* vol. 107, pp. 5667-5669, Jun 19 2003.

[83] B. J. Landi, H. J. Ruf, J. J. Worman, and R. P. Raffaelle, "Effects of alkyl amide solvents on the dispersion of single-wall carbon nanotubes," *Journal of Physical Chemistry B,* vol. 108, pp. 17089-17095, Nov 4 2004.

[84] Y. Kang and T. A. Taton, "Micelle-encapsulated carbon nanotubes: a route to nanotube composites," *J Am Chem Soc,* vol. 125, pp. 5650-1, May 14 2003.

[85] Y. Maeda, S. Kimura, Y. Hirashima, M. Kanda, Y. F. Lian, T. Wakahara, *et al.*, "Dispersion of single-walled carbon nanotube bundles in nonaqueous solution," *Journal of Physical Chemistry B,* vol. 108, pp. 18395-18397, Dec 2 2004.

[86] A. Star, Y. Liu, K. Grant, L. Ridvan, J. F. Stoddart, D. W. Steuerman, *et al.*, "Noncovalent side-wall functionalization of single-walled carbon nanotubes," *Macromolecules,* vol. 36, pp. 553-560, Feb 11 2003.

[87] C. M. Hansen, *Hansen solubility parameters: a user's handbook*: CRC press, 2007.

[88] M. Rubinstein and R. H. Colby, *Polymer physics* vol. 23: Oxford University Press New York, 2003.

[89]   Y. Hernandez, V. Nicolosi, M. Lotya, F. M. Blighe, Z. Sun, S. De, *et al.*, "High-yield production of graphene by liquid-phase exfoliation of graphite," *Nat Nanotechnol,* vol. 3, pp. 563-8, Sep 2008.

[90]   T. Hasan, V. Scardaci, P. H. Tan, A. G. Rozhin, W. I. Milne, and A. C. Ferrari, "Dispersibility and stability improvement of unfunctionalized nanotubes in amide solvents by polymer wrapping," *Physica E-Low-Dimensional Systems & Nanostructures,* vol. 40, pp. 2414-2418, May 2008.

[91]   M. Zheng, "Sorting carbon nanotubes," *Topics in Current Chemistry,* vol. 375, p. 13, 2017.

[92]   B. K. Kaushik and M. K. Majumder, "Carbon nanotube: properties and applications," in *Carbon Nanotube Based VLSI Interconnects*, ed: Springer, 2015, pp. 17-37.

[93]   R. Krupke, F. Hennrich, H. Lohneysen, and M. M. Kappes, "Separation of metallic from semiconducting single-walled carbon nanotubes," *Science,* vol. 301, pp. 344-7, Jul 18 2003.

[94]   C. Jiaming, Y. Dehua, Z. Xiang, Z. Naigen, and L. Huaping, "Recent progress on the structure separation of single-wall carbon nanotubes," *Nanotechnology,* vol. 28, p. 452001, 2017.

[95]   S. K. Doorn, M. S. Strano, M. J. O'Connell, E. H. Haroz, K. L. Rialon, R. H. Hauge*, et al.*, "Capillary electrophoresis separations of bundled and individual carbon nanotubes," *Journal of Physical Chemistry B,* vol. 107, pp. 6063-6069, Jun 26 2003.

[96]   D. A. Heller, R. M. Mayrhofer, S. Baik, Y. V. Grinkova, M. L. Usrey, and M. S. Strano, "Concomitant length and diameter separation of single-walled carbon nanotubes," *J Am Chem Soc,* vol. 126, pp. 14567-73, Nov 10 2004.

[97]   F. Bonaccorso, T. Hasan, P. H. Tan, C. Sciascia, G. Privitera, G. Di Marco*, et al.*, "Density Gradient Ultracentrifugation of Nanotubes: Interplay of Bundling and Surfactants Encapsulation," *Journal of Physical Chemistry C,* vol. 114, pp. 17267-17285, Oct 21 2010.

[98]   Y. Kazuhiro, M. Yasumitsu, and K. Hiromichi, "Optical and Conductive Characteristics of Metallic Single-Wall Carbon Nanotubes with Three Basic Colors; Cyan, Magenta, and Yellow," *Applied Physics Express,* vol. 1, p. 034003, 2008.

[99]   M. Zheng, A. Jagota, M. S. Strano, A. P. Santos, P. Barone, S. G. Chou*, et al.*, "Structure-based carbon nanotube sorting by sequence-dependent DNA assembly," *Science,* vol. 302, pp. 1545-8, Nov 28 2003.

[100]   Y. Feng, Y. Miyata, K. Matsuishi, and H. Kataura, "High-Efficiency Separation of Single-Wall Carbon Nanotubes by Self-Generated Density Gradient Ultracentrifugation," *Journal of Physical Chemistry C,* vol. 115, pp. 1752-1756, Feb 10 2011.

[101] C. M. Homenick, A. Rousina-Webb, F. Y. Cheng, M. B. Jakubinek, P. R. L. Malenfant, and B. Simard, "High-Yield, Single-Step Separation of Metallic and Semiconducting SWCNTs Using Block Copolymers at Low Temperatures," *Journal of Physical Chemistry C,* vol. 118, pp. 16156-16164, Jul 24 2014.

[102] J. Crochet, M. Clemens, and T. Hertel, "Quantum yield heterogeneities of aqueous single-wall carbon nanotube suspensions," *J Am Chem Soc,* vol. 129, pp. 8058-9, Jul 4 2007.

[103] T. Takeshi, J. Hehua, M. Yasumitsu, and K. Hiromichi, "High-Yield Separation of Metallic and Semiconducting Single-Wall Carbon Nanotubes by Agarose Gel Electrophoresis," *Applied Physics Express,* vol. 1, p. 114001, 2008.

[104] H. Liu, D. Nishide, T. Tanaka, and H. Kataura, "Large-scale single-chirality separation of single-wall carbon nanotubes by simple gel chromatography," *Nat Commun,* vol. 2, p. 309, 05/10/online 2011.

[105] Y. Yomogida, T. Tanaka, M. Zhang, M. Yudasaka, X. Wei, and H. Kataura, "Industrial-scale separation of high-purity single-chirality single-wall carbon nanotubes for biological imaging," *Nat Commun,* vol. 7, p. 12056, Jun 28 2016.

[106] X. J. Wei, T. Tanaka, Y. Yomogida, N. Sato, R. Saito, and H. Kataura, "Experimental determination of excitonic band structures of single-walled carbon nanotubes using circular dichroism spectra," *Nature Communications,* vol. 7, p. 12899, Oct 5 2016.

[107] H. Kataura, Y. Kumazawa, Y. Maniwa, I. Umezu, S. Suzuki, Y. Ohtsuka*, et al.*, "Optical properties of single-wall carbon nanotubes," *Synthetic Metals,* vol. 103, pp. 2555-2558, Jun 1999.

[108] F. Wang, G. Dukovic, L. E. Brus, and T. F. Heinz, "The optical resonances in carbon nanotubes arise from excitons," *Science,* vol. 308, pp. 838-41, May 6 2005.

[109] J. Maultzsch, R. Pomraenke, S. Reich, E. Chang, D. Prezzi, A. Ruini*, et al.*, "Exciton binding energies in carbon nanotubes from two-photon photoluminescence," *Physical Review B,* vol. 72, p. 241402, Dec 2005.

[110] K. Matsuda, "1 - Fundamental optical properties of carbon nanotubes and graphene," in *Carbon Nanotubes and Graphene for Photonic Applications*, ed: Woodhead Publishing, 2013, pp. 3-25.

[111] R. Saito, G. Dresselhaus, and M. S. Dresselhaus, "Trigonal warping effect of carbon nanotubes," *Physical Review B,* vol. 61, pp. 2981-2990, Jan 15 2000.

[112] A. Hagen and T. Hertel, "Quantitative analysis of optical spectra from individual single-wall carbon nanotubes," *Nano letters,* vol. 3, pp. 383-388, 2003.

[113] C. Fantini, A. Jorio, M. Souza, M. S. Strano, M. S. Dresselhaus, and M. A. Pimenta, "Optical transition energies for carbon nanotubes from resonant Raman

spectroscopy: environment and temperature effects," *Phys Rev Lett,* vol. 93, p. 147406, Oct 1 2004.

[114] M. J. O'Connell, S. Sivaram, and S. K. Doorn, "Near-infrared resonance Raman excitation profile studies of single-walled carbon nanotube intertube interactions: A direct comparison of bundled and individually dispersed HiPco nanotubes," *Physical Review B,* vol. 69, p. 235415, 2004.

[115] S. Reich, C. Thomsen, and P. Ordejon, "Electronic band structure of isolated and bundled carbon nanotubes," *Physical Review B,* vol. 65, p. 155411, Apr 15 2002.

[116] P. H. Tan, T. Hasan, F. Bonaccorso, V. Scardaci, A. G. Rozhin, W. I. Milne*, et al.*, "Optical properties of nanotube bundles by photoluminescence excitation and absorption spectroscopy," *Physica E-Low-Dimensional Systems & Nanostructures,* vol. 40, pp. 2352-2359, May 2008.

[117] R. B. Capaz, C. D. Spataru, S. Ismail-Beigi, and S. G. Louie, "Diameter and chirality dependence of exciton properties in carbon nanotubes," *Physical Review B,* vol. 74, p. 121401, Sep 2006.

[118] P. Finnie, Y. Homma, and J. Lefebvre, "Band-gap shift transition in the photoluminescence of single-walled carbon nanotubes," *Physical Review Letters,* vol. 94, p. 247401, Jun 24 2005.

[119] A. G. Walsh, A. N. Vamivakas, Y. Yin, S. B. Cronin, M. S. Unlu, B. B. Goldberg*, et al.*, "Screening of excitons in single, suspended carbon nanotubes," *Nano Lett,* vol. 7, pp. 1485-8, Jun 2007.

[120] T. Hasan, Z. Sun, P. Tan, D. Popa, E. Flahaut, E. J. Kelleher*, et al.*, "Double-wall carbon nanotubes for wide-band, ultrafast pulse generation," *ACS Nano,* vol. 8, pp. 4836-47, May 27 2014.

[121] H. Hirori, K. Matsuda, and Y. Kanemitsu, "Exciton energy transfer between the inner and outer tubes in double-walled carbon nanotubes," *Physical Review B,* vol. 78, p. 113409, Sep 2008.

[122] K. Liu, J. Deslippe, F. Xiao, R. B. Capaz, X. Hong, S. Aloni*, et al.*, "An atlas of carbon nanotube optical transitions," *Nat Nanotechnol,* vol. 7, pp. 325-9, Apr 15 2012.

[123] A. Di Crescenzo, D. Demurtas, A. Renzetti, G. Siani, P. De Maria, M. Meneghetti*, et al.*, "Disaggregation of single-walled carbon nanotubes (SWNTs) promoted by the ionic liquid-based surfactant 1-hexadecyl-3-vinyl-imidazolium bromide in aqueous solution," *Soft Matter,* vol. 5, pp. 62-66, 2009.

[124] C. Backes, U. Mundloch, A. Ebel, F. Hauke, and A. Hirsch, "Dispersion of HiPco (R) and CoMoCAT (R) Single-Walled Nanotubes (SWNTs) by Water Soluble Pyrene Derivatives-Depletion of Small Diameter SWNTs," *Chemistry-a European Journal,* vol. 16, pp. 3314-3317, 2010.

[125] S. M. Bachilo, M. S. Strano, C. Kittrell, R. H. Hauge, R. E. Smalley, and R. B. Weisman, "Structure-assigned optical spectra of single-walled carbon nanotubes," *Science,* vol. 298, pp. 2361-6, Dec 20 2002.

[126] S. M. Bachilo, L. Balzano, J. E. Herrera, F. Pompeo, D. E. Resasco, and R. B. Weisman, "Narrow (n,m)-distribution of single-walled carbon nanotubes grown using a solid supported catalyst," *J Am Chem Soc,* vol. 125, pp. 11186-7, Sep 17 2003.

[127] S. Y. Ju, W. P. Kopcha, and F. Papadimitrakopoulos, "Brightly fluorescent single-walled carbon nanotubes via an oxygen-excluding surfactant organization," *Science,* vol. 323, pp. 1319-23, Mar 6 2009.

[128] R. B. Weisman and S. M. Bachilo, "Dependence of optical transition energies on structure for single-walled carbon nanotubes in aqueous suspension: An empirical Kataura plot," *Nano Letters,* vol. 3, pp. 1235-1238, Sep 2003.

[129] A. Rao, E. Richter, S. Bandow, B. Chase, P. Eklund, K. Williams*, et al.*, "Diameter-selective Raman scattering from vibrational modes in carbon nanotubes," *Science,* vol. 275, pp. 187-191, 1997.

[130] A. Jorio, M. Dresselhaus, R. Saito, and G. Dresselhaus, "Raman Spectroscopy in Graphene Related Systems, Swiley," ed: VCH, Weinheim, 2011.

[131] A. Jorio, R. Saito, J. H. Hafner, C. M. Lieber, M. Hunter, T. McClure*, et al.*, "Structural (n, m) determination of isolated single-wall carbon nanotubes by resonant Raman scattering," *Phys Rev Lett,* vol. 86, pp. 1118-21, Feb 5 2001.

[132] M. Milnera, J. Kurti, M. Hulman, and H. Kuzmany, "Periodic resonance excitation and intertube interaction from quasicontinuous distributed helicities in single-wall carbon nanotubes," *Phys Rev Lett,* vol. 84, pp. 1324-7, Feb 7 2000.

[133] A. C. Ferrari and J. Robertson, "Interpretation of Raman spectra of disordered and amorphous carbon," *Physical Review B,* vol. 61, pp. 14095-14107, May 15 2000.

[134] A. C. Ferrari and J. Robertson, "Resonant Raman spectroscopy of disordered, amorphous, and diamondlike carbon," *Physical Review B,* vol. 64, p. 075414, Aug 15 2001.

[135] A. C. Ferrari, "Raman spectroscopy of graphene and graphite: Disorder, electron-phonon coupling, doping and nonadiabatic effects," *Solid State Communications,* vol. 143, pp. 47-57, Jul 2007.

[136] M. S. Dresselhaus, A. Jorio, A. G. Souza Filho, and R. Saito, "Defect characterization in graphene and carbon nanotubes using Raman spectroscopy," *Philos Trans A Math Phys Eng Sci,* vol. 368, pp. 5355-77, Dec 13 2010.

[137] K. Iakoubovskii, N. Minami, T. Ueno, S. Kazaoui, and H. Kataura, "Optical characterization of double-wall carbon nanotubes: Evidence for inner tube shielding," *The Journal of Physical Chemistry C,* vol. 112, pp. 11194-11198, 2008.

[138] P. Lutsyk, R. Arif, J. Hruby, A. Bukivskyi, O. Vinijchuk, M. Shandura, *et al.*, "A sensing mechanism for the detection of carbon nanotubes using selective photoluminescent probes based on ionic complexes with organic dyes," *Light-Science & Applications,* vol. 5, p. e16028, Feb 2016.

[139] K. Balasubramanian and M. Burghard, "Chemically functionalized carbon nanotubes," *Small,* vol. 1, pp. 180-192, 2005.

[140] Y.-M. Lin, J. C. Tsang, M. Freitag, and P. Avouris, "Impact of oxide substrate on electrical and optical properties of carbon nanotube devices," *Nanotechnology,* vol. 18, p. 295202, 2007.

[141] B. Chandra, V. Perebeinos, S. Berciaud, J. Katoch, M. Ishigami, P. Kim, *et al.*, "Low bias electron scattering in structure-identified single wall carbon nanotubes: role of substrate polar phonons," *Physical review letters,* vol. 107, p. 146601, 2011.

[142] M. E. Fermann, A. Galvanauskas, and G. Sucha, *Ultrafast lasers: Technology and applications* vol. 80: CRC Press, 2002.

[143] F. Dausinger and F. Lichtner, *Femtosecond technology for technical and medical applications* vol. 96: Springer Science & Business Media, 2004.

[144] M. S. William and M. Jyotirmoy, "Laser material processing," *Steen springer-Verlag, London, Berlin, Heidelberg,* vol. 3, p. 408, 2010.

[145] K. Sugioka and Y. Cheng, "Ultrafast lasers-reliable tools for advanced materials processing," *Light-Science & Applications,* vol. 3, p. e149, Apr 2014.

[146] J. Wang, Y. Chen, and W. J. Blau, "Carbon nanotubes and nanotube composites for nonlinear optical devices," *Journal of Materials Chemistry,* vol. 19, pp. 7425-7443, 2009.

[147] M. Chernysheva, A. Rozhin, Y. Fedotov, C. Mou, R. Arif, M. Kobtsev Sergey, *et al.*, "Carbon nanotubes for ultrafast fibre lasers," in *Nanophotonics* vol. 6, ed, 2017, p. 1.

[148] A. Martinez and S. Yamashita, "5 - Carbon nanotube and graphene-based fiber lasers," in *Carbon Nanotubes and Graphene for Photonic Applications*, ed: Woodhead Publishing, 2013, pp. 121-147e.

[149] S. J. Beecher, R. R. Thomson, N. D. Psaila, Z. Sun, T. Hasan, A. G. Rozhin, *et al.*, "320 fs pulse generation from an ultrafast laser inscribed waveguide laser mode-locked by a nanotube saturable absorber," *Applied Physics Letters,* vol. 97, p. 111114, Sep 13 2010.

[150] G. Della Valle, R. Osellame, G. Galzerano, N. Chiodo, G. Cerullo, P. Laporta, *et al.*, "Passive mode locking by carbon nanotubes in a femtosecond laser written waveguide laser," *Applied physics letters,* vol. 89, p. 231115, 2006.

[151] K. H. Fong, K. Kikuchi, C. S. Goh, S. Y. Set, R. Grange, M. Haiml, *et al.*, "Solid-state Er : Yb : glass laser mode-locked by using single-wall carbon nanotube thin film," *Optics Letters,* vol. 32, pp. 38-40, Jan 1 2007.

[152] T. Schibli, K. Minoshima, H. Kataura, E. Itoga, N. Minami, S. Kazaoui, *et al.*, "Ultrashort pulse-generation by saturable absorber mirrors based on polymer-embedded carbon nanotubes," *Opt Express,* vol. 13, pp. 8025-31, Oct 3 2005.

[153] Y. W. Song, S. Yamashita, C. S. Goh, and S. Y. Set, "Passively mode-locked lasers with 17.2-GHz fundamental-mode repetition rate pulsed by carbon nanotubes," *Opt Lett,* vol. 32, pp. 430-2, Feb 15 2007.

[154] U. Keller, K. J. Weingarten, F. X. Kartner, D. Kopf, B. Braun, I. D. Jung, *et al.*, "Semiconductor saturable absorber mirrors (SESAM's) for femtosecond to nanosecond pulse generation in solid-state lasers," *Ieee Journal of Selected Topics in Quantum Electronics,* vol. 2, pp. 435-453, Sep 1996.

[155] E. J. R. Kelleher, J. C. Travers, Z. Sun, A. G. Rozhin, A. C. Ferrari, S. V. Popov, *et al.*, "Nanosecond-pulse fiber lasers mode-locked with nanotubes," *Applied Physics Letters,* vol. 95, p. 111108, Sep 14 2009.

[156] E. J. R. Kelleher, J. C. Travers, Z. Sun, A. C. Ferrari, K. M. Golant, S. V. Popov, *et al.*, "Bismuth fiber integrated laser mode-locked by carbon nanotubes," *Laser Physics Letters,* vol. 7, pp. 790-794, Nov 2010.

[157] Y. W. Song, S. Y. Set, S. Yamashita, C. S. Goh, and T. Kotake, "1300-nm pulsed fiber lasers mode-locked by purified carbon nanotubes," *Ieee Photonics Technology Letters,* vol. 17, pp. 1623-1625, Aug 2005.

[158] M. A. Solodyankin, E. D. Obraztsova, A. S. Lobach, A. I. Chernov, A. V. Tausenev, V. I. Konov, *et al.*, "Mode-locked 1.93 microm thulium fiber laser with a carbon nanotube absorber," *Opt Lett,* vol. 33, pp. 1336-8, Jun 15 2008.

[159] Y. C. Chen, N. R. Raravikar, L. S. Schadler, P. M. Ajayan, Y. P. Zhao, T. M. Lu, *et al.*, "Ultrafast optical switching properties of single-wall carbon nanotube polymer composites at 1.55 mu m," *Applied Physics Letters,* vol. 81, pp. 975-977, Aug 5 2002.

[160] S. Tatsuura, M. Furuki, Y. Sato, I. Iwasa, M. Tian, and H. Mitsu, "Semiconductor Carbon Nanotubes as Ultrafast Switching Materials for Optical Telecommunications," *Advanced Materials,* vol. 15, pp. 534-537, 2003.

[161] M. Chernysheva, A. Bednyakova, M. Al Araimi, R. C. T. Howe, G. Hu, T. Hasan, *et al.*, "Double-Wall Carbon Nanotube Hybrid Mode-Locker in Tm-doped Fibre Laser: A Novel Mechanism for Robust Bound-State Solitons Generation," *Scientific Reports,* vol. 7, p. 44314, 03/1311/07/received 02/02/accepted 2017.

[162]   M. Chernysheva, M. A. Araimi, H. Kbashi, R. Arif, S. V. Sergeyev, and A. Rozhin, "Isolator-free switchable uni- and bidirectional hybrid mode-locked erbium-doped fiber laser," *Optics Express,* vol. 24, pp. 15721-15729, 2016/07/11 2016.

[163]   M. Chernysheva, M. A. Araimi, S. Sukhanov, R. Arif, and A. Rozhin, "Uni- and bidirectional hybrid mode-locked erbium-doped isolator-free fibre laser," in *2016 International Conference Laser Optics (LO)*, 2016, pp. R1-29-R1-29.

[164]   C. Zou, T. Wang, Z. Yan, Q. Huang, M. AlAraimi, A. Rozhin*, et al.*, "Wavelength-tunable passively mode-locked Erbium-doped fiber laser based on carbon nanotube and a 45° tilted fiber grating," *Optics Communications,* vol. 406, pp. 151-157, 2018.

[165]   R. Vaia and J. Baur, "Materials science. Adaptive composites," *Science,* vol. 319, pp. 420-1, Jan 25 2008.

[166]   S. C. Tjong, *Carbon nanotube reinforced composites: metal and ceramic matrices*: John Wiley & Sons, 2009.

[167]   B. Bhushan, *Springer handbook of nanotechnology*: Springer Science & Business Media, 2010.

[168]   A. P. Demchenko, *Introduction to fluorescence sensing*: Springer Science & Business Media, 2008.

[169]   Y. Piao, B. Meany, L. R. Powell, N. Valley, H. Kwon, G. C. Schatz*, et al.*, "Brightening of carbon nanotube photoluminescence through the incorporation of sp3 defects," *Nat Chem,* vol. 5, pp. 840-845, 10//print 2013.

[170]   K. Yanagi, K. Iakoubovskii, S. Kazaoui, N. Minami, Y. Maniwa, Y. Miyata*, et al.*, "Light-harvesting function of beta-carotene inside carbon nanotubes," *Physical Review B,* vol. 74, p. 155420, Oct 2006.

[171]   A. Ahmad, K. Kern, and K. Balasubramanian, "Selective enhancement of carbon nanotube photoluminescence by resonant energy transfer," *Chemphyschem,* vol. 10, pp. 905-9, Apr 14 2009.

[172]   F. Ernst, T. Heek, A. Setaro, R. Haag, and S. Reich, "Energy Transfer in Nanotube-Perylene Complexes," *Advanced Functional Materials,* vol. 22, pp. 3921-3926, Sep 25 2012.

[173]   F. Vialla, G. Delport, Y. Chassagneux, P. Roussignol, J. S. Lauret, and C. Voisin, "Diameter-selective non-covalent functionalization of carbon nanotubes with porphyrin monomers," *Nanoscale,* vol. 8, pp. 2326-32, Jan 28 2016.

[174]   A. O. Gerasov, K. V. Zyabrev, M. P. Shandura, and Y. P. Kovtun, "The structural criteria of hydrolytic stability in series of dioxaborine polymethine dyes," *Dyes and Pigments,* vol. 89, pp. 76-85, Apr 2011.

[175]   A. O. Gerasov, M. P. Shandura, Y. P. Kovtun, Y. G. Vlasenko, and V. F. Gorchev, "1,3,2-(2H)-Dioxaborine Polymethine Dyes on the Base of Dehydroacetic Acid -

Effective Fluorescent Amine Probes," *Journal of Heterocyclic Chemistry,* vol. 45, pp. 1665-1672, Nov-Dec 2008.

[176]   M. Shandura, Y. P. Kovtun, V. Yakubovskyi, Y. P. Piryatinski, P. Lutsyk, R. Perminov*, et al.*, "Dehydroacetic Acid Based Dioxaborine Styryl Dye: Effective Fluorescent Probe for Ammonia and Amine Detection," in *Key Engineering Materials*, 2014, pp. 159-162.

[177]   M. P. Shandura, Y. P. Kovtun, V. P. Yakubovskyi, Y. P. Piryatinski, P. M. Lutsyk, R. J. Perminov*, et al.*, "Dioxaborine Dyes as Fluorescent Probes for Amines and Carbon Nanotubes," *Sensor Letters,* vol. 12, pp. 1361-1367, // 2014.

[178]   M. Al Araimi, P. Lutsyk, A. Verbitsky, Y. Piryatinski, M. Shandura, and A. Rozhin, "A dioxaborine cyanine dye as a photoluminescence probe for sensing carbon nanotubes," *Beilstein J Nanotechnol,* vol. 7, pp. 1991-1999, 2016.

[179]   A. D. McNaught and A. D. McNaught, *Compendium of chemical terminology* vol. 1669: Blackwell Science Oxford, 1997.

[180]   C. Roquelet, B. Langlois, F. Vialla, D. Garrot, J. S. Lauret, and C. Voisin, "Light harvesting with non covalent carbon nanotube/porphyrin compounds," *Chemical Physics,* vol. 413, pp. 45-54, Feb 21 2013.

[181]   O. A. Dyatlova, J. Gomis-Bresco, E. Malic, H. Telg, J. Maultzsch, G. F. Zhong*, et al.*, "Dielectric screening effects on transition energies in aligned carbon nanotubes," *Physical Review B,* vol. 85, p. 245449, Jun 29 2012.

[182]   T. J. McDonald, C. Engtrakul, M. Jones, G. Rumbles, and M. J. Heben, "Kinetics of PL quenching during single-walled carbon nanotube rebundling and diameter-dependent surfactant interactions," *J Phys Chem B,* vol. 110, pp. 25339-46, Dec 21 2006.

[183]   E. Weiss, K. Groenen-Serrano, and A. Savall, "Electrochemical mineralization of sodium dodecylbenzenesulfonate at boron doped diamond anodes," *Journal of Applied Electrochemistry,* vol. 37, pp. 1337-1344, Nov 2007.

[184]   P. Lutsyk, Y. Piryatinski, M. AlAraimi, R. Arif, M. Shandura, O. Kachkovsky*, et al.*, "Emergence of Additional Visible-Range Photoluminescence Due to Aggregation of Cyanine Dye: Astraphloxin on Carbon Nanotubes Dispersed with Anionic Surfactant," *Journal of Physical Chemistry C,* vol. 120, pp. 20378-20386, Sep 15 2016.

[185]   C. Backes, U. Mundloch, A. Ebel, F. Hauke, and A. Hirsch, "Dispersion of HiPco and CoMoCAT single-walled nanotubes (SWNTs) by water soluble pyrene derivatives--depletion of small diameter SWNTs," *Chemistry,* vol. 16, pp. 3314-7, Mar 15 2010.

[186]   S. Mukhopadhyay and U. Maitra, "Chemistry and biology of bile acids," *Current Science,* vol. 87, pp. 1666-1683, Dec 25 2004.

[187] D. M. Small, S. A. Penkett, and D. Chapman, "Studies on simple and mixed bile salt micelles by nuclear magnetic resonance spectroscopy," *Biochim Biophys Acta,* vol. 176, pp. 178-89, Jan 21 1969.

[188] G. Sugihara, D. S. Shigematsu, S. Nagadome, S. Lee, Y. Sasaki, and H. Igimi, "Thermodynamic study on the Langmuir adsorption of various bile salts including taurine and glycine conjugates onto graphite in water," *Langmuir,* vol. 16, pp. 1825-1833, Feb 22 2000.

[189] Y. Sasaki, T. Igura, Y. I. Miyassu, S. Lee, S. Nagadome, H. Takiguchi*, et al.*, "The adsorption behavior of four bile salt species on graphite in water - Evaluation of effective hydrophobicity of bile acids," *Colloids and Surfaces B-Biointerfaces,* vol. 5, pp. 241-247, Dec 8 1995.

[190] M. Lotya, Y. Hernandez, P. J. King, R. J. Smith, V. Nicolosi, L. S. Karlsson*, et al.*, "Liquid phase production of graphene by exfoliation of graphite in surfactant/water solutions," *J Am Chem Soc,* vol. 131, pp. 3611-20, Mar 18 2009.

[191] S. De, P. J. King, M. Lotya, A. O'Neill, E. M. Doherty, Y. Hernandez*, et al.*, "Flexible, transparent, conducting films of randomly stacked graphene from surfactant-stabilized, oxide-free graphene dispersions," *Small,* vol. 6, pp. 458-64, Feb 5 2010.

[192] X. F. Zhang, T. Liu, T. V. Sreekumar, S. Kumar, V. C. Moore, R. H. Hauge*, et al.*, "Poly(vinyl alcohol)/SWNT composite film," *Nano Letters,* vol. 3, pp. 1285-1288, Sep 2003.

[193] J. G. Duque, L. Cognet, A. N. Parra-Vasquez, N. Nicholas, H. K. Schmidt, and M. Pasquali, "Stable luminescence from individual carbon nanotubes in acidic, basic, and biological environments," *J Am Chem Soc,* vol. 130, pp. 2626-33, Feb 27 2008.

[194] G. Oster, "Spectral studies of polyvinylpyrrolidone (PVP)," *Journal of Polymer Science,* vol. 9, pp. 553-556, 1952.

[195] S. S. Shah, M. S. Khan, H. Ullah, and M. A. Awan, "Solubilization of Amphiphilic Hemicyanine Dyes by a Cationic Surfactant, Cetyltrimethylammonium Bromide," *J Colloid Interface Sci,* vol. 186, pp. 382-6, Feb 15 1997.

[196] A. Martinez and Z. Sun, "Nanotube and graphene saturable absorbers for fibre lasers," *Nature Photonics,* vol. 7, pp. 842-845, 10/30/online 2013.

[197] A. Martinez and S. Yamashita, "Carbon nanotube and graphene-based fiber lasers," in *Carbon Nanotubes and Graphene for Photonic Applications*, ed: Elsevier, 2013, pp. 121-147e.

[198] C. J. Zhao, H. Zhang, X. Qi, Y. Chen, Z. T. Wang, S. C. Wen*, et al.*, "Ultra-short pulse generation by a topological insulator based saturable absorber," *Applied Physics Letters,* vol. 101, p. 211106, Nov 19 2012.

[199]   J. Sotor, G. Sobon, W. Macherzynski, P. Paletko, and K. M. Abramski, "Black phosphorus saturable absorber for ultrashort pulse generation," *Applied Physics Letters,* vol. 107, p. 051108, Aug 3 2015.

[200]   R. I. Woodward and E. J. R. Kelleher, "2D Saturable Absorbers for Fibre Lasers," *Applied Sciences-Basel,* vol. 5, pp. 1440-1456, Dec 2015.

[201]   O. Svelto, "Principles of laser," ed: Springer, 2010.

[202]   H. W. Mocker and R. J. Collins, "Mode Competition and Self-Locking Effects in Aq-Switched Ruby Laser," *Applied Physics Letters,* vol. 7, pp. 270-273, 1965.

[203]   O. Okhotnikov, A. Grudinin, and M. Pessa, "Ultra-fast fibre laser systems based on SESAM technology: new horizons and applications," *New journal of physics,* vol. 6, p. 177, 2004.

[204]   U. Keller, "Ultrafast solid-state laser oscillators: a success story for the last 20 years with no end in sight," *Applied Physics B-Lasers and Optics,* vol. 100, pp. 15-28, Jul 2010.

[205]   Z. Sun, T. Hasan, F. Torrisi, D. Popa, G. Privitera, F. Wang*, et al.*, "Graphene mode-locked ultrafast laser," *ACS Nano,* vol. 4, pp. 803-10, Feb 23 2010.

[206]   Q. L. Bao, H. Zhang, Y. Wang, Z. H. Ni, Y. L. Yan, Z. X. Shen*, et al.*, "Atomic-Layer Graphene as a Saturable Absorber for Ultrafast Pulsed Lasers," *Advanced Functional Materials,* vol. 19, pp. 3077-3083, Oct 9 2009.

[207]   M. C. Gupta and J. Ballato, *The handbook of photonics*: CRC press, 2006.

[208]   R. Paschotta and U. Keller, "Passive mode locking with slow saturable absorbers," *Applied Physics B-Lasers and Optics,* vol. 73, pp. 653-662, Nov 2001.

[209]   U. Keller, "Ultrafast solid-state lasers," *Progress in Optics, Vol 46,* vol. 46, pp. 1-115, 2004.

[210]   A. Gambetta, G. Galzerano, A. G. Rozhin, A. C. Ferrari, R. Ramponi, P. Laporta*, et al.*, "Sub-100 fs two-color pump-probe spectroscopy of single wall carbon nanotubes with a 100 MHz Er-fiber laser system," *Optics Express,* vol. 16, pp. 11727-11734, Aug 4 2008.

[211]   R. Thomson, C. Leburn, and D. Reid, *Ultrafast Nonlinear Optics*: Springer, 2013.

[212]   C. Hönninger, R. Paschotta, F. Morier-Genoud, M. Moser, and U. Keller, "Q-switching stability limits of continuous-wave passive mode locking," *JOSA B,* vol. 16, pp. 46-56, 1999.

[213]   E. Garmire, "Resonant optical nonlinearities in semiconductors," *Ieee Journal of Selected Topics in Quantum Electronics,* vol. 6, pp. 1094-1110, Nov-Dec 2000.

[214]   S. Yamashita, A. Martinez, and B. Xu, "Short pulse fiber lasers mode-locked by carbon nanotubes and graphene," *Optical Fiber Technology,* vol. 20, pp. 702-713, 2014/12/01/ 2014.

[215] M. E. Fermann and I. Hartl, "Ultrafast Fiber Laser Technology," *Ieee Journal of Selected Topics in Quantum Electronics,* vol. 15, pp. 191-206, Jan-Feb 2009.

[216] G. Agrawal, "Application of Nonlinear Fiber Optics–Second Edtion," ed: Academic Press-Elsevier Inc, 2008.

[217] W. B. Cho, J. H. Yim, S. Y. Choi, S. Lee, A. Schmidt, G. Steinmeyer*, et al.,* "Boosting the Non Linear Optical Response of Carbon Nanotube Saturable Absorbers for Broadband Mode-Locking of Bulk Lasers," *Advanced Functional Materials,* vol. 20, pp. 1937-1943, 2010.

[218] C. J. Saraceno, C. Schriber, M. Mangold, M. Hoffmann, O. H. Heckl, C. R. E. Baer*, et al.,* "SESAMs for High-Power Oscillators: Design Guidelines and Damage Thresholds," *Ieee Journal of Selected Topics in Quantum Electronics,* vol. 18, pp. 29-41, Jan-Feb 2012.

[219] G. P. Agrawal, *Lightwave technology: telecommunication systems*: John Wiley & Sons, 2005.

[220] M. Chernysheva, A. Bednyakova, M. Al Araimi, R. C. Howe, G. Hu, T. Hasan*, et al.,* "Double-Wall Carbon Nanotube Hybrid Mode-Locker in Tm-doped Fibre Laser: A Novel Mechanism for Robust Bound-State Solitons Generation," *Sci Rep,* vol. 7, p. 44314, Mar 13 2017.

[221] M. A. Chernysheva, A. A. Krylov, C. Mou, R. N. Arif, A. G. Rozhin, M. H. Rummelli*, et al.,* "Higher-Order Soliton Generation in Hybrid Mode-Locked Thulium-Doped Fiber Ring Laser," *Ieee Journal of Selected Topics in Quantum Electronics,* vol. 20, pp. 425-432, Sep-Oct 2014.

[222] A. G. Rozhin, Y. Sakakibara, H. Kataura, S. Matsuzaki, K. Ishida, Y. Achiba*, et al.,* "Anisotropic saturable absorption of single-wall carbon nanotubes aligned in polyvinyl alcohol," *Chemical Physics Letters,* vol. 405, pp. 288-293, Apr 12 2005.

[223] T. Ramanathan, A. A. Abdala, S. Stankovich, D. A. Dikin, M. Herrera-Alonso, R. D. Piner*, et al.,* "Functionalized graphene sheets for polymer nanocomposites," *Nat Nanotechnol,* vol. 3, pp. 327-31, Jun 2008.

[224] S. Stankovich, D. A. Dikin, R. D. Piner, K. A. Kohlhaas, A. Kleinhammes, Y. Jia*, et al.,* "Synthesis of graphene-based nanosheets via chemical reduction of exfoliated graphite oxide," *Carbon,* vol. 45, pp. 1558-1565, Jun 2007.

[225] A. Martinez, S. Uchida, Y. W. Song, T. Ishigure, and S. Yamashita, "Fabrication of Carbon nanotube-poly-methyl-methacrylate composites for nonlinear photonic devices," *Optics Express,* vol. 16, pp. 11337-11343, Jul 21 2008.

[226] F. Shohda, T. Shirato, M. Nakazawa, K. Komatsu, and T. Kaino, "A passively mode-locked femtosecond soliton fiber laser at 1.5 μ m with a CNT-doped polycarbonate saturable absorber," *Optics Express,* vol. 16, pp. 21191-21198, Dec 22 2008.

[227] F. Shohda, T. Shirato, M. Nakazawa, J. Mata, and J. Tsukamoto, "147 fs, 51 MHz soliton fiber laser at 1.56 mu m with a fiber-connector-type SWNT/P3HT saturable absorber," *Optics Express,* vol. 16, pp. 20943-20948, Dec 8 2008.

[228] J. C. Diels, J. J. Fontaine, I. C. McMichael, and F. Simoni, "Control and measurement of ultrashort pulse shapes (in amplitude and phase) with femtosecond accuracy," *Appl Opt,* vol. 24, p. 1270, May 1 1985.

[229] M. Chernysheva, M. A. Araimi, G. A. Rance, N. J. Weston, B. Shi, S. Saied*, et al.,* "Revealing the nature of morphological changes in carbon nanotube-polymer saturable absorber under high-power laser irradiation," *Scientific Reports,* vol. 8, p. 7491, 2018/05/10 2018.

[230] S. Berber, Y. K. Kwon, and D. Tomanek, "Unusually high thermal conductivity of carbon nanotubes," *Phys Rev Lett,* vol. 84, pp. 4613-6, May 15 2000.

[231] J. Hone, M. Whitney, C. Piskoti, and A. Zettl, "Thermal conductivity of single-walled carbon nanotubes," *Physical Review B,* vol. 59, p. R2514, 1999.

[232] P. S. Thomas, J. P. Guerbois, G. F. Russell, and B. J. Briscoe, "FTIR study of the thermal degradation of poly(vinyl alcohol)," *Journal of Thermal Analysis and Calorimetry,* vol. 64, pp. 501-508, 2001.

[233] F. Bonaccorso, Z. Sun, T. Hasan, and A. C. Ferrari, "Graphene photonics and optoelectronics," *Nature Photonics,* vol. 4, pp. 611-622, Sep 2010.

[234] G. Hu, T. Albrow-Owen, X. Jin, A. Ali, Y. Hu, R. C. T. Howe*, et al.,* "Black phosphorus ink formulation for inkjet printing of optoelectronics and photonics," *Nat Commun,* vol. 8, p. 278, Aug 17 2017.

[235] J.-H. Yun, H. Chang-Soo, J. Kim, J.-W. Song, D.-H. Shin, and Y.-G. Park, "Fabrication of carbon nanotube sensor device by inkjet printing," in *Nano/Micro Engineered and Molecular Systems, 2008. NEMS 2008. 3rd IEEE International Conference on*, 2008, pp. 506-509.

[236] L. Yang, R. W. Zhang, D. Staiculescu, C. P. Wong, and M. M. Tentzeris, "A Novel Conformal RFID-Enabled Module Utilizing Inkjet-Printed Antennas and Carbon Nanotubes for Gas-Detection Applications," *Ieee Antennas and Wireless Propagation Letters,* vol. 8, pp. 653-656, 2009.

[237] S. Matsuzaki, Y. Nobusa, R. Shimizu, K. Yanagi, H. Kataura, and T. Takenobu, "Continuous Electron Doping of Single-Walled Carbon Nanotube Films Using Inkjet Technique," *Japanese Journal of Applied Physics,* vol. 51, p. 06FD18, Jun 2012.

[238] H. Okimoto, T. Takenobu, K. Yanagi, Y. Miyata, H. Shimotani, H. Kataura*, et al.,* "Tunable carbon nanotube thin-film transistors produced exclusively via inkjet printing," *Adv Mater,* vol. 22, pp. 3981-6, Sep 22 2010.

[239] P. Beecher, P. Servati, A. Rozhin, A. Colli, V. Scardaci, S. Pisana*, et al.*, "Ink-jet printing of carbon nanotube thin film transistors," *Journal of Applied Physics,* vol. 102, p. 043710, 2007.

[240] J. Li, F. Ye, S. Vaziri, M. Muhammed, M. C. Lemme, and M. Ostling, "Efficient inkjet printing of graphene," *Adv Mater,* vol. 25, pp. 3985-92, Aug 7 2013.

[241] F. Torrisi, T. Hasan, W. Wu, Z. Sun, A. Lombardo, T. S. Kulmala*, et al.*, "Inkjet-printed graphene electronics," *ACS Nano,* vol. 6, pp. 2992-3006, Apr 24 2012.

[242] J. W. Song, Y. S. Kim, Y. H. Yoon, E. S. Lee, C. S. Han, Y. Cho*, et al.*, "The production of transparent carbon nanotube field emitters using inkjet printing," *Physica E-Low-Dimensional Systems & Nanostructures,* vol. 41, pp. 1513-1516, Aug 2009.

[243] I. M. Hutchings and G. D. Martin, *Inkjet technology for digital fabrication*: John Wiley & Sons, 2012.

[244] B. Derby and N. Reis, "Inkjet printing of highly loaded particulate suspensions," *Mrs Bulletin,* vol. 28, pp. 815-818, Nov 2003.

[245] B. Derby, "Inkjet Printing of Functional and Structural Materials: Fluid Property Requirements, Feature Stability, and Resolution," *Annual Review of Materials Research,* vol. 40, pp. 395-414, 2010.

[246] C. Yaws, "Thermophysical Properties of Chemicals and Hydrocarbons; William Andrew: Norwich, NY, 2008," *Google Scholar*.

[247] S. B. Sant, "Physics and Chemistry of Interfaces," *Materials and Manufacturing Processes,* vol. 28, pp. 1379-1380, 2013/12/02 2013.

[248] A. A. Tracton, *Coatings technology: fundamentals, testing, and processing techniques*: CRC Press, 2006.

[249] P. Beecher, P. Servati, A. Rozhin, A. Colli, V. Scardaci, S. Pisana*, et al.*, "Ink-jet printing of carbon nanotube thin film transistors," *Journal of Applied Physics,* vol. 102, p. 043710, Aug 15 2007.

[250] J. W. Song, J. Kim, Y. H. Yoon, B. S. Choi, J. H. Kim, and C. S. Han, "Inkjet printing of single-walled carbon nanotubes and electrical characterization of the line pattern," *Nanotechnology,* vol. 19, p. 095702, Mar 5 2008.

[251] R. Zhang and P. Somasundaran, "Advances in adsorption of surfactants and their mixtures at solid/solution interfaces," *Adv Colloid Interface Sci,* vol. 123-126, pp. 213-29, Nov 16 2006.

[252] S. P. Chen, H. L. Chiu, P. H. Wang, and Y. C. Liao, "Inkjet Printed Conductive Tracks for Printed Electronics," *Ecs Journal of Solid State Science and Technology,* vol. 4, pp. P3026-P3033, 2015.

[253]   X. Tu, S. Manohar, A. Jagota, and M. Zheng, "DNA sequence motifs for structure-specific recognition and separation of carbon nanotubes," *Nature,* vol. 460, pp. 250-3, Jul 9 2009.

[254]   V. Martinez, R. Le Parc, C. Martinet, and B. Champagnon, "Structural studies of germanium doped silica glasses: the role of the fictive temperature," *Optical Materials,* vol. 24, pp. 59-62, Oct-Nov 2003.

[255]   R. Barrio, F. Galeener, E. Martinez, and R. Elliott, "Regular ring dynamics in AX 2 tetrahedral glasses," *Physical Review B,* vol. 48, p. 15672, 1993.

[256]   F. L. Galeener and A. Geissberger, "Vibrational dynamics in Si 30-substituted vitreous Si O 2," *Physical Review B,* vol. 27, p. 6199, 1983.

[257]   WangF, A. G. Rozhin, ScardaciV, SunZ, HennrichF, I. H. White*, et al.*, "Wideband-tuneable, nanotube mode-locked, fibre laser," *Nat Nano,* vol. 3, pp. 738-742, 12//print 2008.

[258]   R. G. W. Brown, "Absorption and Scattering of Light by Small Particles," *Optica Acta: International Journal of Optics,* vol. 31, pp. 3-3, 1984/01/01 1984.

[259]   A. Martinez, K. Zhou, I. Bennion, and S. Yamashita, "In-fiber microchannel device filled with a carbon nanotube dispersion for passive mode-lock lasing," *Opt Express,* vol. 16, pp. 15425-30, Sep 29 2008.

[260]   K. Kashiwagi and S. Yamashita, "Deposition of carbon nanotubes around microfiber via evanescent light," *Opt Express,* vol. 17, pp. 18364-70, Sep 28 2009.

[261]   Y. W. Song, S. Yamashita, C. S. Goh, and S. Y. Set, "Carbon nanotube mode lockers with enhanced nonlinearity via evanescent field interaction in D-shaped fibers," *Opt Lett,* vol. 32, pp. 148-50, Jan 15 2007.

[262]   B. Xu, M. Omura, M. Takiguchi, A. Martinez, T. Ishigure, S. Yamashita*, et al.*, "Carbon nanotube/polymer composite coated tapered fiber for four wave mixing based wavelength conversion," *Opt Express,* vol. 21, pp. 3651-7, Feb 11 2013.

[263]   A. Martinez, M. Al Araimi, A. Dmitriev, P. Lutsyk, S. Li, C. B. Mou*, et al.*, "Low-loss saturable absorbers based on tapered fibers embedded in carbon nanotube/polymer composites," *Apl Photonics,* vol. 2, p. 126103, Dec 2017.

[264]   M. Sumetsky, Y. Dulashko, and A. Hale, "Fabrication and study of bent and coiled free silica nanowires: Self-coupling microloop optical interferometer," *Opt Express,* vol. 12, pp. 3521-31, Jul 26 2004.

[265]   C. F. Bohren and D. R. Huffman, *Absorption and scattering of light by small particles*: John Wiley & Sons, 2008.

[266]   A. M. Rao, P. C. Eklund, S. Bandow, A. Thess, and R. E. Smalley, "Evidence for charge transfer in doped carbon nanotube bundles from Raman scattering," *Nature,* vol. 388, pp. 257-259, Jul 17 1997.

[267] X. M. Liu, H. R. Yang, Y. D. Cui, G. W. Chen, Y. Yang, X. Q. Wu, *et al.*, "Graphene-clad microfibre saturable absorber for ultrafast fibre lasers," *Sci Rep,* vol. 6, p. 26024, May 16 2016.

[268] G. Steinmeyer, D. H. Sutter, L. Gallmann, N. Matuschek, and U. Keller, "Frontiers in Ultrashort Pulse Generation: Pushing the Limits in Linear and Nonlinear Optics," *Science,* vol. 286, pp. 1507-1512, Nov 19 1999.

[269] S. D. Stranks, C. Weisspfennig, P. Parkinson, M. B. Johnston, L. M. Herz, and R. J. Nicholas, "Ultrafast Charge Separation at a Polymer−Single-Walled Carbon Nanotube Molecular Junction," *Nano Letters,* vol. 11, pp. 66-72, 2011/01/12 2011.

[270] S. D. Stranks, J. K. Sprafke, H. L. Anderson, and R. J. Nicholas, "Electronic and Mechanical Modification of Single-Walled Carbon Nanotubes by Binding to Porphyrin Oligomers," *ACS Nano,* vol. 5, pp. 2307-2315, 2011/03/22 2011.

[271] V. Sgobba and D. M. Guldi, "Carbon nanotubes—electronic/electrochemical properties and application for nanoelectronics and photonics," *Chemical society reviews,* vol. 38, pp. 165-184, 2009.

[272] D. M. Guldi, H. Taieb, G. M. A. Rahman, N. Tagmatarchis, and M. Prato, "Novel Photoactive Single-Walled Carbon Nanotube–Porphyrin Polymer Wraps: Efficient and Long-Lived Intracomplex Charge Separation," *Advanced Materials,* vol. 17, pp. 871-875, 2005.

[273] B. J. Landi, R. P. Raffaelle, S. L. Castro, and S. G. Bailey, "Single-wall carbon nanotube–polymer solar cells," *Progress in Photovoltaics: Research and Applications,* vol. 13, pp. 165-172, 2005.

[274] G. A. Rahman, D. M. Guldi, S. Campidelli, and M. Prato, "Electronically interacting single wall carbon nanotube–porphyrin nanohybrids," *Journal of Materials Chemistry,* vol. 16, pp. 62-65, 2006.